

Stony Brook University



OFFICIAL COPY

The official electronic file of this thesis or dissertation is maintained by the University Libraries on behalf of The Graduate School at Stony Brook University.

© All Rights Reserved by Author.

**Materials Structure Prediction
and
Phase Transition Mechanism Investigation**

A Dissertation presented

by

Guangrui Qian

to

The Graduate School

in Partial Fulfillment of the

Requirements

for the Degree of

Doctor of Philosophy

in

Geosciences

Stony Brook University

August 2015

Stony Brook University

The Graduate School

Guangrui Qian

We, the dissertation committee for the above candidate for the

Doctor of Philosophy degree, hereby recommend

acceptance of this dissertation

Artem R. Oganov - Dissertation Advisor
Professor, Department of Geosciences

Brian L. Phillips - Chairperson of Defense
Professor, Department of Geosciences

Donald J. Weidner
Professor, Department of Geosciences

Troy Rasbury
Associate Professor, Department of Geosciences

Phillips B. Allen
Professor, Department of Physics
Stony Brook University

This dissertation is accepted by the Graduate School

Charles Taber
Dean of the Graduate School

Abstract of the Dissertation

Materials Structure Prediction and Phase Transition Mechanism Investigation

by

Guangrui Qian

Doctor of Philosophy

in

Geosciences

Stony Brook University

2015

A physics-based understanding of the behavior of materials under conditions of high-pressure and high-temperature is full of excitement and challenges. Here, we mainly cover two parts within the subject of high pressure science with USPEX – crystal structure prediction in materials containing hydrogen, and investigation of mechanisms of structural phase transitions.

We applied the USPEX method to study hydrogen hydrate, and hydronitrogen materials. In hydrogen hydrate system, we confirmed that the $\text{H}_2\text{O}-\text{H}_2$ system undergoes a series of transformations with pressure, and adopts the known open-network clathrate structures (sII, C_0), dense "filled ice" structures (C_1 , C_2) and found two novel hydrogen hydrate phases. For hydronitrogen under pressure, numerous unreported and exotic phases are found at pressure up to 800 GPa, such as N_4H , N_3H , N_2H and NH phases composed of nitrogen backbones, the N_9H_4 phase containing two-dimensional metallic nitrogen planes and novel N_8H , NH_2 , N_3H_7 , NH_4 and NH_5 molecular phases. Another surprise is that NH_3 becomes thermodynamically unstable above ~ 460 GPa.

To reveal the phase transition mechanism and pathway for simple and small systems, the variable-cell NEB (VC-NEB) method was developed,

which is very efficient for finding the phase transition path within a static mean-field picture. The method has been applied to the various reconstructive solid-solid B4→B1 and B3→B1 phase transitions of GaN, phase transition in MgF₂ system and guide for experiments for materials synthesis. Combine with the evolutionary metadynamics (EV-metadynamics) and the transition path sampling (TPS) approach, a general procedure for structure phase transition investigation in USPEX is introduced. Different levels of investigation of the fcc→hcp transformation in argon with EV-metadynamics, VC-NEB and TPS methods are performed, helping us to understand comprehensively and deeply the phase transition pathway and mechanism.

To my loving parents. To my wife, Wei Xu.
They made me what I am today.

Table of contents

List of figures	viii
List of tables	xv
1 Introduction	1
1.1 Materials at high pressure	1
1.2 Crystal structure and energy modeling	2
1.2.1 Empirical potentials	3
1.2.2 Density functional theory	5
1.3 Crystal structure prediction	8
1.3.1 Global optimization of the energy landscape	9
1.3.2 Modern methods of crystal structure prediction	10
1.4 Structural phase transition	12
1.4.1 Landau theory	14
1.4.2 Transition state theory	15
1.5 Universal Structure Predictor: Evolutionary Xtallography	17
2 Crystal Structure Prediction	19
2.1 Crystal structure prediction with evolutionary algorithm	19
2.2 Crystal structure prediction in USPEX	20
2.2.1 Variation operators	21
2.2.2 Fingerprint technique	23
2.3 Novel methods and extensions in USPEX	24
3 Structural Phase Transition Mechanism Investigation	28
3.1 Reconstructive structural phase transition	28
3.2 Evolutionary metadynamics method	29
3.2.1 Evolutionary metadynamics method	31
3.2.2 Transition sequence from evolutionary metadynamics	33

Table of contents

3.3	Variable-Cell Nudged Elastic Band Method	34
3.3.1	Variable-Cell Nudged Elastic Band Method	35
3.3.2	Implementation of the VC-NEB method	38
3.3.3	Extra techniques in VC-NEB	40
3.4	Transition path sampling approach	42
3.4.1	Transition path ensemble and sampling	43
3.4.2	Order parameter with fingerprint in USPEX	46
3.5	Studying phase transition in USPEX	47
4	Structure Prediction of Materials Containing Hydrogen	50
4.1	Materials containing hydrogen at pressure	50
4.2	Novel hydrogen hydrate structures under pressure	51
4.2.1	Motivation	51
4.2.2	Hydrogen hydrate structures prediction	52
4.2.3	Novel hydrogen hydrate materials	53
4.2.4	Phase diagram of hydrogen hydrate materials	56
4.2.5	Stability mechanism of hydrogen hydrate materials	58
4.3	Novel hydronitrogens materials under pressure	61
4.3.1	Calculation details	64
4.3.2	Polymeric hydronitrogens	65
4.3.3	Two dimensional N_9H_4 phases	70
4.3.4	Molecular hydronitrogens	70
4.3.5	Discussion	76
5	Phase Transition Pathway and Mechanism investigation	78
5.1	Phase Transition Investigation with VC-NEB	78
5.1.1	Phase transition mechanism of $B4 \rightarrow B1$ and $B3 \rightarrow B1$ in GaN	78
5.1.2	Intermediate phases investigation in MgF_2	85
5.1.3	the VC-NEB method in guiding materials synthesis	87
5.2	Phase transition investigation for argon in USPEX	91
5.2.1	Phase diagram tree from evolutionary metadynamics simulation	92
5.2.2	Transformation pathway investigation with VC-NEB method	93
5.2.3	Nucleation study with TPS approach	94
	References	101

List of figures

1.1	The important types of periodic nets for crystal structure prediction. Figure taken from Ref. [12]	11
1.2	Disconnectivity graph, heat capacity, and free energy surfaces for LJ ₃₈ . Figure taken from Ref. [185]	13
1.3	Landau Theory	14
1.4	Schematic illustrating the crossover between two different states in the framework of transition state theory.	16
2.1	Illustration of the evolutionary algorithm for crystal structure prediction in USPEX.	20
2.2	Illustration of variation operator used in USPEX, (a) heredity, (b) lattice mutation, (c) softmode mutation, (d) permutation. Figures taken from Ref. [127]	22
2.3	A variable composition prediction in a binary Lenard-Jones system. Solid circles denote ground states, while open circles denote metastable solutions. The figure is taken from Ref. [127]	25
3.1	The dynamic evolution (thin lines) labeled by the number of dynamical iterations of free energy minima flooding using metadynamics method. Figure taken from Ref. [85]	30
3.2	Illustration of the evolutionary metadynamics algorithm [204].	32
3.3	Enthalpy evolution during the compression on 72-atom supercell of α -quartz (SiO ₂) at 10 GPa (black line: enthalpies for best structures with constant h ; magenta line: enthalpies for best structures after full relaxation). Figure taken from [204]	34

3.4	The minimum energy path (line with dash gray circle) and initial path are described on enthalpy surface. The forces in the VC-NEB method on image i are shown in the inset. \mathbf{F}_i^∇ is the potential force in the gradient direction. $\mathbf{F}_i^{\nabla\perp}$ and $\mathbf{F}_i^{s\parallel}$ are the transverse component of \mathbf{F}_i^∇ and the spring force, respectively. The forces on Image $i + 1$ indicates the differences between the potential force \mathbf{F}^∇ and $\mathbf{F}^{G-SSNEB}$ in the G-SSNEB method. Figure taken from [143].	37
3.5	Basic procedure of the VC-NEB technique. Figure taken from [143].	38
3.6	Enthalpy barriers for the B4→B1 phase transition of AlN at transition pressure along <i>hexagonal</i> path, by using the VC-NEB and G-SSNEB methods. Figure taken from [143].	39
3.7	Example for enthalpy barrier B4 (wurtzite) → B1 (rocksalt) transformation along the “tetragonal” path. Without rotation-avoiding technique, the structure transformation process starts from image 6 and finishes at image 25, implying that there are only 18 “effective” intermediate images on the phase transition path. Figure taken from [143].	41
3.8	Schematic illustration of two types of potential energy surface topologies as controlled by (a) energetic effects (2nd order phase transitions) and (b) entropic effects (1st order phase transitions). Color scale distinguishes between low energy (blue) and high energy (red) regions. Figure taken from [17]	43
3.9	Transition path sampling iterations at work: (a) a state (black spiral) is randomly chosen from an existing A→B trajectory and a new trajectory is shot off in direction of A. If successful, trajectory is retained, and another shooting point is chosen from it. (b)-(c) The shooting step is repeated in both directions, A→B and B→A, shifting both limits of the shooting window until trajectory decorrelation is achieved. Figure taken from [17]	45
3.10	Fingerprint method working to distinguish the hcp → fcc phase transition in argon. The yellow and green lines indicate the cosine similarity of the configurations along the transformation referenced to fcc and hcp structures, respectively. MD time step is 1 fs.	48
4.1	Enthalpy relative to ice XI as a function of pressure with a van der Waals functional. The phase transition sequence at T = 0 K is ice XI → II → XV → VIII → X.	53

4.2	Convex hull diagram for H ₂ O-H ₂ system at selected pressures and zero temperature. This figure shows the enthalpy of formation (in eV/molecule) of molecular compounds from H ₂ O and H ₂ . The red and yellow circles represent the C ₀ and <i>Ih</i> -C ₀ phases, respectively. The green star represents the sII structure.	54
4.3	(a) Hydrate <i>Ih</i> -C ₀ structure at 0.5 GPa, (b) hydrate C ₃ structure at 30 GPa, (c) cages formed by water molecules in hydrate C ₃ at 100 GPa, the hydrogen molecules are located at the center of each chair-like H-O ring, (d) cages in “filled ice-Ic” hydrate C ₂ , hydrogen molecules are in the center of the cage. Large red and small blue spheres are O and H atoms in water molecules, respectively; the yellow spheres represent the H ₂ molecules in (a) and (b), and represent H atoms in (c) and (d). Red dashed lines represent hydrogen bonds.	55
4.4	Enthalpy of <i>I4</i> ₁ / <i>amd</i> , <i>Pna</i> 2 ₁ and <i>I4</i> ₁ <i>md</i> variants of the C ₂ structure relative to the <i>P4</i> ₁ 2 ₁ 2 structure as a function of pressure. Near 70 GPa, the <i>Pna</i> 2 ₁ H ₂ O-H ₂ transforms to the <i>Imma</i> phase.	56
4.5	Phase diagram of the H ₂ O-H ₂ system. The stability ranges of C ₂ and C ₃ phases are calculated with and without ZPE effect. The solid orange line represents extra stability range added due to ZPE, the dashed orange line represents regions that become unstable after inclusion of the ZPE.	57
4.6	Variations of the Raman shift of the vibron for the H ₂ molecules with pressure from experimental data in [103] and our theoretical calculations. The red and black symbols are the experimental data for H ₂ vibrons in the H ₂ -D ₂ O sample. The blue open circles and squares indicate the Raman shift calculation for C ₂ and C ₃ phases of H ₂ -D ₂ O system, respectively.	58
4.7	The H-O distances in C ₂ and C ₃ phases. The H-bond symmetrization happens around 55 GPa in the C ₂ phase and around 120 GPa in the C ₃ phase.	59
4.8	Bader volumes of the water and hydrogen molecules in ice-VIII, H ₂ -I [141], C ₂ and C ₃ phases as a function of pressure.	60
4.9	Internal energy of the C ₂ and C ₃ phases relative to the isochoric mixture of H ₂ O and H ₂ . Green lines represent the energy of the hydrate phases; red lines – the energy of the isochoric mixture of ice-VIII and H ₂ -I phases.	61
4.10	Internal energy of the C ₂ and C ₃ phases of (a) H ₂ O-He and (b) H ₂ O-Ne, respectively.	62

-
- 4.11 Phase diagram for N-H system from 30-800 GPa. For the hydronitrogen structures, the blue color indicate infinite nitrogen chain structures. Green and pink indicates molecule and molecular ionic structures, respectively. The red color indicates the 2D-plane N_9H_4 phase. 63
- 4.12 Convex hull for nitrogen hydride system at 60, 100, 200, 500, 800 GPa. The solid and hollow symbols indicate stable and metastable phases, respectively. 64
- 4.13 Structures for N_8H and N_9H , (a) $P\bar{1}$ - N_8H molecular structure with four pentazole (N_5H) and six nitrogen molecules. (b) $P\bar{1}$ - N_8H structure with zigzags-shaped nitrogen chain structure. (c) $Cc2m$ - N_9H type with zigzags-shaped nitrogen chains. The red dot lines indicate symmetric hydrogen bonds. 66
- 4.14 The proposed structures for N_4H , N_3H , and N_2H and NH , N_9H_4 . The small pink spheres indicate hydrogen atoms and the blue large spheres are nitrogen atoms. The structures in the pink box are the corresponding monomeric units. (a) $Cmc2_1$ - N_4H structure. The structure is composed of one dimensional zigzag-shaped N-chains. Every two chains are engaged though asymmetric hydrogen bone, and crosswise packed. (b) Layered $P2_1/c$ - N_3H structure containing distorted arm-chair-shaped chain. (c) $P2_1/c$ - N_2H structure composed of parallel one dimensional arm-chair-shaped N_2H chains. (d) $P1$ - NH structure. Its structure consists of $N_2H_5^+$ ion and negatively charged arm-chair-shaped chain layers. It will transform to $C2$ phase at 180 GPa, due to the symmetrization of the hydrogen bonds between $N_2H_5^+$ ions and between chains. (e) The $Fdd2$ - NH structure consists of square-spiral-like chains. (f) Top view and side view of $Ccc2$ - N_9H_4 . The small pink spheres indicate hydrogen atoms and the blue and green large spheres are nitrogen atoms at different layers. 67
- 4.15 (a) The band structure of $P2_1/c$ N_2H phase at 120 GPa. (b) Electron density corresponding to the vicinity of the Fermi level for the $P2_1/c$ N_2H chain structure. The nitrogen atoms have sp^2 hybridization, and are responsible for the π^* orbits along the arm-chair nitrogen chain, which makes N_2H act as a metallic polymer. 69
- 4.16 (a) Band structures of N_9H_4 and (b) Fermi surface of N_9H_4 at 60 GPa. . . . 70

- 4.17 The proposed structures for NH_4 , NH_5 and N_3H_7 . The small pink spheres indicate hydrogen atoms and the blue large spheres are nitrogen atoms. The nitrogen atom in NH_4^+ cation and the H^- anion are noted with green and aqua spheres, respectively. (a) Phase transition sequence from host-guest $Pc \rightarrow$ host-guest $C2/c \leftrightarrow$ Partially ionic $P1$ NH_4 phases. In host-guest structure of $C2/c$ - NH_4 , the hydrogen molecules are captured in the channels formed by NH_3 molecules. In the partially ionic $P1$ - NH_4 structure, the NH_4^+ cation is close to the H^- anion. (b) The ionic $C2/c$ NH_5 phase, with symmetric hydrogen bonds in $[\text{H}_3\text{N} \cdots \text{H} \cdots \text{NH}_3]^+$ units and H^- anions. (c) Phase transition sequence molecular $P1 \rightarrow$ ionic $C2 \rightarrow$ ionic $P-3m1$ N_3H_7 71
- 4.18 (a) Host-guest $I4/m$ NH_4 structure at 60 GPa, the hydrogen molecules fill channels in the frameworks formed by NH_3 molecules. (b) Host-guest $P2_1$ type NH_4 structure at 60 GPa. There is only small difference in the orientation directions of the NH_3 molecules between $P2_1$ and Pc type NH_4 . (c) Short-chain molecular $P2_1/c$ - NH structure at 36 GPa. (d) The $P2_1/m$ - N_3H_7 structure (shown at 400 GPa) is stable in the range 380-680 GPa and consists of buckled N_2H_5^+ and NH_2^- layers. (e) Another $P2_1/m$ N_3H_7 structure (shown at 500 GPa, we call it $P2_1/m$ -II), calculated to be stable above 680 GPa, is also an ionic phase consisting of NH_5^+ and NH_2^- ions. In contrasting to the $P2_1/m$ structure, the NH_2^- layers arrange as zigzag chains plain between the NH_5^+ layers. All the symmetric hydrogen bonds are shown by the red dashed lines. 73
- 4.19 Various structures for NH_5 . (a) Molecular $R3m$ structure at 5 GPa. (b) Ionic $P-43m$ structure at 5 GPa. (c) Ionic $C2/c$ structure at 150 GPa. (d) The view of $[\text{H}_3\text{N} \cdots \text{H} \cdots \text{NH}_3]^+$ subunit in ionic $C2/c$ structure at 100 GPa. (e) Ionic $P2$ structure at 200 GPa. (f) Molecular $P2_1/c$ structure at 40 GPa, where hydrogen molecules locates at the empty channels formed by NH_3 . (g) Another molecular $P2_1/c$ structure at 500 GPa. (h) Ionic $Ama2$ structure at 300 GPa. The small pink spheres indicate hydrogen atoms and the blue large spheres are nitrogen atoms. The nitrogen atom in the NH_4 cation and the H^- anion are noted with green and aqua spheres, respectively. 74
- 5.1 Two representative paths for $\text{B4} \rightarrow \text{B1}$ phase transition, through the *hexagonal* and *tetragonal* intermediate structures, respectively. The structural parameters (u, γ) denote the primary characteristics of these structures. 81

5.2	Enthalpy barrier and evolution of internal structural parameters for the B4→B1 phase transition of GaN at the transition pressure along the “tetragonal” path. The saddle point is at image 15 with a barrier of 0.34 eV/formula.	82
5.3	Enthalpy barrier and internal structural parameters for the B4→B1 phase transition of GaN under transition pressure along the <i>hexagonal</i> path with a barrier of 0.39 eV/formula.	83
5.4	Enthalpy barrier of B3→B1 phase transition in GaN at the equilibrium pressure 45.0 GPa. At images 11 and 21, B1 and B3 structures in a monoclinic cell are found during the MEP searching, respectively. The Ga atoms move along the arrow directions during the phase transition.	84
5.5	Transformation barrier for pyrite → cotunnite structural transition of MgF ₂ at $P = 45.0$ GPa. The intermediate orthorhombic and baddeleyite-type MgF ₂ structures are found along the pathway at image 7 and image 16. The saddle point is at the 26 image with a barrier 0.28eV/f.u.. The blue stage indicates relative enthalpy of the fully relaxed images.	85
5.6	(a) Transformation barrier for pyrite → cotunnite structural transition of MgF ₂ at various pressures. The intermediate orthorhombic type MgF ₂ structure at image 8 is always energy preferred than the pyrite phase above 50 GPa, which is considered as a good candidate for “phase X”. (b) Volume compression of MgF ₂ with pressure. The volume of the orthorhombic structure is ~1.5% smaller than pyrite type. The baddeleyite type MgF ₂ is ~2% denser than pyrite type.	88
5.7	The <i>Ibam</i> → <i>P6/mmm</i> transition of BH system at 168 GPa. A <i>Pbcm</i> intermediate phase is revealed. The saddle points on <i>Ibam</i> → <i>Pbcm</i> and <i>Pbcm</i> → <i>P6/mmm</i> segments have barriers of 0.32 and 0.19 eV/formula, respectively.	89
5.8	Mechanism and energy barrier of hydrazoic acid to <i>P2₁/c</i> N ₃ H phase transition revealed by the VC-NEB method. A unit cell with 32 atoms was used during the pathway calculation. Only one layer of N ₃ H structures during the phase transition are shown at specific images.	91
5.9	Enthalpy evolution in GEM simulation at ambient pressure starting from the hcp structure (red dash line: enthalpies for best structures; blue line: enthalpies for best structures after full relaxation). The structures undergo amorphous phases after at 18 generations.	92
5.10	Phase diagram tree built from the GEM calculations. Many low-symmetry phases are ignored for clarity.	93

5.11	Energy barrier for fcc→hcp structure transition for argon found in a VC-NEB calculation.. The initial pathway is same as the orthorhombic-1 model in Ref. [82]. At images 10 and 14, two intermediate $C2/m$ phases are found as metastable states during the transformation.	94
5.12	Evolution of structural parameters of the fcc→hcp phase transition revealed by VC-NEB. The initial and final structure are described in orthogonal settings, with $\alpha = \beta = \gamma = 90^\circ$	95
5.13	Snapshots taken from a representative trajectory of the real mechanism for the fcc→hcp phase transition.	97
5.14	Evolution of the fingerprint cosine similarity, free energy and temperature in a successful MD TPS trajectory. A and B indicate fcc and hcp phases, respectively. The red and green lines are the cosine similarities of the structures to the fcc and hcp phases, respectively. The top subfigure indicates a successful MD simulation of the fcc→hcp transformation. There are 70,000 MD steps in total, time step is 0.1 fs.	98
5.15	Snapshots taken from a representative trajectory of the nucleation of the orthorhombic and hcp phases. The yellow dashed cycles indicate the site of nucleation.	99

List of tables

4.1	Structure details of stable nitrogen hydrides compounds	77
4.2	Chemical reactions to synthesis high-energy-density hydronitrogen at $\Delta H = 0$	77
5.1	Structure parameters of B4, B3 and B1 structures for GaN at zero pressure. Other calculated and experimental values are also given for a comparison. .	79
5.2	Structural data and atomic coordinates in the orthorhombic ($Pca2_1$) and baddeleyite-type ($P2_1/c$) MgF_2 at 45 GPa.	86

Acknowledgements

I am very grateful to work with my supervisor and my colleagues in the group. The memory of my PhD experience at Stony Brook University can never be erased.

My supervisor, Prof. Artem R. Oganov, has provided me with his supervision, encouragement throughout my PhD study and tremendous support in my life. He is kind of family to me and Candy.

Also thanks to Andriy Lyakhov and his wife Olga. Our two family had a lot of great time together. It's tremendously sad to have lost him.

Thanks to people in my group for exciting discussions, including Andriy O. Lyakhov, Salah E. Boulfefel, Qiang Zhu, Qingfeng Zeng, Huafeng Dong, Xiangfeng Zhou, Xiao Dong, Maxim Rakitin, Shengnan Wang, Mahdi Davari, Haiyang Niu, Fei Qi, Bingxi Li, Jin Zhang and many others in the US and Russia. Thanks to the whole department of Geosciences in Stony Brook, especially Yvonne Barbour, Yuanyuan Liu, Xuebing Wang and Yu Chen's family for their support.

Thanks to my supervisor from Nanjing University, Prof. Huitian Wang, my seniors Jian Sun and Xiangfeng Zhou for their support in my master experience in Nanjing University. That was the my primary step to start my PhD career.

Thanks to my best friend Chenglin Cao.

Thanks to many other people, not mentioned here, who have helped me a lot in both scientific and personal life.

I am indeed very fortunate to have met so many remarkable people in my life. Because of them, I had never given up.

Publications

G.-R. Qian, X. Dong, X.-F. Zhou, *et al.* (2013) Variable cell nudged elastic band method for studying solid–solid structural phase transitions. *Comput. Phys. Commun.*, 184(9), 2111–2118.

G.-R. Qian, A. O. Lyakhov, Q. Zhu, A. R. Oganov, and X. Dong. (2014) Novel hydrogen hydrate structures under pressure. *Sci. Rep.*, 4, 07 .

G.-R. Qian, C.-H. Hu, A. R. Oganov, *et al.* (2014) Diverse Chemistry of Stable Hydronitrogens, and Implications for Planetary and Materials Sciences. arXiv preprint arXiv:1411.4513. **(Submitted)**

X.-F. Zhou, A. R. Oganov, **G.-R. Qian**, *et al.* (2012) First-principles determination of the structure of Magnesium Borohydride. *Phy. Rev. Lett.*, 109(24), 245503.

X. Dong, X.-F. Zhou, **G.-R. Qian**, *et al.* (2013) An *ab initio* study on the transition paths from graphite to diamond under pressure. *J. Phys.: Condens. Matter* 25(14), 145402.

C.-H. Hu, A. R. Oganov, Q. Zhu, **G.-R. Qian**, *et al.*, (2013) Pressure-induced stabilization and insulator-superconductor transition of BH. *Phy. Rev. Lett.*, 110(16), 165504.

H.-F. Dong, A. R. Oganov, Q. Zhu, **G.-R. Qian**. (2015) The phase diagram and hardness of carbon nitrides. *Sci. Rep.*, 5.

A. F. Goncharov, N. Holtgrewe , **G.-R. Qian**, *et al.* (2015) Backbone N_xH compounds at high pressures . *J. Chem. Phys.*, 142, 214308

Y.-Q. Shen, A. R. Oganov, **G.-R. Qian**, *et al.* (2015) Novel lithium-nitrogen compounds at ambient and high pressures. *Sci. Rep.*. **(Accepted)**

X. Dong, A. R. Oganov, A. F. Goncharov, E. Stavrou, S. Lobanov, G. Saleh, **G.-R. Qian**, *et al* (2013). Stable Compound of Helium and Sodium at High Pressure. arXiv preprint arXiv:1309.3827. **(Submitted)**

X. Dong, A. R. Oganov, **G.-R Qian**, *et al.* (2015) How do chemical properties of the atoms change under pressure. arXiv preprint arXiv:1503.00230. **(Submitted)**

M. S. Rakitin, A. R. Oganov, H.-Y. Niu, M. Esfahani, X.-F. Zhou, **G.-R Qian**, *et al.* (2015) Novel phase of beryllium fluoride at high pressure. arXiv preprint arXiv:1506.03861. **(Submitted)**

D.-X. Li, A. R. Oganov, X. Dong, X.-F. Zhou, Q. Zhu, **G.-R Qian**, *et al.* (2015) Nitrogen oxides under pressure stability, ionization, polymerization, and superconductivity. arXiv preprint arXiv:1506.08362. **(Submitted)**

Motivation

Over the past decade, high-pressure materials science has awoken with another surge of activity. The high-pressure experimental and theoretical research has been revolutionized due to the technological and methodological breakthroughs. In laboratory experiments, the exploration of solid state at extreme pressures under several hundred gigapascals (GPa), even up to terapascal (TPa), is made possible due to the recent progress in diamond-anvil-cell (DAC) and shock-wave techniques.

The application of high pressure, especially together with high temperature, has revealed interesting alteration of the atomic arrangements, resulting in unexpected structure transformations and emergence of novel compounds. Properties that appear with these phase transitions, like mechanical and optical responses, conductivity, magnetic ordering, differ from those studied and observed at ambient conditions. These exciting modifications of physical and chemical properties of materials provide a different dimension to the synthesis of new materials and a novel field in material research and design. The application of high-pressure techniques has been exploited in the field of physics, chemistry, geosciences and also the biosciences. The fascination with the application of high pressure is strengthened by the possibility of producing potentially important materials, pharmaceuticals with unique properties unprecedented at normal conditions. For example, high-pressure synthesis provides a general route to extremely hard materials, by bringing the atoms closer together and creating new bonds and new very dense structures.

The optical, infrared spectroscopy, neutron and x-ray diffraction help to characterize these novel materials. But with the high cost and lack of guidance for material synthesis under extreme conditions, the productivity of this approach is not optimal. Hence, the dream of computational material design is to offer a more general, flexible and reproducible route in materials prediction and design, before the materials are synthesized.

By now, it is widely believed that crystal structure prediction is achievable and as well the key step to the computation material design, though this problem was considered an intractable “scandal” not long ago [5, 50, 104]. As stated by Artem R. Oganov [124] :

“Crystal structure is arguably the most important piece of information about a material, as it determines – directly or indirectly – pretty much all properties of a material.”

For materials design, it is of crucial importance to know and be able predict the structure.

One of the most general and powerful techniques, inspired by the nature itself, and adaptable for any specific global minimal searching problems, is the evolutionary algorithm (EA) method. Different from *structural diagram* and *data mining approaches*, the EA method needs just the information about chemical elements to run computational optimization based on the fitness function, i.e., the (free) energy, or specific properties (hardness, density, band gap, superconducting T_c). The local optimization – structure relaxation – makes structure prediction easier and more reliable, by greatly reduce the landscape searching. With more accurate quantum mechanical first-principle calculations, as opposed to empirical/semi-empirical potentials methods, reliable fitness ranking guides the EA prediction better. The USPEX code is based on the EA method and has made impressive successes in structure prediction.

We also focus on synthesis and phase transformation of materials. Understanding of the mechanism and pathways of transitions between different phases will guide many cases the synthesis experiments.

The main purpose of this work is to achieve further development of the USPEX method for complex and more challenging systems. We also try to illustrate an epitome of phase transition mechanism approaches to reveal a detailed picture of phase transition mechanisms under the framework of USPEX.

The layout of this thesis is as follows: In Chapter 1, we describe the background and methods employed in this thesis. A general introduction of USPEX and recently developed methods/extensions for structural prediction are given in Chapter 2, this part is mainly basic on Ref. [124, 200]. In Chapter 3, we introduce all the three approaches of phase transition investigation implemented in USPEX [17, 143, 200, 204] . Chapter 4 and Chapter 5, we report our results in studying the H-O and N-H systems at pressure and phase transition mechanism investigation for GaN, BH, MgF₂ and the argon systems using USPEX [143–145].

Chapter 1

Introduction

1.1 Materials at high pressure

High pressures occur inside of planets and stars and in both natural and man-made environments. The range of pressures encountered in the universe is extremely wide, varying from the familiar vacuum space by 60 orders of magnitude to the pressure found at the center of a neutron star. In the whole universe, most matter exists under high pressure. In our planet, the pressure at sea level is 1 *atmosphere* (10^{-4} GPa) and the center of the Earth is at a pressure of 350 GPa. Studies of high-pressure behavior of planetary materials are a key step to understand the structure and evolution of our Earth and other planets.

In laboratory, high pressures can be applied in the diamond-anvil-cell (DAC), shock-wave techniques, and large-volume presses. Static pressure applied in a DAC is a continuously varying parameter which can be used for systematic studies of the properties of solids as a function of interatomic distances. With the well-controlled high pressure technique, one can experimentally shorten atomic distance, enhance orbital overlap, and consequently modify crystalline structures and tune interactions, and eventually generate new states of materials which are different from normal compounds available at ambient conditions. Therefore, high pressure is now a powerful and efficient way to discover novel condensed states and functional materials. For example, pressure is now the main route of synthesis of super hard materials. Pressure brings about superconductivity in conventional materials [3, 56], by substantially modifying the electron correlation and electron-phonon interaction. Recently, an extremely high T_c (as high as ~ 200 K) was predicted for the high-pressure compound H_3S , which represents a significant step toward the understanding of the high pressure behavior of metallic hydrogen and hydrogen-rich hydrides [39]. The pressure-induced insulator-metal transformation is common under pressure. With the tendency towards electron delocalization

in all insulators, semiconductors and even molecular crystals eventually become metals at a sufficiently high pressure.

Pressure ranges accessible in the laboratory are still rather limited, and the corresponding structural determination and characterization for a given materials under high pressure is still a challenge. On the other hand, with the help of state-of-the-art computer simulations, prediction of the behavior of materials under high pressure is now achievable. Currently, structural prediction is an essential tool in high pressure science and in materials research and design.

1.2 Crystal structure and energy modeling

Understanding of crystal structures is the soul of materials science and mineralogy. Crystal structure is a translational repetition of a small fragment called “unit cell”. The arrangement pattern of atoms includes a fundamental property of a crystal structure — symmetry, which has a profound influence on the properties of material. To formulate the structure in a mathematical way, we use the vectors configuration to describe the shape of the lattice, the symmetry and atomic information of the crystal. The configuration of the crystal structure, with its unique structural characteristics, can also further be used to calculate the properties with theoretical and computational methods.

With the advent of newer computational and theoretical methods, computerized virtual modeling of crystal structures and access to large crystal structure databases are now available to supplement traditional tools and methods of crystallographic research. Among these theoretical methods, the empirical potentials and quantum simulation and density functional theory provide different levels of quality for energy ranking and properties estimation. In practice, *ab initio* calculations are limited to a few hundred atoms and a few picoseconds, while giving very precise results. In many cases, the results of first-principle calculations, such as the very popular density functional theory for solid-state systems agree quite satisfactorily with experimental data. By now, first principle method finds increasingly broad application in the material sciences for the interpretation and prediction of the behavior of complex systems at an atomic scale. With empirical methods, one can run simulations of millions of atoms for a nanosecond, but which is poor at descriptions of specific properties related to the electron behavior. Empirical methods still provide the only method of atomistic simulation in these large scale regimes. For many physical problems, such as fracture, protein folding, dislocation dynamics, phase transition dynamics, much of their physics is dominated by geometry. In these cases, finite size effects are more important than accurate energetics and empirical potential methods find their home.

1.2.1 Empirical potentials

Given a defined crystal lattice and its initial atomic coordinates, a way for describing the energy and other properties of the system for any configuration is needed. For empirical models, a functional form is usually chosen for the energy, with a number of parameters that have to be calculated. Then we fit these parameters to reproduce a set of data from experiment or high accuracy quantum calculations. The parameter sets development is a laborious process. Both the functional form and parameters sets require extensive optimization, and usually are system dependant. Thus, there are no universally good potentials, but only potentials that are appropriate for a given problem. A brute-force iterative parameter modification needs to be performed to reach a good agreement between the model system and results derived from *ab initio* calculations, or experiments.

For empirical potentials, we often choose the interatomic potential depending on the area of proposed application. Here, we assume that the total energy can be described by an empirical potential for the system of N atoms, and the total energy can be expressed in a many-body expansion:

$$U(R_1, R_2, \dots, R_N) = \sum_i U_1(R_i) + \sum_i \sum_{j>i} U_2(R_i, R_j) + \sum_i \sum_{j>i} \sum_{k>j} U_3(R_i, R_j, R_k) + \dots \quad (1.1)$$

where U_i is the i -body term. U_1 is the term related to an external field or boundary conditions. Specifically, U_2 is a term representing the interaction of any atomic pair with a distance of $\mathbf{r} = R_i - R_j$, which is named “pair potential”.

When the many-body expansion is truncated at U_2 with three or more body atomic interaction ignored, a pair potential is used to describe the interaction that is only dependent on distances between the atoms. Pair potentials are very common in physics. Coulomb potentials are often used for different systems; other famous examples include Lennard-Jones (LJ) potential, Morse potential and Buckingham potentials. Usually, in a pair potential, there is one repulsion and another attraction term.

Lennard-Jones potential The LJ potential is a mathematically simple model, and the most common expression of this potential is :

$$U(\mathbf{r}) = 4\epsilon \left[\left(\frac{\sigma}{\mathbf{r}} \right)^{12} - \left(\frac{\sigma}{\mathbf{r}} \right)^6 \right] \quad (1.2)$$

where ε is the depth of the potential well, σ is the distance where the inter-particle potential reaches zero and \mathbf{r} is the distance of pair atoms. These parameters can be fitted to the experimental data or accurate quantum simulation calculations. The $1/\mathbf{r}^{12}$ term describes the Pauli repulsion at short ranges, when the electronic clouds surrounding the atoms start to overlap, the energy of the system increases steeply. The term $1/\mathbf{r}^6$ represents attraction due to weak dispersion interactions, which become dominant when \mathbf{r} increases. This weak interaction term gives a proper description for the van der Waals (vdW) interaction in molecular systems. Due to its computational simplicity, the Lennard-Jones potential is used extensively in computer simulations.

Morse potential Compared to Lennard-Jones potential, the Morse potential is more suitable for describing systems with covalent chemical bonds. It can also be used to model the interaction between an atom and a surface.

$$U(\mathbf{r}) = \varepsilon[e^{-2\alpha(\mathbf{r}-\mathbf{r}_e)} - 2e^{-\alpha(\mathbf{r}-\mathbf{r}_e)}] \quad (1.3)$$

ε is the well depth, α controls the width of the potential, and \mathbf{r}_e is the equilibrium bond distance.

Buckingham potential Buckingham potential is a further approximation of the Lennard-Jones function, with the repulsion term in an exponential form. In fact, exponential term gives better and more physical description and of strong repulsion due to overlap of the closed shell electron clouds. The Buckingham potential can be expressed as :

$$U(\mathbf{r}) = Ae^{-B\mathbf{r}} - C/\mathbf{r}^6 \quad (1.4)$$

In Buckingham model, “nuclear fusion” [72] occurs when \mathbf{r} becomes small, when the exponential term converges to a constant when \mathbf{r} goes to 0 and the $1/\mathbf{r}^6$ term diverges.

In practice, all these above pair potentials have a cut off at a certain range. Pair potentials describe well the inert gases, molecular models and ionic systems. However, they fail in the cases when the environmental dependence needs to be considered and many-body effects become important. For example, for a metallic system with defects, the individual atom near defect site must be very different from other atoms. Similarly, pair potentials are generally inadequate for covalent systems, where many-body effects play an important role. Pair potentials do not account for the directional nature of the bond. Therefore, the three-body term and even higher body terms need to be introduced to describe the bond angle, torsion effects, and so on in a more precise force field method.

1.2.2 Density functional theory

Different from empirical potentials, first-principles calculations provide the ideal complement to the laboratory approach without requiring extra information from experiment; that is, there are no free parameters in the theory. It has no practical limits to the pressures and temperatures which can be calculated. So simulation can predict the properties of materials under extreme conditions, guiding experimentalists to find novel materials, or calculating properties of materials which may be difficult to measure experimentally. Typical applications of first-principles methods have involved calculating crystal structures, optical and conduction properties, and phase transitions. Density functional theory is the well established, thought an approximate, theoretical method to describe materials properties.

Quantum simulation The principles of quantum mechanics is the most reliable way to determine the energy and describe any physical systems at the atomic scale. To investigate a system of N electrons and M nuclei, we start with the Schödinger equation :

$$\hat{H}\Psi = E\Psi \quad (1.5)$$

where

$$\Psi = \Psi(\mathbf{r}_1, \dots, \mathbf{r}_N, \mathbf{R}_1^n, \dots, \mathbf{R}_M^n) \quad (1.6)$$

is a wave function that depends on the position of all electrons \mathbf{r} and nuclei \mathbf{R}^n . And \hat{H} is the Hamiltonian operator of the system, which takes the form :

$$\begin{aligned} \hat{H} = & -\sum_i \frac{\hbar^2}{2m_e} \nabla_i^2 + \frac{1}{2} \sum_{i \neq j} \frac{e^2}{|\mathbf{r}_i - \mathbf{r}_j|} + \sum_{i,l} \frac{Z_l e^2}{|\mathbf{r}_i - \mathbf{R}_l|} \\ & - \sum_I \frac{\hbar^2}{2M_I} \nabla_I^2 + \frac{1}{2} \sum_{I \neq J} \frac{Z_I Z_J e^2}{|\mathbf{R}_I - \mathbf{R}_J|} \end{aligned} \quad (1.7)$$

This is too complicated to be exactly solved, only possible for the simplest systems. Layers of approximations are applied, hopefully maintaining physical relevance, to solve it successfully in complex systems. The first step is to separate the nuclei and the electronic degrees

of freedom with the Born-Oppenheimer approximation, where the nuclei terms would be constant. Thus, the Schrödinger equation can be rewritten as :

$$\hat{H} = \underbrace{-\sum_i \frac{\hbar^2}{2m_e} \nabla_i^2}_{\hat{T}} + \underbrace{\frac{1}{2} \sum_{i \neq j} \frac{e^2}{|\mathbf{r}_i - \mathbf{r}_j|}}_{V_H} + \underbrace{\sum_{i,I} \frac{Z_I e^2}{|\mathbf{r}_i - \mathbf{R}_I|}}_{V_{\text{ext}}} \quad (1.8)$$

To solve this many-body Schrödinger equation, there many sophisticated methods developed based on the expansion of the wavefunction in Slater determinants. The most popular solution in quantum chemistry sometimes is the Hartree-Fock and post-Hartree-Fock methods [7].

Density functional theory In 1964, the density functional theory (DFT) was proposed by Hohenberg and Kohn [67] to solve the many-body problem with a more sophisticated way. The central idea of DFT is to replace the many-body problem with the the electron density. The electron density, with its dependence on three spatial coordinates, will implicitly contain the electronic degrees of freedom. The original formulation is based on two theorems as follows:

Theorem I: For any system of interacting particles in an external potential V_{ext} , the potential V_{ext} is determined uniquely, except for a constant, by the ground state particle density $\rho_0(r)$.

Theorem II: A universal functional for the energy $E[\rho]$ in terms of the density $\rho(r)$ can be defined, valid for any external potential V_{ext} . For any particular potential V_{ext} , the exact ground state energy of the system is the global minimum value of this functional, and the density $n(r)$ that minimizes the functional is the exact ground state density $\rho_0(r)$.

The Kohn-Sham ansatz [79] is to replace the many-body system of the interacting electrons, $\Psi(r_1, r_2, \dots)$, with a set of non-interacting one-body wave functions, $\{\psi_i(r)\}$ to produce the correct ground state density $\rho = \sum |\psi_i(r)|^2$. The ground state energy of the interacting system $E[\rho]$ then has the same ground state energy of the non-interacting quasiparticles system $E_{\text{KS}}[\rho]$. The universal functional now can be expressed as:

$$E_{\text{KS}}[\rho] = E_{\text{kinetic}} + \int d^3r [V_{\text{ext}}(r)\rho(r)] + E_{\text{Hartree}}[\rho] + E_{\text{xc}}[\rho] \quad (1.9)$$

The energy under KS ansatz is divided into kinetic energy (T), Hartree energy (E_H), the external potential (V_{ext}) and a term containing all the many-body terms, E_{xc} . The exact form

1.2 Crystal structure and energy modeling

of E_{xc} is the only unknown term so far. The KS approach involves independent particles but an interacting density. Thus, all the difficult many-body terms are incorporated into the exchange-correlation functional of the density. If the solution of $E_{xc}[\rho]$ is available, the KS equation can be solved by self-consistent iteration, which would lead to the exact energy. However, there is no way to obtain the exact form of $E_{xc}[\rho]$. Instead, we have to reasonably approximate it.

Exchange-correlation To practically solve the equations with the unknown E_{xc} , the Local Density Approximation (LDA) was introduced at the same time as Kohn-Sham equations, and used in the early works. Such type exchange-correlation energy density describe a uniform electron gas over all space with the $E_{xc}[\rho]$, only depending on the local electron density. It can be expressed as :

$$E_{xc}^{LDA}[\rho] = \int d^3r \rho(r) E_{xc}[\rho] \quad (1.10)$$

LDA is the simplest density functional and also a very successful approximation. It was used for a generation in materials science and yielded good results for a broad range of materials. But it is insufficiently accurate for most chemical purposes. LDA typically overbinds molecules, underestimates the band gap of semiconductors and lattice parameters.

A natural extension to overcome these limitations is to include the gradient of the density, and obtain the exchange and correlation from a uniform electron gas with a gradient. It is known today as so call Generalized Gradient Approximation (GGA).

$$E_{xc}^{GGA}[\rho] = \int d^3r \rho(r) E_{xc}[\rho, \nabla\rho,] \quad (1.11)$$

GGA improves the shortcomings of LDA's poor description of strong inhomogeneous system. There is no unique way to determine the gradient dependence of the uniform electron gas. Many different reformulations and extensions of GGA have been proposed and tested over the years. One of the widely used GGA functionals is the Perdew-Burke-Ernzerhof (PBE) [133].

In many cases, DFT calculations agree quite satisfactorily for solid-state systems with experimental data, but also failed in many cases. To solve the problem of failing to describe strongly localized and interacting electrons in transition metal oxides and rare earth elements and compounds, the Hubbard models [2] is proposed to remedy this issue with an artificial "U" term in the LDA+U method. However, it was still not considered accurate enough for some calculations, especially in quantum chemistry field. Many other modern methods, like semi-local functionals (PBEsol [135]), hybrid functionals (PBE0 [1], HSE [64], B3LYP

[8]) and methods considering more accurate dispersion effects (DFT-D [55], vDw-DF [37]) are proposed to obtain more accurate $E_{xc}[\rho]$ functionals.

Pseudopotentials The pseudopotential approach was introduced for efficient implementation of DFT, which attempts to replace the complicated all-electron effects with a simplified description. The core electrons are usually chemically inert, and do not contribute to bonding. Therefore, there is no need to treat them explicitly. With the pseudopotential, the kinetic of the core (i.e. non-valence) electrons of an atom and its nucleus are simplified, where core states are eliminated and the valence electrons are described by pseudo-wavefunctions with significantly fewer nodes. A good pseudopotential reproduces the true potential outside the core region while give a much smoother potential inside the core. Thus, the pseudopotential method greatly decreases the computational complexity in DFT calculations.

Norm-conserving and ultrasoft [178] are the two main modern pseudopotential approaches used in most of plane-wave electronic structure codes. A further approximation implied by ultrasoft pseudopotential — the projector augmented wave (PAW) method [13] — was proposed to introduce projectors and auxiliary localized functions to present a general approach to solution of the electronic structure.

1.3 Crystal structure prediction

Predicting the crystal structure at the atomic level is a considerable fundamental challenge in condensed matter science. Understanding the structure of materials is fundamental to being able to understand their properties, and then helpful to classify them for specific applications. Compared to identifying the structure information from the experiments, the task of crystal structure prediction is more challenging, due to an extremely large number of degrees of freedom to be explored, the complexities of interatomic forces, and the difficulty in choosing a suitable computational criterion for identifying those crystal structures favored by nature.

With the development of the density functional theory and electronic structure techniques, the modeling of the crystals becomes a routine nowadays. It is generally possible to model the equilibrium, relax the structure and minimize the energy of structures of solids with acceptable accuracy. More ambitiously, we may take an approximate structure, whose energy is then minimized, to generate a more accurate model.

1.3.1 Global optimization of the energy landscape

In the crystal structure prediction problem, the most popular way is considering it as a optimization problem for searching the crystal structures in a high dimensional configuration space. When the crystal structure modeling solves the structure searching problem in a “local optimization” level, then a crystal structure prediction becomes possible, owing to the the crystal structure prediction problem modeling to a problem in exploring the configurational space defined by the internal coordinates of the unit cell. The structure relaxation process, as a local minimal optimization method, significantly decreases the dimension of configuration space. Therefore, the structure prediction problem then changes to explore the “smooth” energy landscape when considering energy as the fitness function, because every structure only has an identical energy and the energy landscape continuity of the of the configuration space.

For a system with N atoms, the number of distinct points on the landscape can be estimated as:

$$C = \binom{V/\delta^3}{N} \prod_i \binom{N}{n_i} \quad (1.12)$$

where V is unit cell volume of the N atoms, δ is a relevant discretization parameter (for instance, 1) and n_i is the number of atoms of i -th type in the unit cell. Thus, the configuration space for crystal structure prediction is astronomically large (roughly 10^N if one uses $\delta = 1$ and typical atomic volume of 10^3), even for small systems ($N \approx 10 - 20$),

Besides, the dimensionality of the energy landscape is considered as:

$$d = 3(N - 1) + 6 \quad (1.13)$$

where $3N - 1$ degrees of freedom are from N atoms, and the remaining six dimensions comes from the lattice.

Huge numbers of local minimums exist on the landscape, which makes the crystal prediction problem basically a NP-hard problem, where the difficulty increases exponentially with the dimensionality. Fortunately, structure relaxation technique from crystallography can smooth the fluctuant landscape surface. Great reduction of dimensionality of the configuration space can be achieved when the crystal structures are relaxed for the nearest local energy minima. Within employing the relaxation technique, the intrinsic dimensionality can be reduced:

$$d^* = 3(N - 1) + 6 - \kappa \quad (1.14)$$

where κ is the number of correlated dimensions, which could vary a lot according to the intrinsic chemistry in the system. For example, the dimensionality drops a lot from 99 to 11.6 for $\text{Mg}_{16}\text{O}_{16}$, and a few from 39 to 32.5 for $\text{Mg}_4\text{N}_4\text{H}_4$. Thereby, the reduced complexity for the energy landscape of local minima is:

$$C^* = \exp(\beta d^*) \quad (1.15)$$

This implies that any efficient search method for crystal structure prediction must include structure relaxation.

1.3.2 Modern methods of crystal structure prediction

Many types of approaches have been proposed to address the “crystal structure prediction” (CSP) problem, like data mining approaches (structure models by analogy), structural diagrams and topological modeling methods, etc. The topological approaches aim at constructing the simplest topologies consistent with the already known chemistry of the system. The data mining and structural diagrams approaches show great predictive power when there is compound information in multinary compounds. These methods show a good ability in structure prediction but empirical or data-based, which extremely limit their application in different “real” situations, like exotic compounds.

The crystal structure prediction problem can be seen as a mathematical problem of “global optimization”, and there are many approaches successful in solving such global minimization/maximization problems.

Typical modern solutions for crystal structure prediction are introduced below. Other methods based on genetic population-based metaheuristic optimization algorithms will be described in later chapters.

Periodic-Graph Approach A straight idea to solve the crystal structure prediction problem is to do materials design from the existing knowledge of materials. When focusing not only on the atomic positions but also the chemical bonds of the geometrical model of crystals, the topological approach [130] gradually developed as a new modern crystallochemical analysis method. Under this point of view, the materials research and design come up to a new level, with analysis of the topological motifs through hundred thousands of crystal structures (See Ref. [12] and relevant reference-in). A comprehensive prediction of the crystal structure, with the periodic-graph/topological approach, only needs to find the complete net since all other representations can be derived from the complete one. In practice, only some partial representations are needed for structure prediction.

1.3 Crystal structure prediction

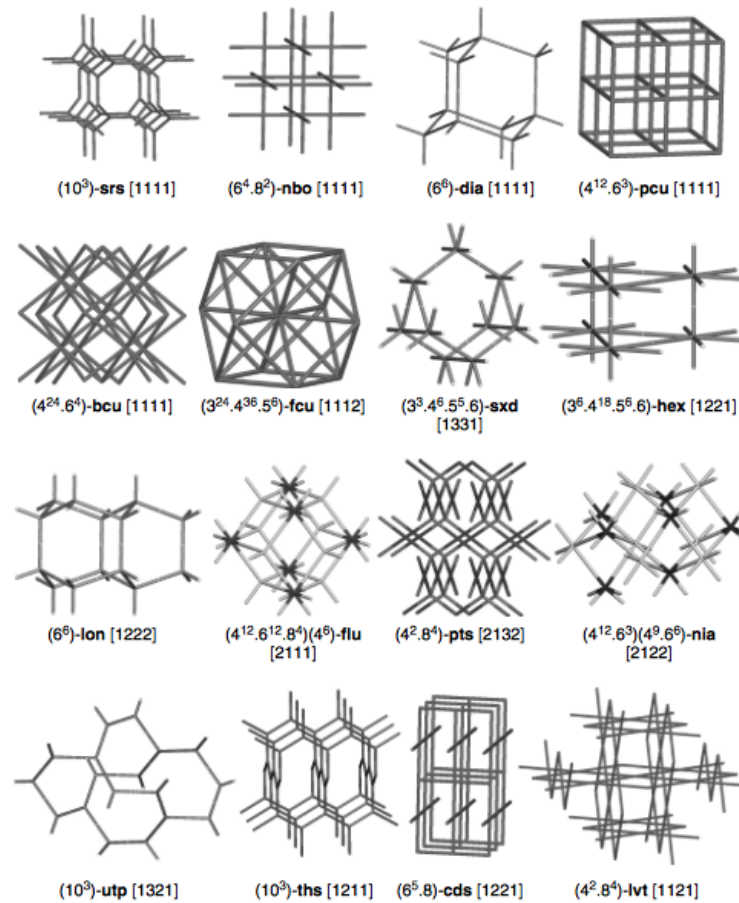


Fig. 1.1 The important types of periodic nets for crystal structure prediction. Figure taken from Ref. [12]

Random Search Methods Compared to periodic-graph approach, the random search methods for structure prediction do not require priority knowledge of the systems. A repeated routine of generating random arrangement of atomic or molecular components and running local minimization is the complete diagram for the method. Sometimes, bias-search on the PES and some constraints are used to accelerate the method [140]. The random search only requires very few parameters, and is very easy to implement. Though this randomly guessing solution is not the most efficient way to solve the problem, the random search methods are also widely used [140], and most times is used as a partial function feature in other modern methods, like evolution-algorithm methods .

Basin-Hopping Method Basin-hopping [184] is a stochastic algorithm which attempts to find the global minimum of a smooth scalar function. For structure prediction problem with basin-hopping, the potential energy surface is transformed into a collection of interpenetrating staircases [186, 187]. Hopping moves for structure prediction are proposed by perturbing the current geometry and are accepted or rejected based upon the energy difference between the local minima obtained following minimization from the two instantaneous configurations. Together with the disconnectivity graphs approach [153, 160], the basin-hopping approach is able to provide insight into the organization of the PES in a two-dimensional figure.

1.4 Structural phase transition

Structural phase transitions, a common phenomena in nature, determine many aspects of the behavior of materials, and thus provide a novel way in the discovery of new materials with different chemical and physical properties.

Solid-solid phase transition could be generally classified into two types: first-order and second order. First order phase transitions often are reconstructive. By contrast, second-order ones are either displacive or order-disorder. Second order transitions always involve group-subgroup symmetry relations

Solid-solid phases are often induced by pressure or temperature. Currently, the investigations of solids under several hundred GPa is made possible in lab with the recent progress in high pressure techniques of DAC and shock-wave. Under such conditions, a massive of novel and exotic compounds are often found. The properties of the compounds at high pressure like mechanical stability, ferroelectric response, conductivity switching, magnetic order, mass and electronic transport, differ from those studied and observed at normal conditions. The high pressure provides a broad way in novel material research and design, which including differ-

1.4 Structural phase transition

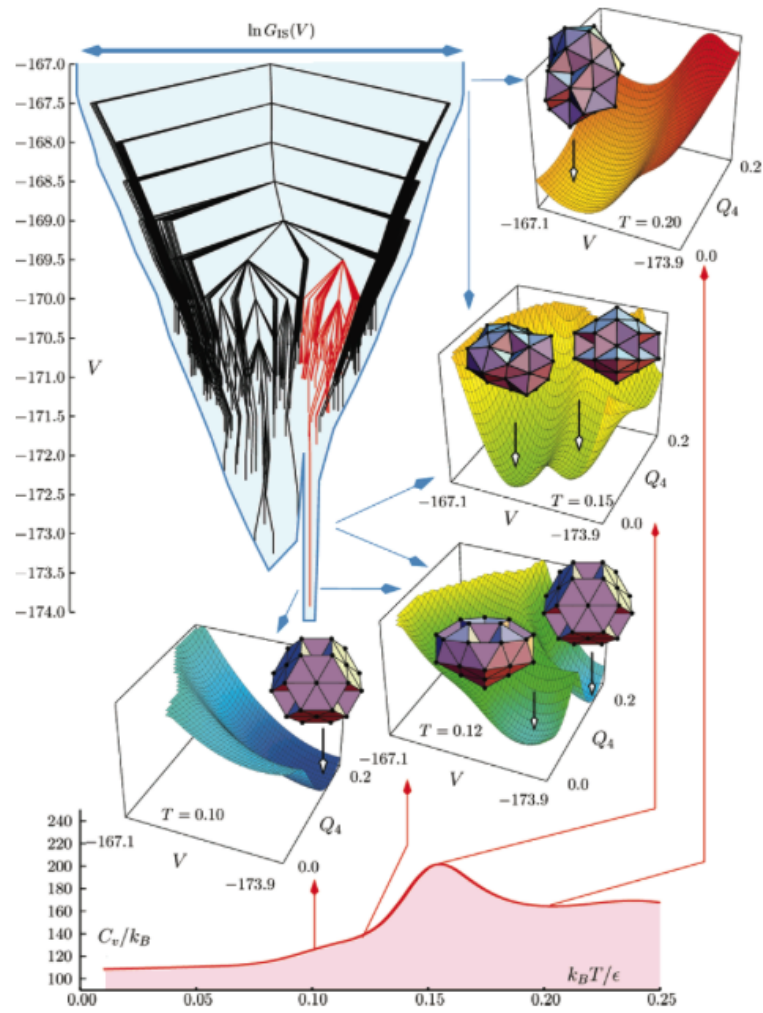


Fig. 1.2 Disconnectivity graph, heat capacity, and free energy surfaces for LJ₃₈. Figure taken from Ref. [185]

ent types of phase transformations during forming these novel compounds. Therefore, that a good understanding of the mechanism of the pressure induced phase transitions becomes important and would contribute much in guiding these novel materials synthesis experiments in more well controlled and efficient ways.

Acquiring a firm and precise understanding of atomistic mechanisms of structural changes accompanying new phase formation at high-pressure remains a challenging problem. Specifically, detailed understanding of local structural rearrangement induced by pressure of a structural reconstruction transition, in the phase coexistence regime accompanying with the nucleation phenomenon, still requires grappling with the problem for a long time. There are various method for solving the problem, we here mainly introduce two methods, that many other modern approaches based on, the Landau theory and the transition state theory.

1.4.1 Landau theory

Many approaches have been developed trying to generally describe structural phase transitions in the solid state. Landau theory [86, 170] coupled with the “soft mode” concept is proposed as a free energy based approach, which has been developed to formulate a general theory of continuous (i.e. second-order) phase transitions. It gives a very simple yet highly useful picture for displacive/second-order transformations, with only one single order parameter. Later, the approach was extended to cover first-order transitions [171].

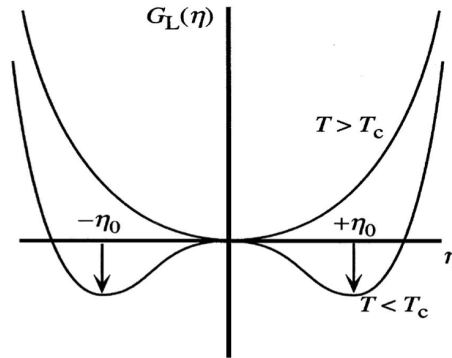


Fig. 1.3 Landau free energy for temperatures above and below the transition temperature. The equilibrium value of the order parameter η is given by the minimum of the free energy. At high temperatures ($T \geq T_c$) there is only one single minimum at $\eta = 0$. At low temperatures ($T \ll T_c$) the free energy has a maximum at $\eta = 0$ and minima at non-zero values of $\eta = \pm\eta_0$.

In the Landau approach, a variable η is associated with a phase transition to describe the transformation process, known as an order parameter. This variable is supposed to contain all the information about the degree of order or extent of deformation during the transformation.

1.4 Structural phase transition

In principle, the order parameters of the Landau theory can be obtained from a microscopic model.

The basic idea of Landau theory method is that many phase transitions are able to be described with terms of relatively few phenomenological constants. Thus, the free energy of the system can be Taylor-expanded into terms that couple η with these phenomenological constants, or physical quantities (such as strain, temperature and spin directions). The expansion is truncated at the lowest sufficient order and the behavior of η and the coupled quantities can be obtained from the free energy using standard thermodynamic relations. The pertinence of Landau theory relies on the appropriate definition of the order parameter. Once η is defined, the Landau free energy can be written as:

$$G(\eta) = G_0 + A(T - T_c)\eta^2 + B\eta^4 + \dots \quad (1.16)$$

This causes the appearance of secondary minima that become the global minimum on lowering the temperature. In first order transitions, the order parameter discontinuously jumps from zero to a non-zero value, accounting for phase coexistence.

It is in this sense that Landau theory has proven to be so powerful: a wide range of fundamental relationships can be derived, with coefficients that are usually obtained by fitting experimental data [38]. Landau theory is a mean-field method, which makes remarkable success in the field of continuous transformations. However, it represents a major drawback in studying first-order transformations, such as flattening local fluctuations into averages. Moreover, the nucleation and growth phenomena, which are very common in phase transitions, could not be accounted for either.

1.4.2 Transition state theory

The classical transition state theory (TST) has been developed [45, 193] for solving the problems of the transitions between two stable states. The basic idea of TST is the assumption of a dividing energy surface, which is known as potential energy surface (PES), between the two investigated stable states in the configuration space. On the PES, the two stable states are defined as separated adjacent sets. TST focus on the searching for dynamical bottlenecks on PES that the system passes through during the transition. Thus, the validity of the TST relies on the choice of an “effective” PES in configuration space.

A rare event (phase transition or chemical reaction) must have sufficient energy to overcome a potential energy barrier (the activation energy) to occur within TST . When the phase transitions that lead to reactions are described, they are under a static picture (classic mechanic picture) and the details of the atomic vibration are lost.

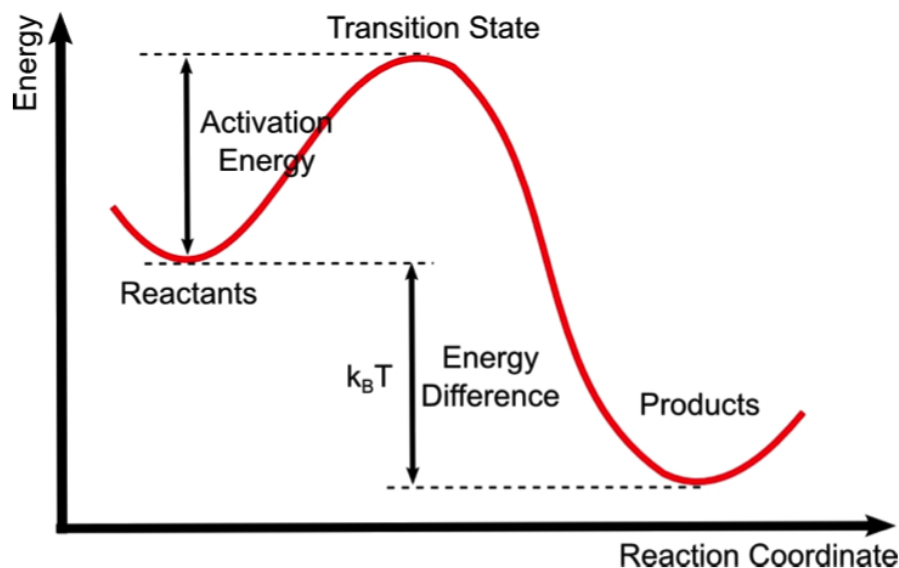


Fig. 1.4 Schematic illustrating the crossover between two different states in the framework of transition state theory.

Within TST, the problem of studying the dynamic processes of the transition becomes to find the free energy barrier for the transition. Such dynamical information could be retrieved from the free energy F as a function of a reaction coordinate which is assumed to describe the progress of the transition process. Within the harmonic approximation to TST [180, 191], the problem of the transition dynamics investigation becomes to search the saddle point on the PES that takes the system from one potential energy minimum (initial state) to another (final state). The transition dynamics can be identified with the algorithms considering a series of gradients of the PES, when the system is dominated by energetic effects. Saddle points are thus determined by the enumeration of the stationary points on the PES. The structure at the saddle point is named as “transition state”.

TST is widely applicable in studying how chemical reactions and phase transitions take place, but it has limitations and does fail in some situations. First, one basic and important assumption of TST is that atomic nuclei should behave according to classical mechanics [45]. It is assumed that unless atoms or molecules collide with enough energy to form the transition structure, then the reaction does not occur. However, according to quantum mechanics, for any barrier with a finite amount of energy, there is a possibility that particles can still tunnel across the barrier. With respect to chemical reactions this means that there is a chance that

molecules will react even if they do not collide with enough energy to traverse the energy barrier [111]. While this effect is expected to be negligible for reactions with large activation energies, it becomes a more important phenomenon for reactions with relatively low energy barriers, since the tunneling probability increases with decreasing barrier height. Second, transition state theory also has limitations in describing some reactions at high temperature. TST is a zero-temperature method, that assumes the reaction system passes over the lowest energy saddle point on the PES. Thus, TST gives good description for reactions occurring at relatively low temperatures. While for cases at high temperatures, higher energy vibrational modes becomes more important. the complex motion and collisions may lead to transition states far away from the lowest energy saddle point, which is out of the ability of TST method.

1.5 Universal Structure Predictor: Evolutionary Xtallography

USPEX is short for “**U**niversal **S**tructure **P**redictor **E**volutionary **X**tallography”. The initial motivation for the development of USPEX is for achieving the crystal structure prediction in inorganic materials. Now, USPEX has grown to a multi-method software platform, that includes evolutionary algorithm, random sampling, evolutionary metadynamics, improved PSO (Particle Swarm Optimization) methods for structure predictions, VC-NEB and TPS approaches for phase transition mechanisms and many other new features in material research and design.

The USPEX method, at first, employs an evolutionary algorithm devised by A. R. Oganov and C. W. Glass, and inspired by the discovery of the post-perovskite structure of MgSiO_3 in 2004, which has been made independently by two groups in 2004 and has significantly changed models of the Earth’s mantle structure [120, 128, 174]. The *First Blind Test of Inorganic Crystal Structure Prediction*[124] shows that USPEX outperforms other methods in terms of efficiency and reliability. The method continues to be rapidly developed. In addition to crystal structure prediction, USPEX can work in other dimensionalities and predict the structure of nanoparticles, polymers, surfaces, interfaces and 2D-crystals. It can very efficiently handle molecular crystals (including those with flexible and very complex molecules) and can predict stable chemical compositions and corresponding crystal structures, given just the names of the chemical elements. In addition, new methods have been developed for revealing the phase transition pathway and mechanisms, which enable USPEX to perform materials prediction and guide experimental synthesis under a broader view and more comprehensive paradigm.

USPEX has been applied to a number of important problems, many new results were obtained. Over 250 papers were written on USPEX or using its methodology. Its significant success and efficiency draws from the carefully designed frame of the algorithms (type of selection, niching, softmutation, etc.) and problem-specific variation operators, while its reliability is largely due to the use of state-of-the-art *ab initio* simulations inside the evolutionary algorithm. USPEX method/code is regularly updated and has been used by over 2300 researchers worldwide, due to its extremely good efficiency and reliability. The code is mainly contributed by C. W. Glass, A.O. Lyakhov, Q. Zhu, G. R. Qian, M. Rakin and many other people.

As a mature and widely used code, USPEX now evolves to support a maximally simple input. A few parameters are needed to perform the prediction and simulation, like the atoms of each sort, pressure-temperature conditions, algorithm parameter values, and types of energy calculation used. A number of new techniques are implemented to improve the user-friendliness of USPEX code. For instance, the *Autofrac* method enable an automatic evolution of variation operators (lattice mutation, atomic permutation and heredity, etc). A special algorithm that accurately estimates the cell volume at the pressure, available for all predictions for crystals, molecules and polymers, helps users to get rid of any preparing work before running a USPEX calculation. The use of specially designed fingerprint functions for niching helps to speed up structure search and prevents sticking to local minima, which ensure the USPEX is robust for all systems. One of the most popular features, which has been achieved first and best in USPEX, is to perform variable-composition simulations, where one specifies only the atomic types, and USPEX should find both the stable compositions and the corresponding structures. Right now, the prediction for structures of low-dimensional objects - nanoparticles and surfaces, and of packing of molecules in molecular crystals are available and have been released.

Chapter 2

Crystal Structure Prediction

2.1 Crystal structure prediction with evolutionary algorithm

The development of reliable and robust methods for crystal structure prediction has been a goal of the physical, chemical and biological sciences since the 1950s [36]. Many computational methods were employed in predicting the atomic/molecular-level structures and properties of compounds. The evolutionary algorithm (EA) is one of these successful approaches, which is capable of solving the global optimization problem up to a few hundred degrees of freedom, and running the configuration search in the energy landscape.

The evolutionary algorithm (EA) is one of the most popular artificial intelligence approaches. Evolutionary algorithms show significant success in diverse fields, owing to no assumption about the underlying fitness landscape and learning power. This generality is shown by successes in fields as diverse as engineering, art, biology, economics, marketing, genetics, operations research, robotics, social sciences, physics, politics and chemistry. When the evolutionary algorithm is applied to structure prediction problems, the “individual” is simply a configuration, or candidate structure, with the lattice parameters and atomic coordinates. New candidate structures are generated, through procreation, by applying two operators: “crossover” to pairs of candidate structures, so combining current structural features into new individuals, and “mutation” to individual candidate structures, so possibly introducing new structural features to the population.

Many comparable population-based metaheuristic intelligence approaches, like swarm algorithms (especially particle swarm optimization, short for PSO), are also suitable for solving the structure prediction problem. However, the EA approach shows more success currently in crystal structure prediction problems because :

- 1) The EA is widely used, and the algorithm has been studied well, as well as the limitations.

2) The procedure involves physically motivated variation operators: Heredity process is like a chemical reaction, and mutation is more like a phase transition process, which are the two main way to produce materials.

2.2 Crystal structure prediction in USPEX

To implement the EA in crystal structure prediction, the main task is to find the genotype-phenotype distinction and create effective variation operators (heredity and mutation) specifically for crystallography.

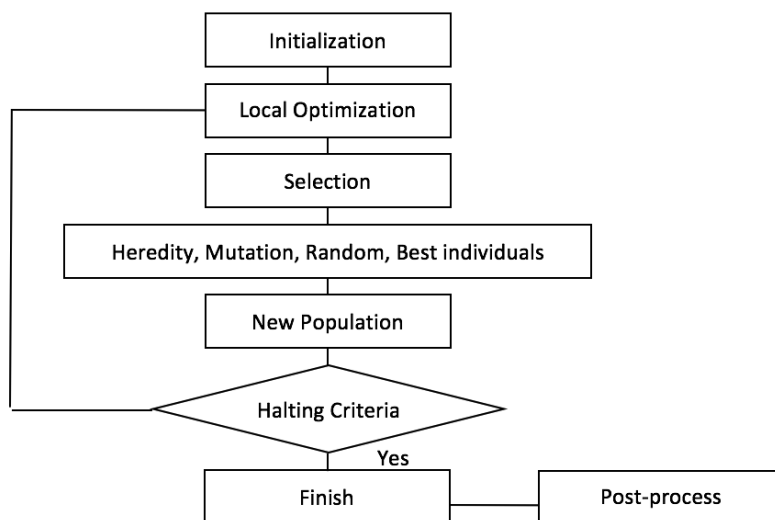


Fig. 2.1 Illustration of the evolutionary algorithm for crystal structure prediction in USPEX.

Simple EA can solve often complex problems, thus it seems that there may be no direct link between algorithm complexity and problem complexity. However, in most real applications of EA approach, computational complexity is a prohibiting factor, which usually comes from the fitness function evaluation. For crystal structure prediction with EA, the major computational complexity is a precise fitness evaluation, especially under first principle framework. Thus, besides the implementation of full function EA procedure in crystal structure prediction, techniques in reducing the searching configuration space, accelerating the speed, increasing the success ratio and overcoming the premature problem are also important to combining with the knowledge of the crystallography. USPEX gives a good and very efficient solution of these topics.

As shown in Fig. 2.1, the procedure of USPEX for crystal structure prediction is implemented as:

- (1) Initialization of a set of crystal structures as the first generation, which satisfies the hard constraints and is randomly generated at some conditions;
- (2) Determination of the quality for each member of the population using the so-called fitness question;
- (3) Selection of the best members from the current generation as parents from which the structures of the new population are created by applying specially designed variation operators.
- (4) Evaluation of the quality for each member of the new population.
- (5) Repeat steps 3-4 till the halting criteria are achieved.

In this chapter, a simple overview of the basic knowledge and main feature of crystal structure prediction in USPEX will be introduced. The following sections are mainly based on the book *Modern Methods of Crystal Structure Prediction* (edited by Artem R. Oganov)[124] and relevant reference of USPEX [98, 125, 127, 203, 204].

2.2.1 Variation operators

To keep the approach intuitive, we represent lattice vectors and atomic coordinations by real numbers, instead of binary strings. Such a genotype-phenotype encode method makes the search space continuous and shows great success and convenience in variation operator design.

At the beginning of applying EA for structural prediction, the initial structures are usually generated randomly. To produce the more reasonable structures and reduce the complexity of configuration space, we also applied the structural initialization strategy by considering the crystal symmetry and space group constraint. According to randomly selected space groups method approach, we randomly pick one of 230 space groups to set up a Bravis cell according to the specified initial volume with random cell parameters consistent with the space group, then initialize the atoms occupying special Wyckoff positions.

To deliver the good gene to the next population with EA, the design of different variation operators is the most important step. There are mainly two types of variation operators, heredity and mutation, and many variants of these two operators are proposed.

For the operators in EA approach, heredity is the core part. The heredity operator first chooses planes which are parallel to one lattice plane along the other lattice vector from different parents, and then cut the structures and match the slices. When the child structure is generated, it delivers different parts of the crystal information from different parents. In the child structure, the number of atoms of each kind should be adjusted to be conserved.

Mutation operators use a single parent to produce a single child. It has several variant forms — lattice mutation, softmode mutation and permutation. Lattice mutation applies stain

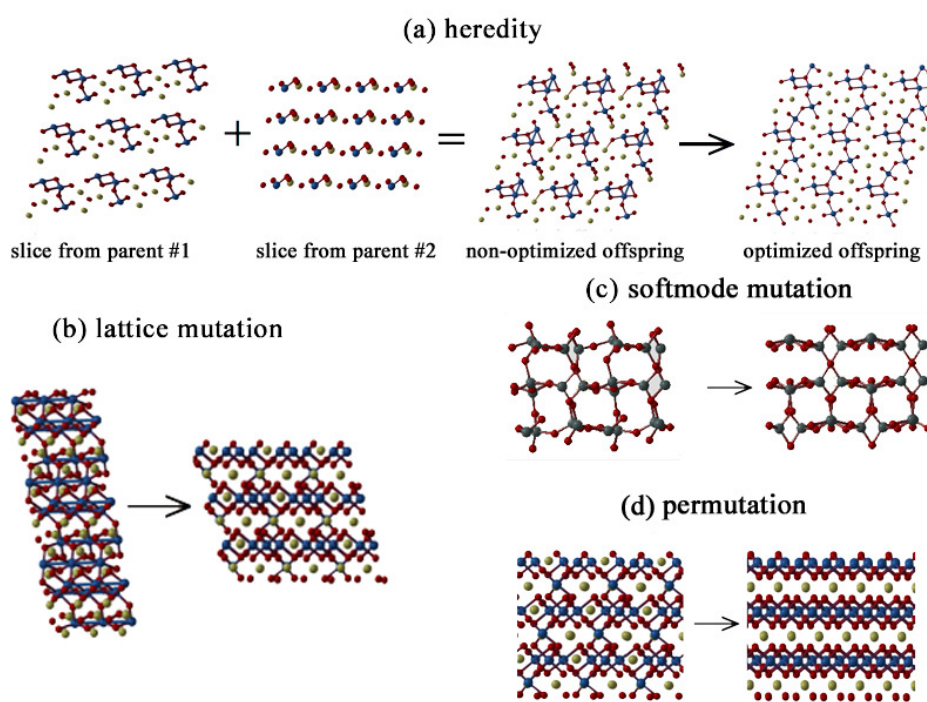


Fig. 2.2 Illustration of variation operator used in USPEX, (a) heredity, (b) lattice mutation, (c) softmode mutation, (d) permutation. Figures taken from Ref. [127]

matrix with zero-mean Gaussian random strains to the lattice vectors; softmode mutation displaces the atoms along the softest mode eigenvectors, or a random linear combination of softest eigenvectors; permutation operator swaps chemical identities of atoms in random pairs.

The variation operations in USPEX are shown in Fig. 2.2.

2.2.2 Fingerprint technique

Premature convergence often happens in EA, where a population for an optimization problem converged too early, resulting in getting stuck in some local minima but not the global minimum. Such behavior is especially common for energy landscapes with many good local minima. This is due to the fact that good structures tend to produce children in their vicinity, and cause the loss of genetic variation. The key to prevent the premature convergence is to control the diversity of the population to generate offsprings that are superior to their parents.

Different from other EA application, direct comparison of the gene representation for crystal structures does not work since crystals could be represented in lattice vectors units in many equivalent ways in choosing different shapes of the unit cell. Thus before solving the premature convergence problem, new technique for identifying similar structures and measuring the similarity quantitatively needs to be provided.

In USPEX, the fingerprint function [129] is used to describe the structure characteristic of a crystal structure. The fingerprint function has the features such as :

- 1) directly and only derived from the structure, rather than its properties,
- 2) invariant with respect to shifts, rotation, and reflections in the coordinate system;
- 3) sensitive to different orderings of the atoms;
- 4) formally related to experiment;
- 5) robust against numerical errors.

The fingerprint function has the formulation very similar to radial distribution function (RDF), which is expressed as:

$$f(R) = \sum_i \sum_{j \neq i} \frac{Z_i Z_j}{4\pi R_{ij}^2} \frac{V}{N} \delta(R - R_{ij}) \quad (2.1)$$

where Z_i is the atomic number for atom i , R_{ij} is the distance between atoms i and j , V is the unit cell volume, and N is the number of atoms in the unit cell. The index i goes over all

atoms in the unit cell and index j goes over all atoms within the cutoff distance from the atom i . To remove the fingerprint dependency from cutoff distance, the function is normalized as:

$$f_N(R) = \frac{f(R)}{\sum_{i,j} Z_i Z_j N_i N_j} - 1 \quad (2.2)$$

where N_i is the number of atoms in the unit cell with atomic number Z_i .

The similarity between different structures can be estimated by the cosine distance between two fingerprint functions,

$$d_{ij} = 0.5 \left(1 - \frac{f_i f_j}{|f_i| |f_j|} \right) \quad (2.3)$$

The selection rules and variation processes above can also be improved with this new crystallographic descriptor. A similarity criteria is set in USPEX to identify all similar structures, and ignore them to only choose different ones. Many other features and benefits from fingerprint theory could be found in Ref. [129].

2.3 Novel methods and extensions in USPEX

With the powerful EA and well designed variation operators, the USPEX method has been widely successfully applied in various systems, and the success rate and efficiency is also quite encouraging. Many other advanced methods and new techniques have been developed for very large and complex crystal structure prediction, including randomly symmetric structures generation, smarter variation operators design according to local environments, anti-aging and anti-seeds technique, etc. The novel features and performance of USPEX could be found in Ref. [98], where it indicates that USPEX outperforms other methods in terms of efficiency and reliability.

Although the standard framework of EA in USPEX is very powerful, new ideas can frequently come out to solve the more complicated problems and different types of realistic problems, which are beyond the abilities of traditional crystal prediction concerns. Several new features and extensions are introduced below:

Variable composition prediction Beyond the standard framework of crystal structure prediction, the simultaneous prediction of all stable stoichiometries and relevant structures are also enabled in USPEX. The idea of stoichiometry prediction was first proposed by Johnneson et al [73], who succeeded in predicting stable stoichiometries in alloy systems within fixed structure types. This pioneering study indicates that prediction of a complex landscape consisting of both compositional and structural coordinates is possible for crystals.

The example for complicated A-B system working with Lenard-Jones potential are shown in Fig. 2.3.

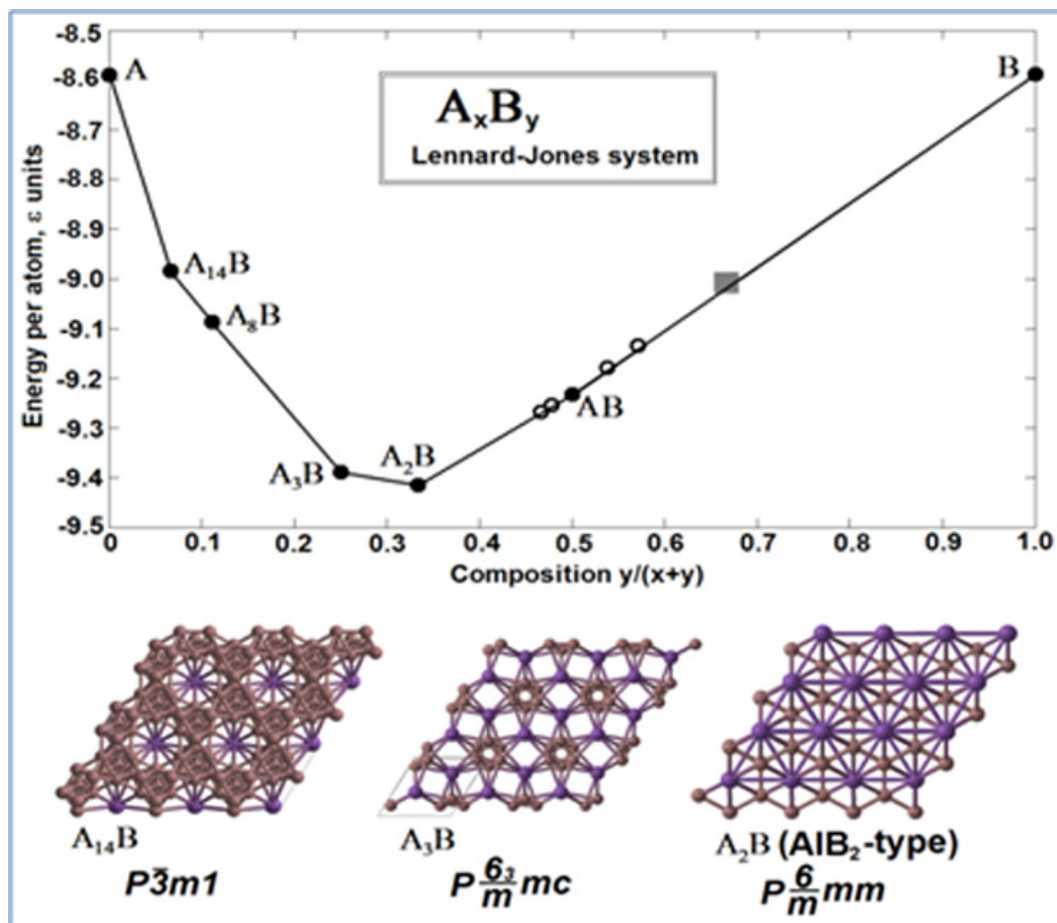


Fig. 2.3 A variable composition prediction in a binary Lenard-Jones system. Solid circles denote ground states, while open circles denote metastable solutions. The figure is taken from Ref. [127]

Molecular crystals predictions Another challenging yet very interesting topic in materials science is crystal prediction of the molecular crystals. Molecular crystals are extremely interesting due to the wide applications in the field of pharmaceuticals, pigments, explosives, and metal-organic frameworks. Quite different from problems in inorganic crystals, the prediction of stable organic structures can be achieved under the constraint of fixed molecules (or partially fixed as flexible molecules) as building blocks [203], instead of assembling the structures from single atoms. The variation operators, heredity and mutations, are also

improved to follow the constraint to keep the molecules as a whole block, only flexible for internal angles and bond length. A new variation operator, “rotational mutation” of the molecular blocks, is introduced in molecular crystal prediction as well. More details and performance of the method can be found in Ref. [203].

Two dimension systems and clusters The topic of structure prediction for low dimension systems is also attractive. Lots of novel physics and chemistry can be achieved by simply reducing the dimensionality of materials for two dimension (2D) or cluster systems. For 2D and cluster predictions, enough “vacuum” needs to be inserted to eliminate the interaction between its periodic structures, which is the popular model and widely used in most codes.

Surface structure predictions Similar to 2D system, the prediction of surface structure and reconstruction is another type of low dimensional situation. The difference from pure 2D problem, the substrate is taken into account in surface predictions, which yet is not considered by the variation operators. The established convex hull for multicomponent system is also different from bulk [202] in variable composition simulations, due to stability on surface value of the chemical potential.

Magnetic materials predictions To reveal the ground state for magnetic materials, a full magnetic state configuration space search is applied to extended when performing the real space structure predictions. For a magnetic material, it normally adapts a magnetic phase as ferromagnetic (FM) or anti-ferromagnetic (AFM). The nonmagnetic (NM) state is also considered, because the magnetic transition and collapse usually occurs at high pressure leading to the NM state. For a polarized situation, the electrons can also stay at different spin states, high spin (HS), low spin (LS) and a mixed high and low spin (LH) states when the competition of the crystal field splitting energy and the spin-pairing energy exists. Therefore, the different magnetic type and spin state classifications are considered during the process of the structure and magnetic state initialization, structural heredity, mutation and permutation operators in USPEX method, to predict an accurate predictions of magnetic states. A novel magnetic mutation operator “spinmutation” for magnetic configuration space search is also developed in USPEX, where different magnetic states would mutate to each other with a user-defined ratio.

Coevolution method for large scale and complicated systems When dealing with large scale structure prediction problems — with complicated multicomponents or under various pressure ranges, the task of structure calculations is usually heavy in USPEX. A number of

2.3 Novel methods and extensions in USPEX

similar yet independent calculations are run for different situations, which normally bring huge number of duplicated or similar structures. To accelerate the calculations and increase the success rate, independent USPEX calculations could be run separately, but in a global coevolutionary search with exchanging good (stable and some metastable) structures between different runs. Calculations for similar structures will be avoided and the diversity of the structures can be kept in different USPEX calculations, when combining the “anti-seeds” [98] techniques. This coevolutionary method on top of the EA approach is very efficient and has been implemented in USPEX.

Chapter 3

Structural Phase Transition Mechanism Investigation

3.1 Reconstructive structural phase transition

According to Buerger's phase transition classification [19], some of the structural phase transformations are "displacive", some are "reconstructive" and yet some are "order — disorder". The classification was simply assumed from comparisons of the initial and final structures, not based on experimental investigations of the phase transition process. In "displacive" transitions, the atomic positions change by fairly small amounts, without breaking the primary bonds in order to interconvert crystal structures. Thus, these transitions normally show only a small amount of hysteresis, accompanying small or vanishing enthalpy and volume changes. Some displacive transitions are induced by a "soft-mode" mechanism, in which the frequency of a vibrational mode drops towards zero induced by pressure or temperature. Displacive transitions are also topotactic, where the space group symmetries of the two phases show a group/subgroup relationship.

Among the "reconstructive" transitions, the transformations involve large structural changes, including rearranging of the atoms, breaking and reformation of chemical bonds, and any change of space group is allowed. The corresponding activation energies are usually quite high, and normally show a large hysteresis and in some cases they are irreversible. Thermodynamically, reconstructive phase transitions show a "jump" feature of the enthalpy and volume changes at the transition pressure/temperature, where there are discontinuities in the first-order free energy derivatives (entropy and volume) as a result of the change in the atomic environment. Displacive transitions show second-order or weak first-order thermodynamic character. It is also common that there is sometimes a coexistence of phases at equilibrium, hysteresis and metastability of the intermediate phases.

From the symmetry aspects of Buerger’s phase transitions classification, there is no clear order parameter in the “reconstructive” transitions. However, any crystallographic mechanism of the transformation can be describable using an intermediate structure whose space group is subgroup of both space groups of the two end phases. Moreover, the intermediate state transforms continuously from one to the other end phase, according to the change of the “reaction coordinate”, or kinetic order parameter. For example, coordination number (CN) is often used as an order parameter for identifying the phase transition. The CN changes as $4 \rightarrow 6 \rightarrow 8$ in zincblende ($F-43m$) to rocksalt ($Fm-3m$) to CsCl-type ($Pm-3m$) structures in binary AB systems. The tetrahedral order parameter [28] can be used to describe many types of phase transition, like phase transitions in water-ice, graphite to diamond [76] and other structure transitions.

With the well-designed order parameter for reconstructive phase transition, Investigation from the static, geometric, concentrated, and mean field approaches are developed for revealing the “classic” picture of the phase transition mechanism. Methods based on molecular dynamics simulations and using an advanced method, like transition path sampling, are working on the mechanistic elucidation of transformation mechanisms from nucleation and growth phenomena. However, it is still challenging to study the transformation mechanism even in a simple system, because there is no very general way and a standard pipeline to explore them. Every investigation for phase transition pathway is system-dependant, from the order parameter design, space group symmetry analysis and procedure of the simulations.

In this chapter, we will introduce the approaches — the evolutionary metadynamics (EV-metadynamics), VC-NEB and TPS methods — implemented in USPEX for studying phase transition mechanism and pathway investigations. These methods reveal the transition mechanism at different levels, and an epitome will be introduced for studying a phase transition with these methods as a general procedure. The methodology description of evolutionary metadynamics and transition path sampling is mainly based on Qiang Zhu’s evolutionary metadynamics [204] and Dellago’s papers [32–35].

3.2 Evolutionary metadynamics method

Metadynamics is a free energy surface exploration approach. It performs efficiently to capture the properties of the multidimensional potential energy surface (PES), instead of exploring the specific crossing pathway between two known stable states. It is usually applied within molecular dynamics (MD) simulations and starts from an initially prepared state, while no assumptions are made for the final state on the energy landscape. Thus, metadynamics is an open-end method.

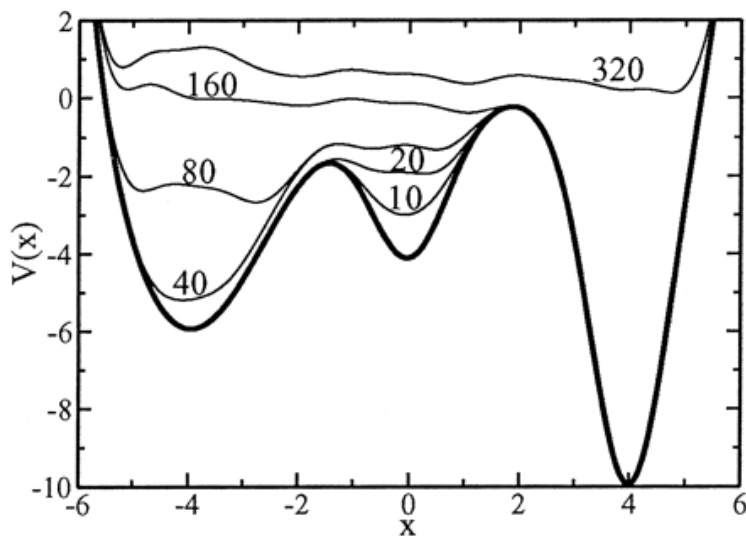


Fig. 3.1 The dynamic evolution (thin lines) labeled by the number of dynamical iterations of free energy minima flooding using metadynamics method. Figure taken from Ref. [85]

The basic idea of metadynamics can be described as “filling the free energy wells with computational sand”. Fig. 3.1 illustrates how the evolution of metadynamics goes. By introducing a history-dependent potential term, metadynamics method fills the minima in the PES and allows efficient exploration of the PES as a function of the system-dependent collective coordinates [85]. Metadynamics simulation greatly improves the sampling of a system combining with the powerful MD technique, where ergodicity is hindered by the complex energy landscape.

Metadynamics has been widely used in various fields, such as phase transitions [109, 110], chemical reactions [41], protein folding [138] and molecular docking [51, 179]. Martonak et al. used the edges of the simulation cell as collective variables (CV) for the study of pressure-induced structural transformations [110]. The local minimal (neighborhood basins near the start states) can be found on the PES by crossing the energy barriers, and the transformation kinetic process will be crudely pictured by detecting the shape of the PES [85, 110]. Metadynamics method is also considered to be a powerful and efficient structure prediction method, but it relies on availability of a good starting structure.

However, the MD technique at each metadynamics metastep for equilibrating the system is not always an efficient method for equilibration, which could lead to trapping in metastable states and bring amorphization of the system rather than transition to another stable crystal structure. Thus, the new method Evolutionary Metadynamics (EV-metadynamics) is proposed by Zhu et al. [204]. With more efficient and robust global optimization moves,

this technique is a general metadynamics-like method driven not by local MD sampling. Following Martonak’s idea. [110], EV-metadynamics also adopts the cell edges as collective variables for structural phase transformations. The equilibration of the system at each value of the collective variables is done with a “soft-mutation” operator [99] used as the evolutionary variation operator in USPEX, rather than previously used MD simulation. It also has been found that the EV-metadynamics is very efficient for predicting stable and low-energy metastable states and avoids amorphization.

3.2.1 Evolutionary metadynamics method

Same as metadynamics for crystal systems, the collective variables of cell box h (3×3 matrix) [110] are used describe the evolution of the system in evolutionary metadynamics. Then the PES is defined in this reduced space of the collective variable. For a given system with volume V under external pressure P , the derivative of the free energy G with respect to h is

$$-\frac{\partial G}{\partial h_{ij}} = V[h^{-1}(P - p)]_{ji} \quad (3.1)$$

where p is the internal pressure tensor calculated for each given geometry.

The collective variable evolves with a stepping parameter δh ,

$$h(t + 1) = h(t) + \delta h \frac{f(t)}{|f(t)|} \quad (3.2)$$

here the driving force $f = -\frac{\partial G}{\partial h}$ is from a history-dependent Gibbs potential $G(t)$ where a Gaussian has been added to G^h at every point $h(t')$ already visited in order to discourage it from being visited again,

$$G(t) = G^h + \sum W e^{-\frac{|h-h(t')|^2}{2\delta h^2}} \quad (3.3)$$

As the simulation proceeds, the history-dependent term fills the initial well of the PES, and concurrently the collective variables (the cell) undergo a sequence of changes, at each of which the atoms are re-equilibrated. At some critical cell distortion atoms rearrange dramatically, yielding a new crystal structure.

Instead of applying the MD simulations to move the atoms aimlessly to equilibrate structures, the atoms are moved along the eigenvector of the softest calculated mode [99, 125, 126] in evolutionary metadynamics [204]. This is the same as the softmutation operator in USPEX. By properties of normal modes, the displacement of the atoms is clear and predictable. Therefore, the original and softmutated structures are usually connected with

a group-subgroup symmetry relations, even sometimes causing a higher symmetry due to the structure relaxation. In this case one observes a structural transition with a common subgroup, which is not clear in metadynamics with MD technique. To calculate the vibrational modes, the dynamical matrix is constructed from bond hardness coefficients.

$$D_{\alpha\beta}(a,b) = \sum_m \left(\frac{\partial^2}{\partial \alpha_a^0 \partial \beta_b^m} \frac{1}{2} \sum_{i,j,l,n} H_{i,j}^{l,n} (r_{i,j}^{l,n} - r_{0,i,j}^{l,n})^2 \right) \quad (3.4)$$

Here coefficients α, β denote coordinates (x, y, z) ; coefficients a, b, i, j describe the atom in the unit cell; coefficients l, m, n describe the unit cell number; $r_{i,j}^{l,n}$ is the distance between atom i in the unit cell l and atom j in the unit cell n , while $r_{0,i,j}^{l,n}$ is corresponding bond distance, and $H_{i,j}^{l,n}$ is bond hardness coefficient computed from bond distances, covalent radii and electronegativities of the atoms [89, 99].

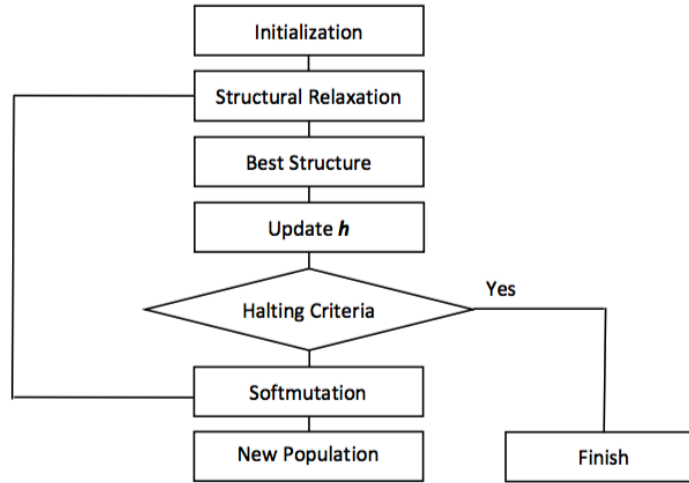


Fig. 3.2 Illustration of the evolutionary metadynamics algorithm [204].

The algorithm of the evolutionary metadynamics technique is shown in Fig. 3.2, and is in many ways similar to the original version by Martonak et al. [109]. Due to the presence of a population of structures and a selection step, this algorithm is evolutionary, unlike original metadynamics [109].

(1) The simulation starts with one known initial structure at given lattice h and external pressure P , and then computes all the vibrational modes of the system.

(2) New structures with atoms softmutated are relaxed at constant h , the lowest-enthalpy structure is selected and its pressure tensor p is computed.

(3) The old lattice box h is then updated according to Eq. 3.2 to have a new h' .

(4) A new generation of softmutated structures are produced and relaxed in the fixed cell h' .

(5) Repeating step (3)-(5) for a number of generations, this computational scheme leads to a series of structural transitions and is stopped when the maximum number of generations is reached.

3.2.2 Transition sequence from evolutionary metadynamics

MD method is widely used to study physical processes in liquids and solids [132], but has difficulties in escaping from local energy minima and crossing high energy barriers [183]. Metadynamics [85] is an ingenious way to solve this problem and accelerate the activated processes involving barrier crossing, which helps in revealing transformation sequences and the saddle points between the local energy minima states. The EV-metadynamics technique accelerates the escaping possibility of metastable phases to finish the neighbor search continuously without amorphization, which makes the EV-metadynamics technique a crystal structure prediction method. With loss of energy landscape scanning ability, no accurate height of the saddle point from the collective variables (CVs) configuration space and the details of transformation mechanism can be pointed out during the EV-metadynamics simulations during the structural phase transition.

On the other hand, the way of moving the atoms following the softest mode includes a clear group-subgroup symmetry relation of these predicted metastable/stable structures. Thus, a phase transition sequence tree can be indicated through the EV-metadynamics simulations, which cannot be observed in metadynamics calculations.

The EV-metadynamics calculation of SiO_2 system shows the power of this method [204]. In Fig. 3.3, EV-metadynamics calculation observed a sequence of phase transitions in SiO_2 using the GULP code with the BKS potential [177]. Starting from a 72-atoms supercell of α -quartz (space group $P3_121$), α -quartz first transforms to quartz II (C2), and then quartz II amorphizes until it transformed into the anatase structure ($I4_1/amd$). Anatase amorphizes again, and eventually evolves into the $3 \times 2 P2_1/c$ structure and then transforms into stishovite ($P4_2/mnm$). The EV-metadynamics simulation unravels a very non-trivial transition sequence through α -quartz \rightarrow quartz II \rightarrow anatase structure $\rightarrow 3 \times 2 P2_1/c$ structure \rightarrow stishovite. As a bonus, the amorphous stages in quartz II \rightarrow anatase structure and anatase structure $\rightarrow 3 \times 2 P2_1/c$ structure indicate a complicated phase transition mechanism and high energy barrier during the transformation.

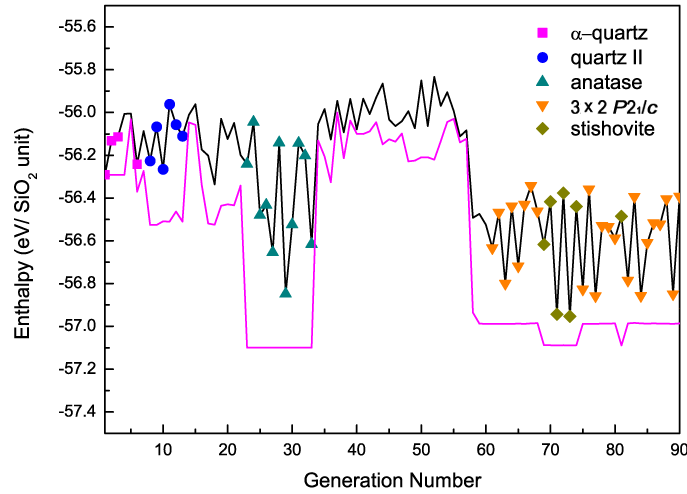


Fig. 3.3 Enthalpy evolution during the compression on 72-atom supercell of α -quartz (SiO_2) at 10 GPa (black line: enthalpies for best structures with constant h ; magenta line: enthalpies for best structures after full relaxation). Figure taken from [204]

3.3 Variable-Cell Nudged Elastic Band Method

Nudged elastic band (NEB) method is a two-end method. The NEB method [47, 62, 63, 118, 119], as a widely used method for solving double-ended problems, is an efficient and robust approach for seeking the reaction paths and saddle points along the “minimum energy path” (MEP) on the potential energy surface between the two endpoints. The NEB method has been successfully applied to molecular chemical reactions [47, 118], surfaces [62, 63], and defect migration [156], in particular it could provide the energy barrier between the given initial and final states of a phase transition process. Some improvements have been presented to enhance the robustness and to raise the efficiency of the NEB method. [62, 63, 107, 156, 163, 173]

The NEB method is a popular technique for studying reaction paths due to its efficiency, but has not been extensively used in solid state physics because of the need to deal with the variation of the unit cell during solid-solid transformations. However, most of the problems treated by the NEB method are considered under the constraint of constant unit cell, which is reasonable for the above mentioned problems, but is not suitable for studying the phase transition mechanisms (which require the variation of the unit cell along the transition path). Solid-state NEB (SSNEB) approach [21] has been developed and applied to the solid-state phase transitions, but the lattice deformation and the displacement of atoms are treated independently within the rapid nuclear motion approximation. A generalized solid-state

NEB (G-SSNEB) method proposed by Sheppard *et al.*[157] investigates the solid-solid transformations involving the unit-cell and atomic degrees of freedom, using a scaled stress with a Jacobian term along the steepest-descent direction and the atomic forces.

We here develop a somewhat different formulation, which is referred as to the variable cell NEB (VC-NEB) method, that treats the cell and atomic coordinates on an equal footing and operates in an expanded configuration space under the constant pressure condition. Here we present an extended technique—a Variable-Cell NEB (VC-NEB) technique combined with *ab initio* calculations. The results reveal that the VC-NEB technique is an efficient and general method and should have wide applications for studying the paths and mechanisms of reconstructive phase transitions. Results of the VC-NEB method can be considered as a starting point for a more sophisticated treatment using the transition path sampling method, the main prerequisite of which is to have an initial transformation trajectory.

3.3.1 Variable-Cell Nudged Elastic Band Method

As in the traditional NEB method, a set of images $\{X_1, X_2, \dots, X_u, \dots, X_n\}$ connecting the two endpoints X_1 and X_n are used to describe the transition path in the VC-NEB method, where X_u is a vector containing the coordinates of the u th image in a special configuration space. Employing the forces orthogonal to the path and the “virtual” springs between the images, finally the image chain would converge to the true MEP to seek the transition routes. Differently from the NEB method, the VC-NEB method expands the configuration space and the force vectors, which has components from the cell and atomic positions transformed to have the same dimensionality. Differently from the G-SSNEB method, the VC-NEB method has its salient feature that the expanded force vectors are always along the gradient of the expanded potential energy surface, which is of great importance for finding the true MEPs.

We describe the unit cell of a crystal by using the variable matrix, which is determined by the matrix of lattice vectors $\mathbf{h} = \{a, b, c\}$, with a cell volume $\Omega = \det(\mathbf{h})$. In the variable-cell technique [132, 137, 190], the finite strain tensor $\bar{\epsilon}$ as a free variable is always chosen, instead of the lattice vector \mathbf{h} , for the sake of convenience. Thus we can replace \mathbf{h}_0 as a reference configuration by $\mathbf{h} = (1 + \bar{\epsilon})\mathbf{h}_0$, where $\bar{\epsilon}$ includes 9 components ϵ_{ij} ($i, j = 1, 2, 3$). The atomic fractional coordinates r_v ($v = 1, 2, \dots, N$) indicate the positions of each v th atom among the total N atoms in the unit cell. The full configuration space is described by the vector $\mathbf{X} = (\epsilon_{1i}, \epsilon_{2i}, \epsilon_{3i}; r_1, \dots, r_N)$ ($i = 1, 2, 3$), with $9 + 3N$ components.

Under the applied pressure P , the enthalpy $H = E + P\Omega$ is determined by the $(9 + 3N)$ -dimensional potential energy surface — the “enthalpy surface”

$$H = H(\epsilon_{1i}, \epsilon_{2i}, \epsilon_{3i}; r_1, \dots, r_N), \quad (3.5)$$

where E is the energy of this structure. The expanded "force vector" in a $9 + 3N$ configuration space can be defined by the derivative of the enthalpy with respect to \mathbf{X} as follows

$$\mathbf{F} = - \left. \frac{\partial H}{\partial \mathbf{X}} \right|_P. \quad (3.6)$$

The strain components of \mathbf{F} on the lattice are the derivatives of H with respect to

$$f_{(\bar{\epsilon})} = -(\sigma + P\Omega)(1 + \bar{\epsilon}^T)^{-1}, \quad (3.7)$$

where σ is the quantum-mechanical stress tensor [122] at a given configuration \mathbf{X} . The forces on atoms, f_1, f_2, \dots, f_N , can be obtained from the Hellmann-Feynman theorem [108]. Finally, the general force \mathbf{F} can be written as [137]

$$\mathbf{F} = (f_{(\bar{\epsilon})}, g f_1, \dots, g f_N)^T, \quad (3.8)$$

where the metric tensor $g = \mathbf{h}^T \mathbf{h}$ is introduced to keep the symmetry during structure relaxation [137, 190].

The tangent vector τ along the path in the NEB method is represented as the unit vector to neighboring images [47, 63, 118]. The transverse components of the potential forces acting on the lattices and atoms are respectively defined as $f_{(\bar{\epsilon})}^{\nabla\perp}$ and $f_v^{\nabla\perp}$. The nudging spring forces on lattices and atoms to keep the image spacings are $f_{(\bar{\epsilon})}^{s\parallel}$ and $f_v^{s\parallel}$. We can now define the VC-NEB force \mathbf{F}^{VC-NEB} , the cell force $f_{(\bar{\epsilon})}^{VC-NEB}$ acting to reshape new image of the cell, and the atom force f_v^{VC-NEB} shifting the atoms

$$f_{(\bar{\epsilon})}^{VC-NEB} = f_{(\bar{\epsilon})}^{s\parallel} + f_{(\bar{\epsilon})}^{\nabla\perp}, \quad (3.9)$$

$$f_v^{VC-NEB} = f_v^{s\parallel} + f_v^{\nabla\perp}, \quad (3.10)$$

$$\mathbf{F}^{VC-NEB} = \left(f_{(\bar{\epsilon})}^{VC-NEB}, g f_1^{VC-NEB}, \dots, g f_N^{VC-NEB} \right)^T. \quad (3.11)$$

In the VC-NEB method, the basic idea is to search the MEPs by studying the "enthalpy surface" instead of the PES in the traditional NEB method. When applying the VC-NEB method to reconstructive phase transitions, the activation path is determined by finding the MEPs on the enthalpy surface in a larger $(9 + 3N)$ -dimensional configuration space, combining the unit cell and atomic variables.

The images along the path are relaxed to MEPs through \mathbf{F}^{VC-NEB} , which contain the transverse components of the potential forces $\mathbf{F}^{\nabla\perp}$ and the spring forces $\mathbf{F}^{s\parallel}$ (Fig. 3.4). The VC-NEB and G-SSNEB methods treat the problem in different metric spaces [146] and have a significant technical difference. In the VC-NEB method, all the components of the general

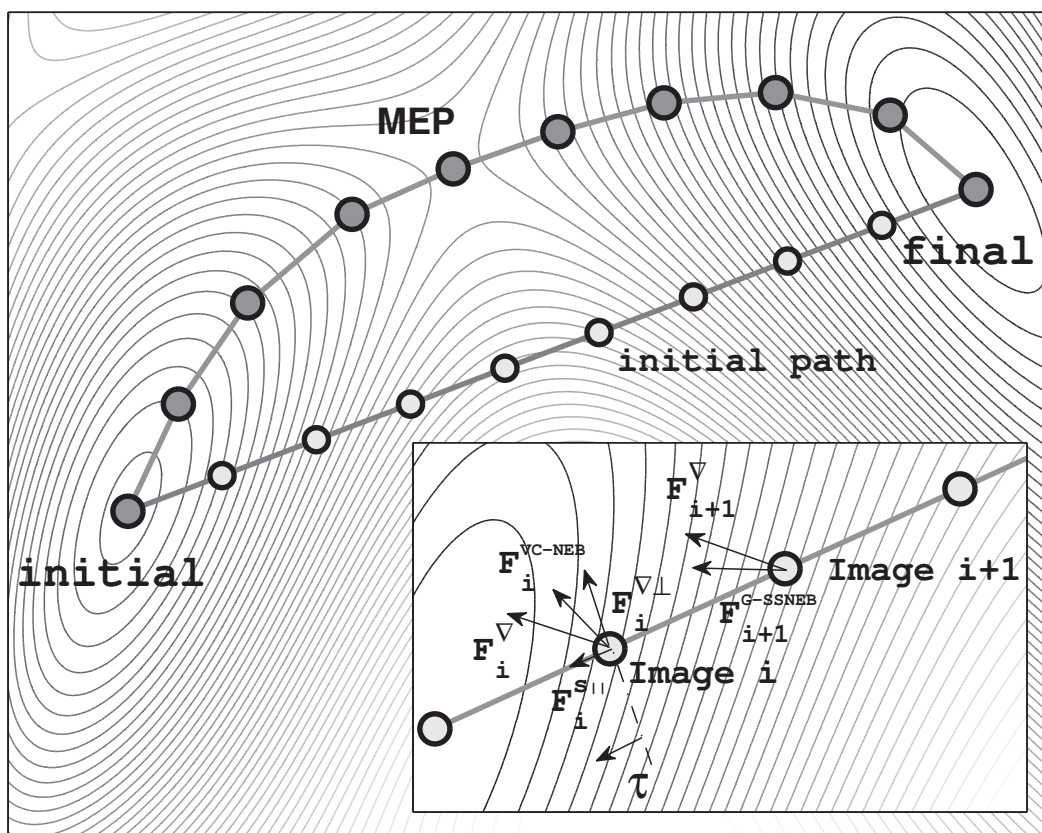


Fig. 3.4 The minimum energy path (line with dash gray circle) and initial path are described on enthalpy surface. The forces in the VC-NEB method on image i are shown in the inset. \mathbf{F}_i^∇ is the potential force in the gradient direction. $\mathbf{F}_i^{\nabla\perp}$ and $\mathbf{F}_i^{s\parallel}$ are the transverse component of \mathbf{F}_i^∇ and the spring force, respectively. The forces on Image $i+1$ indicates the differences between the potential force \mathbf{F}^∇ and $\mathbf{F}^{G-SSNEB}$ in the G-SSNEB method. Figure taken from [143].

forces are along the gradient direction on the enthalpy surface, whereas in the G-SSNEB method which are replaced by the true lattice force (the derivative of energy). For the latter, the computation is implemented under the assumption of an isotropic elastic medium with a Poisson ratio of zero, while this assumption is not needed in our VC-NEB method.

3.3.2 Implementation of the VC-NEB method

Before performing a VC-NEB calculation for a phase transition process with two given endpoint images, its initial path is defined by a set of intermediate images, which are generated by a linear interpolation between the initial and final states or the user-provided specific configurations.

By starting from the initial path, the images are relaxed to the MEP through the VC-NEB force \mathbf{F}^{VC-NEB} , which is derived from the force and stress tensors calculated by the popular *ab initio* codes including GULP [48], Quantum ESPRESSO [52] and VASP [83]. The variable-elastic-constant, improved-tangent-estimate and climbing-image NEB scheme [47, 62, 63, 118, 156] are also implemented in our VC-NEB code for the accurate saddle point determination. The VC-NEB calculation will stop when the user-defined convergence conditions on force and enthalpy have been satisfied.

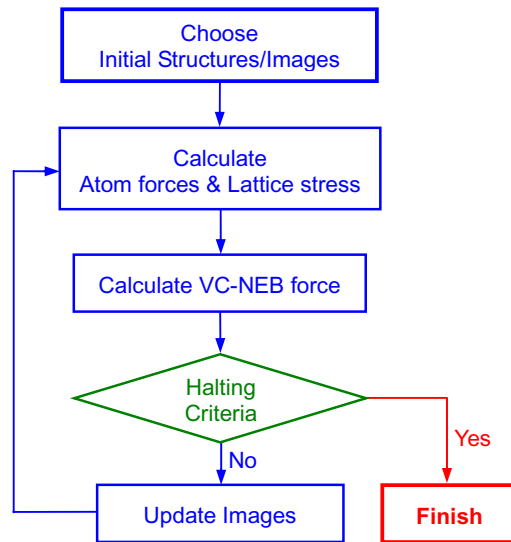


Fig. 3.5 Basic procedure of the VC-NEB technique. Figure taken from [143].

The basic procedure of the VC-NEB technique is as follows, as shown in Fig. 3.5:

(1) Firstly, we rearrange the lattice vectors and the sequence of atoms with a rotation-avoiding approach in the initial and final images.

3.3 Variable-Cell Nudged Elastic Band Method

(2) Initialize the first set of images, based on the linear interpolation between the initial and final images or with the user-provided specific configurations, for the intermediate images.

(3) Calculate the stress on the lattice and the forces on the atoms in the intermediate images from first principles.

(4) Calculate the VC-NEB forces based on the stress on the lattice and the forces on the atoms by determining the tangent vector τ with the vector $\mathbf{X} = (\epsilon_{1i}, \epsilon_{2i}, \epsilon_{3i}; r_1, \dots, r_N)$ ($i = 1, 2, 3$) for intermediate images.

(5) Calculate the transformation strain of the cell and displacement of atoms based on the VC-NEB forces by using the optimization algorithm, and generate a new set of images.

(6) Repeat steps (3)-(5) until the halting criteria are satisfied.

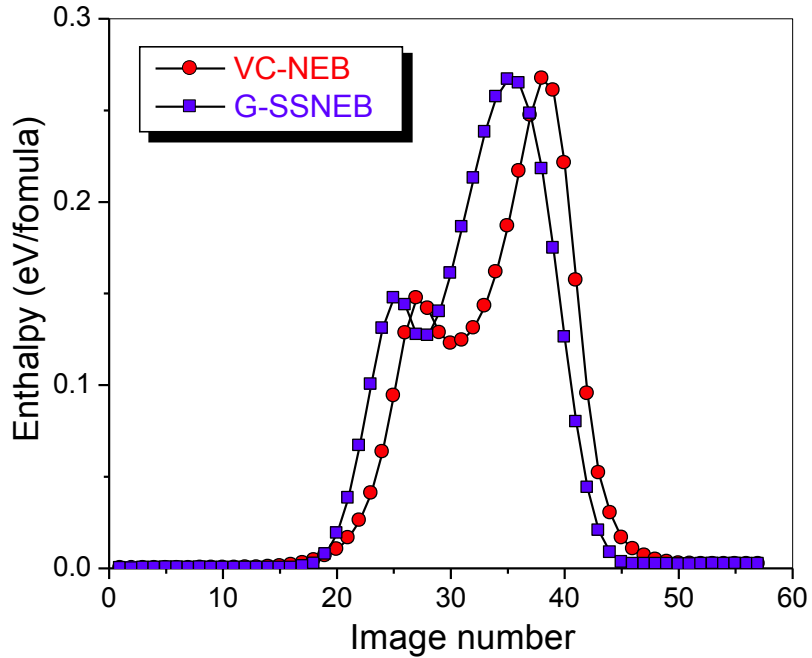


Fig. 3.6 Enthalpy barriers for the B4→B1 phase transition of AlN at transition pressure along *hexagonal* path, by using the VC-NEB and G-SSNEB methods. Figure taken from [143].

To confirm the universality of the VC-NEB method, we perform the calculations for the B4→B1 phase transitions in ZnO and AlN. The results validate that ZnO also favors the tetragonal path. The phase transition happens at a pressure $P_t = 9.54$ GPa with a barrier of ~ 0.13 eV/formula, which is very close to the value reported in Ref. [91]. For the B4→B1 phase transition along the tetragonal path, the tetragonal ZnO is a metastable structure. For the B4→B1 phase transition in AlN, the hexagonal path should be the unique transition

path, because when exploring the path starting with the tetragonal intermediate images, the optimized transition path converges into the hexagonal path quickly, never finding a MEP in the tetragonal intermediate images. For AlN, the *h*-MgO structure is a metastable intermediate structure, as shown in Fig. 3.6. Our results are in good agreement with the findings of Ref. [20]. In particular, the pathway obtained by the VC-NEB method is similar to the one given by using the G-SSNEB method, and with the same transition state structure.

The enthalpy barrier for the B4→B1 phase transition of AlN was calculated by using both the VC-NEB and G-SSNEB methods (VTST code, <http://theory.cm.utexas.edu/vtsttools/>) at $P_t = 14.0$ GPa in a four-atom cell. 57 images and the climbing image NEB were implemented in both the VC-NEB and G-SSNEB calculations. The phase transition barrier for the VC-NEB calculation is 0.265 eV/formula and the G-SSNEB method gives the same barrier. The corresponding enthalpy of *h*-MgO metastable structure from the VC-NEB method is 0.12 eV/formula, which is close to 0.13 eV/formula reported in Ref. [20], as shown in Fig 3.6.

3.3.3 Extra techniques in VC-NEB

The VC-NEB method is very efficient for finding the phase transition path, but we must also carefully prepare the initial path as for all other two-ended methods.

Rotation-avoiding technique The cell rotations happen near the initial and final structures during the VC-NEB calculation, while not happening in a traditional fixed-cell NEB method. As shown in Figs. 3.7, the enthalpy H has no change within the first 6 images (or the last 5 images), implying that the structure belongs still to the B4 (or B1) type, where they are only different in the directions. Therefore the first 5 images and the last 4 images could be avoided during calculation with rotation-avoiding technique to increase the number of “effective” images, and also avoid the twist of the pathway during the VC-NEB simulation.

This ineffective rotation situations are usually caused by

- 1) arbitrarily assigning the lattice vector \mathbf{h} ;
- 2) the flat basin shape of the initial and final structures on the PES when including the configuration space of lattices.

To remove these useless rotations, the rotation-avoiding technique needs to be considered in the VC-NEB method when generating the initial image set. The general 3×3 rotation matrix with Euler angles $R(\phi, \theta, \psi)$ and the lattice mirror operator $M(x, y, z)$ matrix are defined. Before performing a VC-NEB calculation, the global numerical search in space of Euler angles and mirror operator are used to find the minimal lattice cell transformation distance Δh

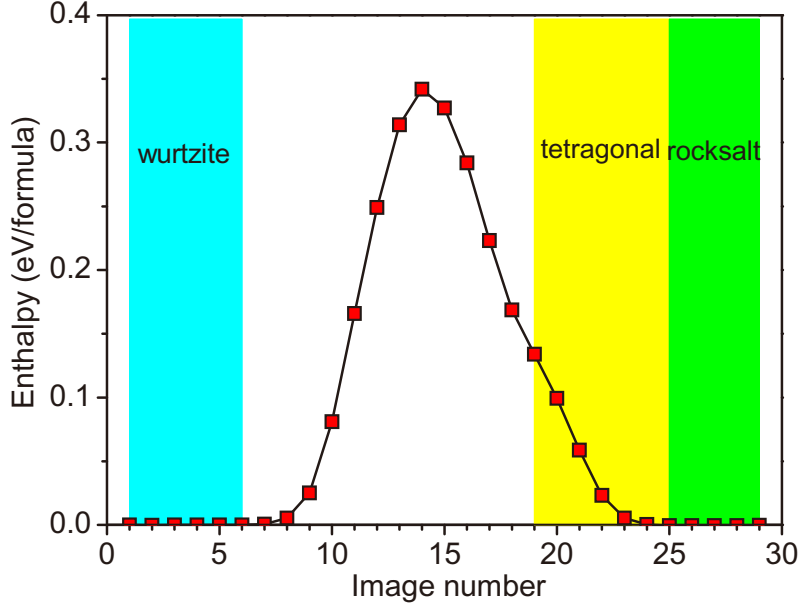


Fig. 3.7 Example for enthalpy barrier B4 (wurtzite) \rightarrow B1 (rocksalt) transformation along the “tetragonal” path. Without rotation-avoiding technique, the structure transformation process starts from image 6 and finishes at image 25, implying that there are only 18 “effective” intermediate images on the phase transition path. Figure taken from [143].

$$\Delta h = |h_{initial} - R(\phi, \theta, \psi)M(x, y, z)h_{final}|. \quad (3.12)$$

The rotation-avoiding lattice vector of the final image \tilde{h}_{final} is assigned as the endpoint image

$$\tilde{h}_{final} = R(\phi, \theta, \psi)M(x, y, z)h_{final}. \quad (3.13)$$

Variable-image-number technique Sometimes, the cell rotation situation still appears after applying the rotation-avoiding technique. Combining the fingerprint method [129], identical structures at the head or the tail of the pathway would be automatically removed, to prevent the cell rotations from appearing and would thus improve the efficiency and robustness of the VC-NEB method. Besides, different from the transition NEB method, without including cell relaxation procedure, the activation path length does not change too much when searching the pathway on the PES. In contrast, the activation path length between neighbor images, which can be represented as the Euclidean distance of configurations of images i and $i + 1$ ($\|\mathbf{X}_i - \mathbf{X}_{i+1}\|$), usually varies dramatically because of the significant change of the structure during the lattice relaxation. Deleting very close neighbor images and inserting new images when images escape too far from neighbor images can greatly balance the method and cover

more details of information on PES. On the other hand, this dynamical image adjusting method will also avoid the twist of the pathway caused by the structure relaxation. Usually, a criterion of the activation path length around $0.3\sim 1.5$ Å of neighbor images is enough to describe most details of the PES shape. In the VC-NEB method in USPEX, when the length between two neighbor images is larger than 1.5 times this criterion, a new image will be added between the two images using linear interpolation; when less than half of this value, the second image will be removed. The above two ways of dynamically adjusting the number of the images in VC-NEB are named as “variable-image-number” technique, which significantly increases the efficiency and improves the robustness of the method in pathway investigation of reconstructive phase transitions.

3.4 Transition path sampling approach

The VC-NEB method, like other modern variants of transition state theory, are very successful in simple and small systems with smooth topography of potential energy landscapes, as shown in Fig. 3.8(a). The success and efficiency of VC-NEB method relies on the choice of using the cell lattice and atomic coordinations to describe the PES, which would automatically reduce from high dimensional configuration parameters to the intrinsic reaction coordinates of the systems to represent the progress of the transformation process. This automatic reduction of reaction coordinates can be easily achieved on simple PES when searching the MEP in VC-NEB.

However, for numerous problems, especially in systems containing large number of atoms, PES topologies are rough, exhibiting a large number of local minima, maxima and saddle points. The reaction coordinates of these transition are then not clear and very difficult to anticipate.

For multidimensional free systems due to large number of atoms, PES also contains many saddle points as illustrated in Fig. 3.8(b). PES is dense in saddle points, which including generally an uncountable number of transition states. Therefore, accurate determination of these points is not possible between the two stable states, and the saddle points neither cease to be characteristic points of the free energy barrier, playing as the role of transition states. MD simulation is a powerful method in studying complicated and large scale system. However, for a complete phase transition trajectory starting in A and ending in B with a trivial MD simulation, it normally spends a long time staying at the initial state and occasionally jumping to the other. The investigation of reactive transition process from a few trivial MD trajectories are not enough to reveal the phase transition mechanism. Instead, to locate and

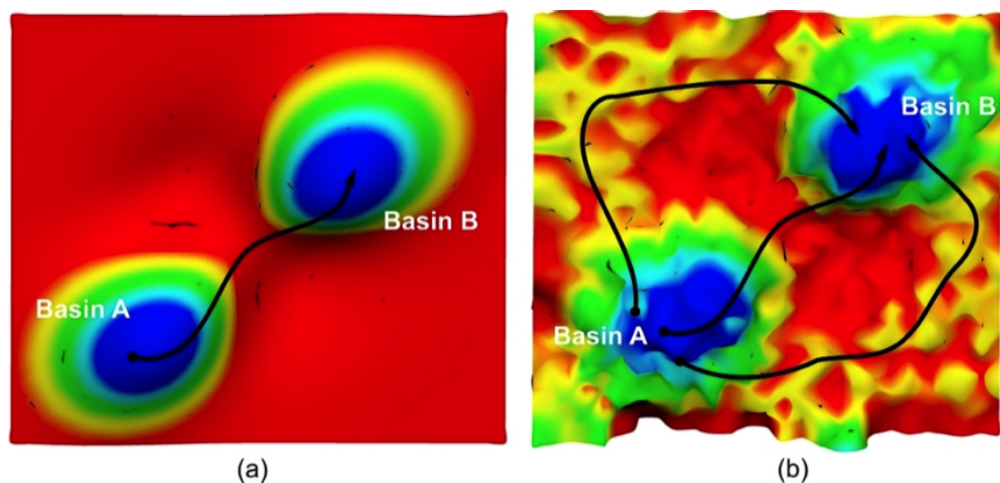


Fig. 3.8 Schematic illustration of two types of potential energy surface topologies as controlled by (a) energetic effects (2nd order phase transitions) and (b) entropic effects (1st order phase transitions). Color scale distinguishes between low energy (blue) and high energy (red) regions. Figure taken from [17]

sample an ensemble of transition states is alternate to accomplish this task within transition path sampling (TPS) approach [14, 15, 33, 35].

3.4.1 Transition path ensemble and sampling

The basic idea of TPS is a generalization of standard Monte Carlo procedures [27, 46] to investigate the trajectory space rather than individual states [142]. In standard procedures of TPS approach, Monte Carlo calculations perform a random walk in the path space of the transition trajectories connecting two stable states, within a certain finite time. A set of these reactive trajectories is called the “transition pathway ensemble”. The simulation process of TPS will help construct the ensemble within MD simulations, without requiring prior knowledge of the transition mechanism or reaction coordinates. To generate the appropriate path ensemble, efficient sampling methods are set up to avoid a very long time trial simulation of the truly reactive trajectories. All the relevant information can then be extracted from the ensemble, such as the kinetic information, reaction mechanism, the transition states, and the rate constants. Several important points of the TPS approaches are introduced below, more theoretical background and details are described in Ref. [14, 15, 33, 35].

Defining the Initial and Final Regions When applying TPS, the initial and final regions

are required to be correctly characterized mandatorily. An easy-to-use way is to apply a low dimensional order parameter to discriminate the regions of initial and final states, labeled as A and B regions below (as shown in Fig. 3.8). A successful order parameter must have the consideration of two criteria:

(1) be able to tolerate typical equilibrium fluctuations within basins of attraction. Otherwise, many important transition pathways might be missing in the transition path ensemble.

(2) region A and B should not extend off basins of corresponding basins of attraction (no overlap between A and B). Otherwise, the transition path sampling would wrongly collect $A \rightarrow A$ and $B \rightarrow B$ as reactive pathways.

Shooting Moves The crucial step of TPS is to generate new trajectories with an existing one. TPS applies powerful and efficient algorithms, by making small random changes in the atomic momenta, to perturb the given initial reactive pathway and create a new one. The new path will then be accepted or rejected in order to have the correct path probability satisfying given constraints. This simulation procedure is iterated and the transition path ensemble is gradually sampled. The algorithm is the so-called “shooting moves”, which is practically the most efficient method among many proposed schemes [112].

Consider the process of a phase transition described by coordinates x , momenta p and time t . A set of slices $(x(t), p(t))$ at discrete times t in $[0, T]$ are on the molecular dynamics trajectory, where T is the length of simulation time of the trajectory path. On the path, (r_0, p_0) is in A, and (r_T, p_T) is in B. A random point at time t on the current pathway is randomly picked, the momenta p are modified slightly into $p + \delta p$, where δp is a random perturbation consistent with system constraints, e.g. conservation of energy and linear and angular momentum. New MD simulations, both backward and forward in time, are then performed from this point with the perturbation p' . Integration of forward and backward paths results in a new trial pathway, as shown in Fig. 3.9. If the new path still successfully connects A to B, it is accepted, otherwise it is rejected and repeat the procedure starting from another point on the previous pathway. Thus, the shooting algorithm serves to achieve perturbation of an old path. The success or failure of the pathway generation procedure relies on the following points:

(1) the smaller the random changes of the atomic momenta, the larger the probability to succeed in finding a new reaction path;

(2) the closer point p is located to the ridge of the barrier tops, the larger the probability of succeeding in finding a new reaction path.

3.4 Transition path sampling approach

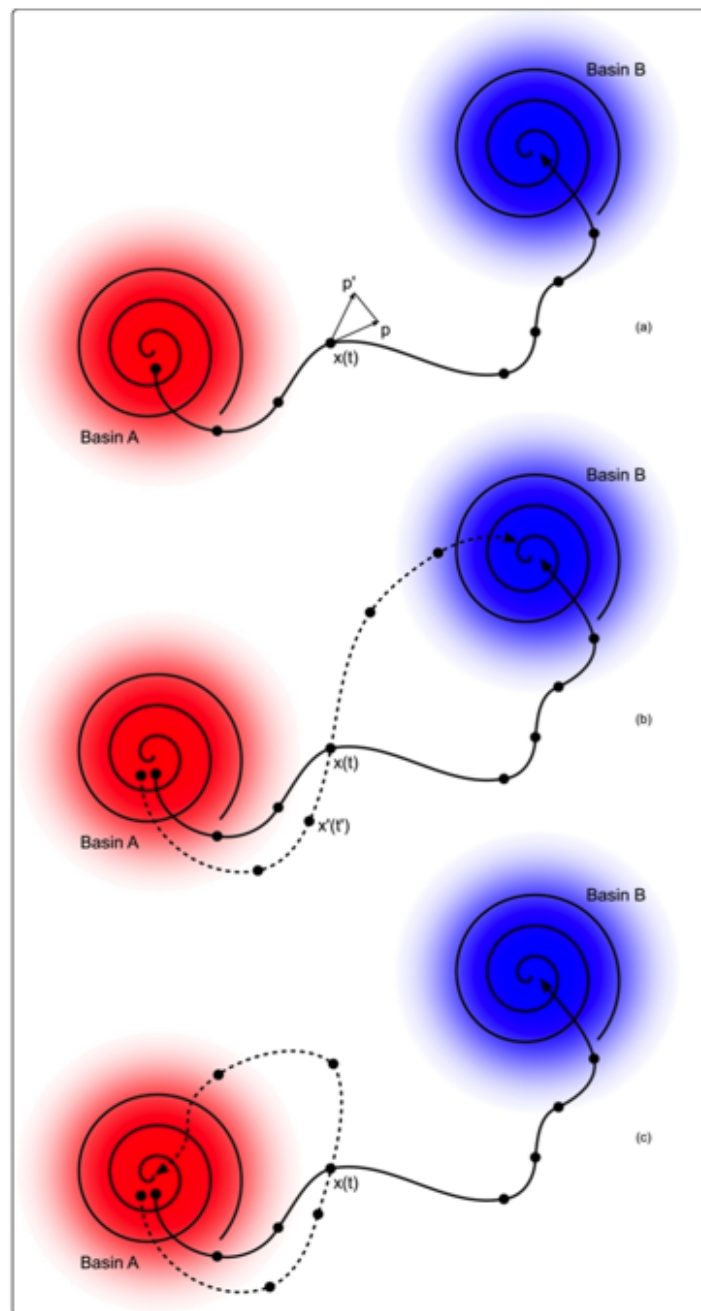


Fig. 3.9 Transition path sampling iterations at work: (a) a state (black spiral) is randomly chosen from an existing $A \rightarrow B$ trajectory and a new trajectory is shot off in direction of A. If successful, trajectory is retained, and another shooting point is chosen from it. (b)-(c) The shooting step is repeated in both directions, $A \rightarrow B$ and $B \rightarrow A$, shifting both limits of the shooting window until trajectory decorrelation is achieved. Figure taken from [17]

On the other hand, with very small random changes of the atomic momenta ($\delta p \rightarrow 0$), the new pathway will simply reproduce or closely follow the previous pathway. A number of new pathways are needed to generate in order to achieve pathways with no memory of the initial pathway. Thus, the magnitude of the momentum changes is usually a compromise, and we should therefore not strive for a 100% success rate in the pathway generation procedure. An acceptance probability in the range of 40 - 60% indicates an efficient sampling [34].

Rate Constant Computation The rate constant $k_{A,B}$ for the transition from A to B could be derived from the conditional probability (correlation function) [26, 32, 33, 35]:

$$P_{AB}(t) = \frac{\langle h_A(x_0)h_B(x_t) \rangle}{\langle h_A(x_0) \rangle} \quad (3.14)$$

where $h_A(x)$ and $h_B(x)$ are the characteristic population functions of regions A and B, respectively. These functions are used to decide whether a given state x is inside A (or B) or off basins:

$$h_{A,B}(x) = \begin{cases} 0 & x \in A, B \\ 1 & x \notin A, B \end{cases} \quad (3.15)$$

$h_{A,B}(x)$ is either 1 in state A(B) or 0 if not.

For short times, the conditional probability $P_{AB}(t)$ is linear with slope $k_{A,B}$,

$$P_{AB}(t) \approx k_{A,B}t \quad (3.16)$$

Hence once the conditional probability is known up to these times, the rate constant is also available.

3.4.2 Order parameter with fingerprint in USPEX

The TPS approach, like some applications of TST or Kramers theory [9, 42, 84], requires the specification of an order parameter (OP) or progress coordinate to successfully separate the initial and final states of the reaction. An advantage of path sampling over TST is that the OP needs not characterize a physical reaction coordinate, it must only distinguish the regime of the reactants and products. A poor choice of OP will fail to uniquely identify the discrepancy, even in a very simple model system.

On the other hand, the choice of a OP can be subtle and system-specific. People use different types of coordinates, collective variables (CVs), and OPs in different systems to describe the transition processes. For investigation of reconstructive transition, a general

3.5 Studying phase transition in USPEX

and efficient OP choice is important and necessary, which is yet usually not obvious. Such problems are expected to be even harder to detect in larger systems or those involving complex reactions in several stages. Borrowing the idea of identifying different structures with fingerprint, we can use an “indirect” way to describe the process of reaction to define an OP.

With the fingerprint method, we have a OP with two numerical values to separate the initial and final states – the cosine distance (similarity) referenced to the two phases. For example, for a system with 1000 atoms, the cosine similarity between any fcc and hcp phases, of any configuration in a MD simulation, is close to 0.96. The similarity of hcp and fcc structure for themselves of any configuration in MD calculation reaches 0.997. Such resolution between the fcc and hcp phase is large enough for distinguishing different regimes in a fcc \rightarrow hcp transformation. For smaller systems and more discrepant structures, the difference of fingerprints becomes larger, giving us the confidence that the fingerprint method is working well in describing reconstructive phase transition. Moreover, the fingerprint method as OP is a general way without any previous knowledge of the structures. The lower limit of the OP with the fingerprint can be indicated from the average cosine similarity of several structures, such as 6 structures, on the MD trajectory after a long time simulation.

3.5 Studying phase transition in USPEX

For the phase transition investigation in USPEX, there are mainly three methods at different levels to solve such problem. The EV-metadynamics method focuses on the phase transition sequence and neighbor phases searching, and we also could reach the phases tree information as a bonus. However, this technique has limitation in revealing the detailed progress of the structural phase transition process, like the transition pathway and mechanism of the atoms’ displacement and breaking and reforming of the bonds.

The VC-NEB method is a general tool for exploring the activation paths between the two endpoints of a phase transition process for small and simple systems. It is a simpler and time-saving method for studying phase transitions. In particular, for complex structural transitions, revealing the mechanism of the phase transition will become quite difficult. Even in simple structures, two or more MEPs may exist between the given initial and final images. The final MEP will likely converge to the path closest to the initial guess by using the minimization technique described above, despite the fact that the found path may not have the globally lowest barrier. The VC-NEB requires a good initial pathway for correct results. At the same time, we need to prevent the arbitrariness assigning the atomic fractional coordinates \mathbf{r}_v of the initial and final images. Otherwise, the calculation will be hard to

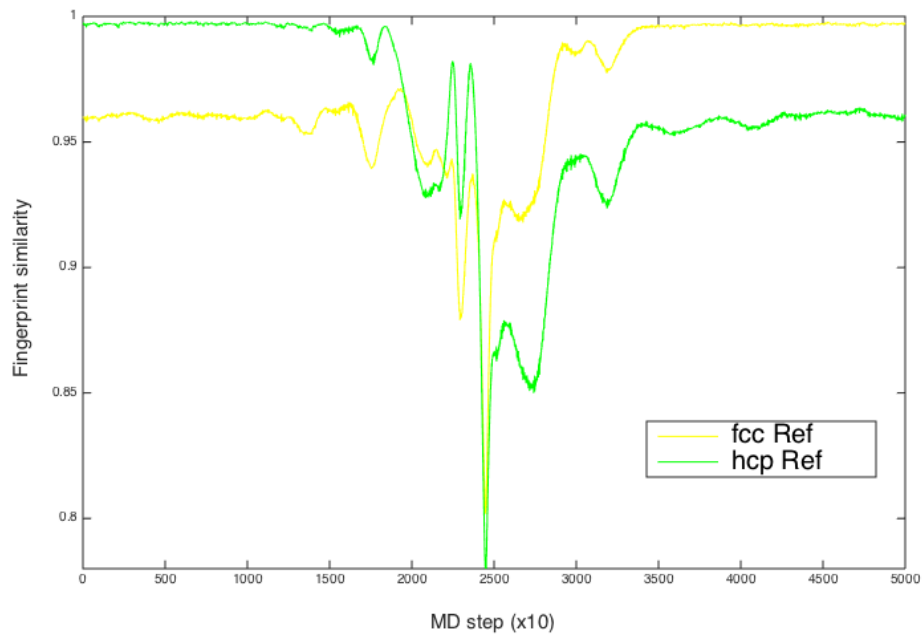


Fig. 3.10 Fingerprint method working to distinguish the hcp \rightarrow fcc phase transition in argon. The yellow and green lines indicate the cosine similarity of the configurations along the transformation referenced to fcc and hcp structures, respectively. MD time step is 1 fs.

3.5 Studying phase transition in USPEX

converge or several identical paths can be found in a calculation. The group/subgroup and topological approaches are helpful to analyze the correlation of the atoms in the two end stable states, but do not work for every situation. The evolutionary metadynamics method provides an direct and easier way in figure out the corresponding relationship of the atoms in initial and final phases. Because of soft-mutation operation, the atoms move along the modes with keeping the sequence fixed during the calculation. The distortion of the lattice provides a wider searching ability for finding same type phase transitions with different mechanisms in a different lattice shape.

The VC-NEB method will fail in case where landscape is as shown in Fig. 3.8(b). Besides, it is a zero-temperature method, stochastic sampling or molecular dynamics must be introduced into the VC-NEB method to overcome this limitation [62, 63]. As a complementary technique, the TPS approach can solve the complex landscape and temperature problem. For TPS, it is necessary to have a trial trajectory, connecting the initial and final states. Its weight can be very low but not-zero. There is no general recipe for modeling an initial path in complex systems. However, the rarity of the transition phenomenon makes the production of such a trajectory from an MD run unlikely to succeed. An artificial modeling of the initial trajectory represent a useful strategy. In this case, the use of interpolation schemes between the limiting stable states is possible. Doing so, one can have a good approximation for a transition state that can be used for shooting moves forward and backward in time in order to end in both A and B. Another option consists in the use of enhanced MD simulation. The use of very high-temperature or very high-pressure (compared to the experimental conditions) can enhance the phenomenon frequency. In this case, the system is systematically cooled, or the pressure is slowly released, in order to equilibrate the initial regime for TPS. But all these methods mentioned above for generating the first success trajectory are time-consuming and require experience. The VC-NEB method gives an excellent initial trajectory for the transition path sampling, avoiding the hard-to-use geometric/topologic approach that has been used before [18].

With evolutionary metadynamics, the VC-NEB and TPS approaches, USPEX provides us a very comprehensive view in studying phase transition mechanism.

Chapter 4

Structure Prediction of Materials Containing Hydrogen

4.1 Materials containing hydrogen at pressure

Hydrogen is the lightest, yet the most abundant element in the universe. Hydrogen combines with other elements to form numerous compounds. On earth, most hydrogen exists in molecular forms, forming covalent compounds with most non-metallic elements, e.g. water and all organic matters. As emphasized by Albert Szent-Györgyi, the Nobel Prize-winning biochemist, hydrogen is an essential element and fuel of life, rather than oxygen. Life's energy source depends on the heat and light from the Sun. Water is the most essential substance for life's existence. The organic compounds are the the building blocks of all various life. Without hydrogen, the earth is just another normal and dead planet in the universe.

Hydrogen is also a commercially important element. One important use of hydrogen is the ammonia synthesis, which is an important compound in many branches of science and technology. Hydrogenation – to treat with hydrogen – is the way in the manufacture to produce organic chemical compounds. Huge quantities of hydrogen are also used as clean fuels. For example, hydrogen fuel cells are being looked into as a way to provide power and research is being conducted on hydrogen as a possible major future fuel.

The behavior of hydrogen at high pressure attracts wide attention. Hydrogen has a very high energy content by weight, but it has a low energy content by volume . This makes hydrogen a challenge to store, particularly within the size and weight constraints of a vehicle. Methods of hydrogen storage for subsequent use include high pressures, cryogenics, and chemical compounds that reversibly release H₂ upon heating. Materials with framework structures can absorb additional H₂ molecules at pressure, forming a series

of novel H₂-containing stoichiometric compounds. Given their high amount of hydrogen, these compounds are potential energy storage materials. For example, CH₄-(H₂)₄ is a good potentially high hydrogen storage material [105, 162], with 33.4 wt% hydrogen content. Water and noble gases also have ability to store hydrogen by forming clathrate structures [97]. Some are good candidates for high-temperature superconductivity, such as (H₂S)₂-H₂ [39], GeH₄-(H₂)₂, SiH₄-(H₂)₂. Metallic hydrogen at pressure is one of the most important physical problems, and hydrogen-rich compounds are also extensively explored as alternatives because their metallization can occur at relatively lower pressures through chemical pre-compression and these compounds might display high-temperature superconductivity.

In this chapter, we mainly focus on hydrogen behavior in two very important systems, H-O and H-N under pressure. These investigations will help understand in more detail hydrogen storage and possible new compounds, even the possibility of existence of new formats of life in the universe. This chapter is mainly based on Ref. [144, 145], the citations for these two papers are not specifically stated below.

4.2 Novel hydrogen hydrate structures under pressure

Molecular compounds (cocrystals) of water ice (H₂O) and hydrogen (H₂) are known to form clathrate structures with the hydrogen molecules encapsulated as guests in the host sublattice formed by water molecules. Hydrogen hydrates, as environmentally clean and efficient hydrogen storage materials, have excited significant interest. Extensive literature exists from both experimental [40, 65, 66, 96, 101–103, 105, 106, 166, 181, 182] and theoretical [88, 197] sides. Aside from the H₂ molecules, many other small molecules are known to form clathrate structures as guest species under elevated pressure as well, including noble gases, nitrogen, oxygen, methane etc. (See Ref. [97] and references therein) Hydrogen hydrates are important as potentially major materials of icy satellites and comets, and potential hydrogen storage materials.

4.2.1 Motivation

Twenty years after the first report of the formation of two filled-ice hydrogen hydrates by Vos *et al.* [182], four hydrogen hydrate forms are known to exist at elevated pressures. Two of the hydrogen hydrates are clathrates, denoted as clathrate structure II (sII) [96, 106] and compound 0 (C₀) [40], the other two are filled ice hydrates, compound 1 (C₁) and compound 2 (C₂) [181, 182]. The sII clathrate hydrate was synthesized under pressures of 180 to 220 MPa at 300 K, and its structure was shown to contain 48 hydrogen molecules and 136

water molecules in the unit cell [106]. The C_0 clathrate was recently found to be stable near 0.5 GPa and to have the composition $2H_2O:H_2$ and trigonal structure [40]. The water molecules in the C_0 structure are arranged in a totally new way, different from the known ices or ice sublattices in hydrate structures. This structure has space group $P3_221$, but this could possibly go as low as $P3_2$, depending on how the hydrogens are arranged [40].

At higher pressures, clathrates give way to denser structures of the filled ice type. The C_1 and C_2 phases are formed at 0.36–0.9 GPa and ~ 2.4 GPa, respectively [166, 181, 182]. The C_1 hydrate has a water host framework based on ice-II and a 6:1 water to hydrogen ratio. C_2 has a 1:1 ratio of water to hydrogen and is composed of water molecules in the “cubic ice” (ice-Ic) framework and rotationally disordered hydrogen molecules [97]. Recent experiments [65, 101–103] indicate that the C_2 hydrate undergoes a structural transformation from cubic to tetragonal phase at around 10–20 GPa, with an increasing difference in the unit cell axes, and then transforms to another high-pressure phase near ~ 45 GPa. This high-pressure phase is maintained up to at least 80 GPa but its structure is not fully resolved. Given the difficulties in characterization of the chemical composition and crystal structure of these hydrates, and believing that new phases are likely to exist, we decided to perform a computational search to revisit the H_2O-H_2 system under pressure.

4.2.2 Hydrogen hydrate structures prediction

Using the evolutionary algorithm USPEX [126, 127, 201, 203], we explored possible stable phases in the H_2O-H_2 system. Predictions were done in the variable-composition mode at several pressures (0, 1, 2, 5, 10, 20, 50 and 100 GPa) and zero temperature. We have done two types of variable-composition structure predictions in searching for all stable phases in the H–O system: (1) In the H–O system, assembling the structures from atoms, and (2) In the H_2O-H_2 system, giving H_2O and H_2 molecules as structure building blocks. We have found that, even in the H–O system, the stable states at pressures of our interest (< 100 GPa) are actually made of well-defined H_2O and H_2 molecules. This allowed us to focus on molecular-type calculations, capable of efficiently dealing with large systems, without loss of rigor. Given molecular nature of all stable and nearly stable compounds in this system, we also searched for the packing of well-defined H_2O and H_2 molecules (rather than H and O atoms), by applying the specially designed constrained global optimization algorithm, considering structures containing up to 24 molecules (i.e. up to 72 atoms) per primitive unit cell.

Structure relaxations were done using density functional theory (DFT) within van der Waals (vdW) functional optB88-vdW [78] in the framework of the all-electron projector augmented wave (PAW) [13] method as implemented in the VASP [83] code. The plane

wave kinetic energy cutoff of 600 eV and Monkhorst-Pack k -point meshes with the reciprocal space resolution of $2\pi \times 0.05 \text{ \AA}$ were used. Having identified the most stable compositions and candidate structures, we relaxed them at pressures from 1 atm to 120 GPa with an even higher cutoff of 800 eV to refine their thermodynamic properties and stability fields. Structure relaxations proceeded until net forces on atoms were below 1 meV/\AA , which gave us enthalpies converged to better than 1 meV/atom .

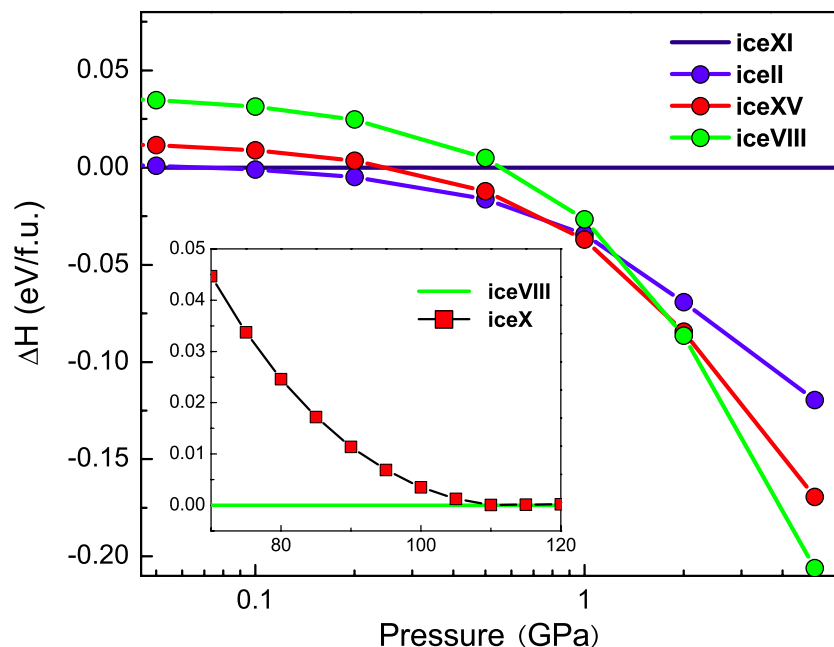


Fig. 4.1 Enthalpy relative to ice XI as a function of pressure with a van der Waals functional. The phase transition sequence at $T = 0 \text{ K}$ is ice XI \rightarrow II \rightarrow XV \rightarrow VIII \rightarrow X.

It is expected that the relative contribution of hydrogen bonding (H-bonding) and van der Waals (vdW) dispersion forces has a significant impact on the phase transition pressures and cohesive properties of the various crystalline ice phases [151]. This is also confirmed by our calculations, as shown in Fig. 4.1 for the phase transition pressures of ice phases from optB88-vdW, GGA [133] calculations and experiments. Thus, all calculations included the vdW functional to treat the vdW forces, unless stated otherwise.

4.2.3 Novel hydrogen hydrate materials

Remarkably, we have found two novel filled ice hydrogen hydrates, and all known hydrogen hydrates (except the sII structure, because of the very large number of molecules in its unit cell). Thus, at pressures in the range 0–2 GPa, the sII structure is input separately in order to

4.2 Novel hydrogen hydrate structures under pressure

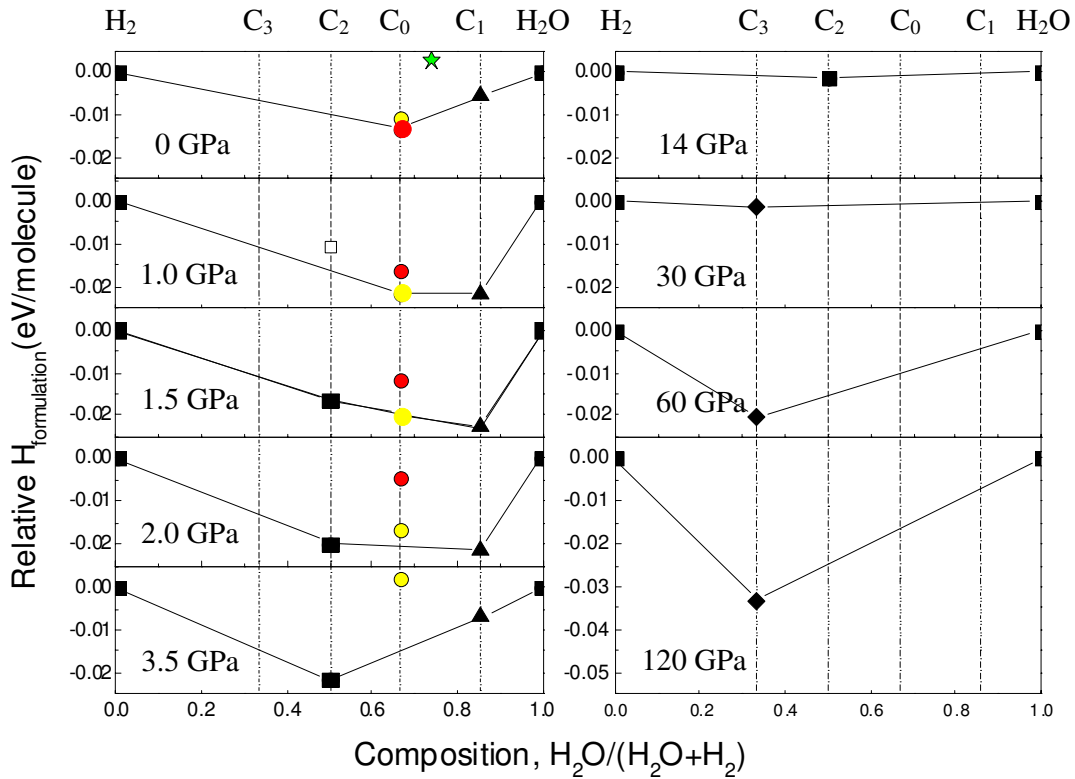


Fig. 4.2 Convex hull diagram for $\text{H}_2\text{O}-\text{H}_2$ system at selected pressures and zero temperature. This figure shows the enthalpy of formation (in eV/molecule) of molecular compounds from H_2O and H_2 . The red and yellow circles represent the C_0 and $Ih-\text{C}_0$ phases, respectively. The green star represents the sII structure.

calculate stability ranges of phases in the $\text{H}_2\text{O}-\text{H}_2$ system. Fig. 4.2 shows the convex hull diagram for the $\text{H}_2\text{O}-\text{H}_2$ system.

Our results are in generally very good agreement with experiments. At 0 GPa, the C_0 , C_1 and a novel hydrogen hydrate phase are found stable or nearly stable in the $\text{H}_2\text{O}-\text{H}_2$ system, while the sII phase is metastable (~ 0.013 eV/molecule less stable than the mixture of stable compounds C_0 and C_1). The structure of the novel hydrogen hydrate is based on the framework of hexagonal ice (ice-Ih), with two hydrogen molecules hosted inside channels running along the hexagonal axis (Fig. 4.3a). It has a 2:1 ratio of water to hydrogen, same as C_0 , and has space group Cc . We name it $Ih-\text{C}_0$ to distinguish from C_0 . The enthalpy of the $Ih-\text{C}_0$ phase is close to C_0 , and is slightly lower at pressures above ~ 0.4 GPa. At 1.5 GPa, in addition to the C_0 , $Ih-\text{C}_0$ and C_1 phases, the hydrate phase C_2 with an ice-Ic framework structure becomes stable.

At pressures above 2 GPa, the C_0 and Ih - C_0 phases are calculated to be above the convex hull, indicating that these phases become unstable against decomposition into C_1 and C_2 . Above 3.5 GPa, the C_1 phase will also become unstable, and the C_2 phase will remain the only stable hydrate. For hydrate C_2 , USPEX calculations uncovered at least four typical energetically favorable candidate structures at different pressures, $P4_12_12$, $I4_1/amd$, $Pna2_1$ and $I4_1md$ (see Fig. 4.4, which is similar to the results in Ref. [197]). The C_2 phase will lose stability at ~ 14 GPa, which is much lower than 40 GPa suggested in the previous study [65, 101]. We explain this by metastable persistence of C_2 up to the pressure of 40 GPa. Between 14–28 GPa, there are, unexpectedly, no thermodynamically stable hydrates.

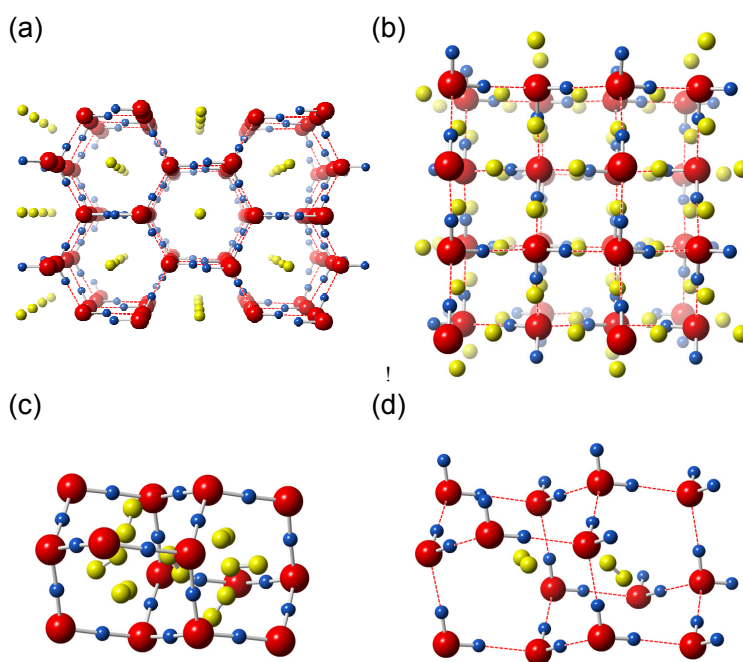


Fig. 4.3 (a) Hydrate Ih - C_0 structure at 0.5 GPa, (b) hydrate C_3 structure at 30 GPa, (c) cages formed by water molecules in hydrate C_3 at 100 GPa, the hydrogen molecules are located at the center of each chair-like H-O ring, (d) cages in “filled ice-Ic” hydrate C_2 , hydrogen molecules are in the center of the cage. Large red and small blue spheres are O and H atoms in water molecules, respectively; the yellow spheres represent the H_2 molecules in (a) and (b), and represent H atoms in (c) and (d). Red dashed lines represent hydrogen bonds.

Near 30 GPa, another novel H_2O – H_2 phase is found to be stable at zero temperature. It has a 1:2 water to hydrogen ratio, and net composition H_6O . This novel hydrogen hydrate, which we name C_3 , has the highest hydrogen concentration among all hydrogen hydrates. If it can be synthesized at low pressures, it would be an attractive hydrogen storage material, having 18 wt.% concentration of easily separable (non-water) hydrogen. The C_3 structure

4.2 Novel hydrogen hydrate structures under pressure

has space group $P4_1$ and is also based on the framework of ice-Ic (Fig. 4.3(b)), similar to low-pressure hydrate C_2 . The unit cell of C_3 contains four water molecules, the H_2 molecules are located at the center of chair-like H-O rings (formed by six oxygen and six hydrogen atoms) that form faces of the cage, as shown in Fig. 4.3(c). Differently, in the C_2 hydrate, the H_2 molecules are in the center of the water cages (Fig. 4.3(d)). According to our calculations, the C_3 phase will remain stable up to at least 120 GPa.

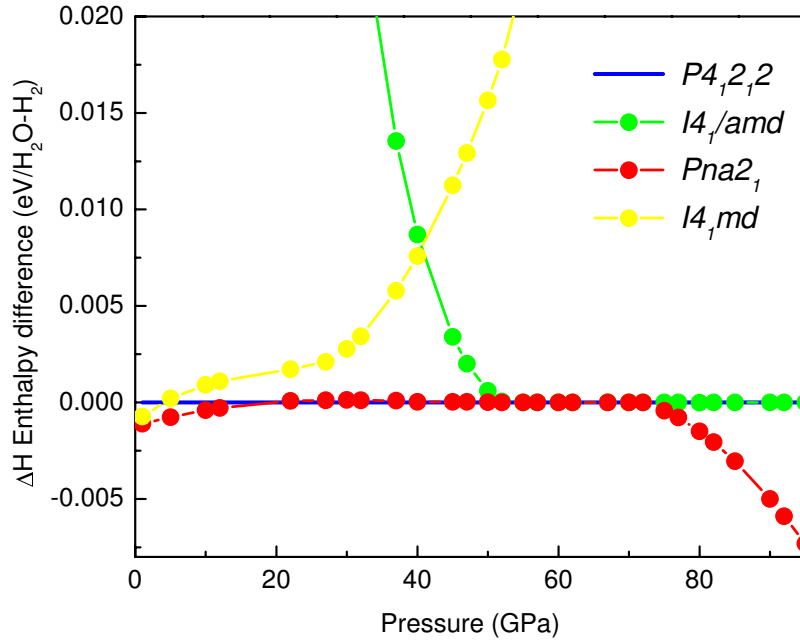


Fig. 4.4 Enthalpy of $I4_1/amd$, $Pna2_1$ and $I4_1md$ variants of the C_2 structure relative to the $P4_12_12$ structure as a function of pressure. Near 70 GPa, the $Pna2_1$ H_2O-H_2 transforms to the $Imma$ phase.

4.2.4 Phase diagram of hydrogen hydrate materials

Our theoretical calculations indicate that the H_2O-H_2 system contains several stable phases, including open-network clathrate structures (C_0) and dense filled ice phases ($Ih-C_0$, C_1 , C_2 and C_3). The C_0 phase is predicted to be stable at pressures below 1.5 GPa, which is close to the experimental result (below 0.8 GPa [40]). The C_1 phase is predicted to be stable at pressures below 3.5 GPa, also close to the experimentally determined transition pressure of 2.5 GPa [182]. The zero-point vibration energy (ZPE) significantly affects the relative stability of hydrogen-rich structures [141]. We have estimated the ZPE within the quasi-harmonic approximation [169] to refine the stability ranges of C_2 and C_3 phases above

10 GPa. When considering the ZPE, the stability field of the C_2 phase expands up to ~ 19 GPa, but this phase remains dynamically stable at pressure above its stability field, and thus can exist as a metastable material at pressures of at least 60 GPa.

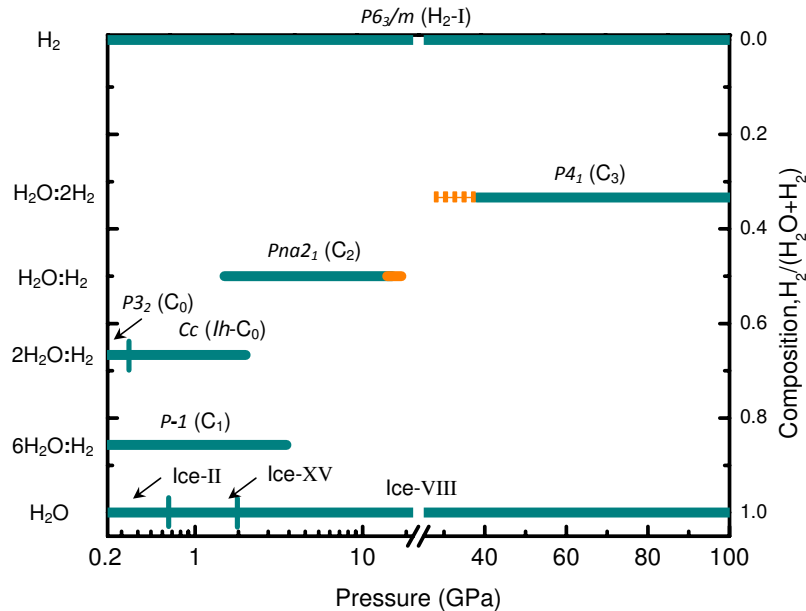


Fig. 4.5 Phase diagram of the H₂O–H₂ system. The stability ranges of C₂ and C₃ phases are calculated with and without ZPE effect. The solid orange line represents extra stability range added due to ZPE, the dashed orange line represents regions that become unstable after inclusion of the ZPE.

The C₃ phase starts to be energetically favorable above ~ 38 GPa when including ZPE, as shown in Fig. 4.5. Thus, the novel C₃ phase can be synthesized in hydrogen-rich conditions at pressures starting from 38 GPa. This theoretical value agrees well with the transition pressure 45–50 GPa to the hitherto mysterious phase of unknown composition observed in the experiments in Ref. [65, 101].

As shown in Fig. 4.6, the Raman shift calculations [87] reveal the the H₂ vibron Raman shift differences between the C₂ and C₃ phases in H₂-D₂O system. The Raman shift of C₃ phase, rather than an amorphous phase, agrees very well with the lower Raman frequencies of the vibron for the hydrogen molecules observed in Ref. [103]. The black rhombi in Fig. 4.6 indicate that some of the H₂-D₂O C₃ sample encountered decomposition when quenched to low pressure. The variation of lattice parameters of the ice host structure in hydrates with pressure, revealed by our theoretical calculations, also agrees well with the observation from the XRD results at high pressure [65]. At 55 GPa, our calculation gives lattice parameters of the C₃ phase $a=b=4.00$ Å and $c=5.67$ Å, corresponding to cubic ice sublattice with periodicity

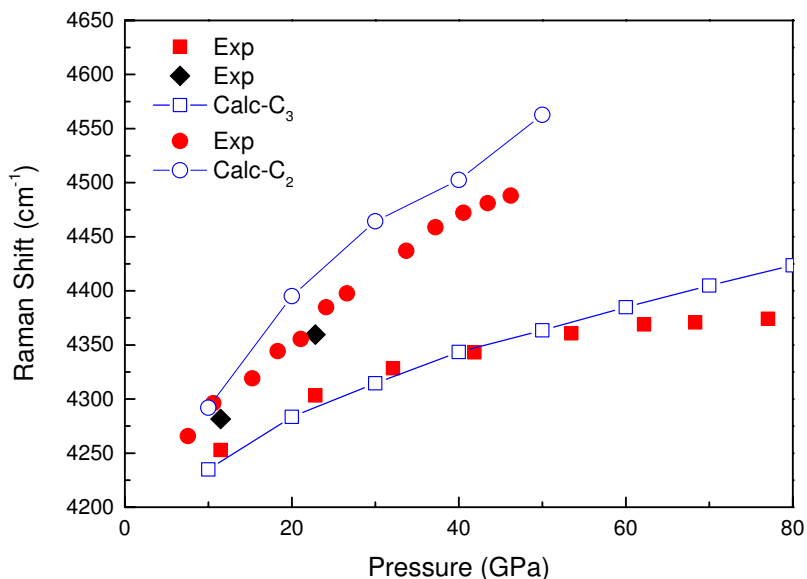


Fig. 4.6 Variations of the Raman shift of the vibron for the H₂ molecules with pressure from experimental data in [103] and our theoretical calculations. The red and black symbols are the experimental data for H₂ vibrons in the H₂-D₂O sample. The blue open circles and squares indicate the Raman shift calculation for C₂ and C₃ phases of H₂-D₂O system, respectively.

5.67 Å, where experiments gives ~ 5.5 Å [65]. At low pressure, the C₂ adopts a “cubic ice” host structure and then transforms to a “tetragonal” one around 20 GPa [65]. When forming the C₃ phase at increased pressure and in excess of H₂, the ice host structure transforms to the “cubic ice” again. The change from tetragonal to “cubic” structure occurs before H-bond symmetrization transition happens in “tetragonal” type C₂ around 55 GPa. Thus, such structural transformation is unrelated to symmetrization of the H-bonds, but comes from the emergence of the C₃ phase. For the hydrate C₃, the H-bond symmetrization is predicted to occur at ~ 120 GPa (see Fig. 4.7), which is close the theoretical H-bond symmetrization pressure in ice-VII [197].

4.2.5 Stability mechanism of hydrogen hydrate materials

The C₂ and C₃ hydrates have a similar ice host framework, but the different numbers of hydrogen molecules and their different locations and orientations bring huge differences in phase stability range. In the C₂ phase, hydrogen molecules stay in the centers of cages formed by water molecules in contrast to C₃ phase, where they are located at the faces of the cages.

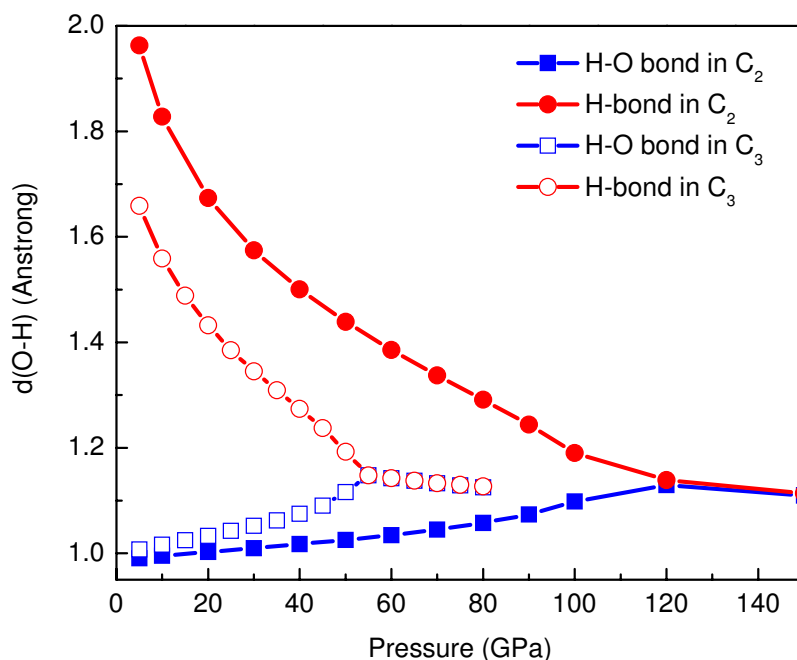


Fig. 4.7 The H-O distances in C₂ and C₃ phases. The H-bond symmetrization happens around 55 GPa in the C₂ phase and around 120 GPa in the C₃ phase.

To clarify the causes of stability of hydrogen hydrates, we used Bader analysis [4, 61], and focused on the C₂ and C₃ phases, as shown in Fig. 4.8. We found a very small charge transferred from H₂ to water molecules, so that the H₂ molecules are slightly positively charged, and H₂O molecules carry a slight negative charge. The magnitudes of these charges are $\sim 10^{-3} - 10^{-2}$ per molecule. This suggests that interactions between these molecules are almost purely steric, mainly related to packing density and shapes of the molecules. Comparing Bader volumes of the H₂O and H₂ molecules in the hydrates and in pure H₂O and H₂, we see that water molecules occupy slightly larger volume in the hydrates, whereas hydrogen molecules occupy much less space in C₃ hydrate than in pure H₂ – this leads to net densification, stabilizing this phase in a wide pressure range. For the C₂ hydrate, the H₂ molecules have lower volume than in pure H₂ only at pressures below ~ 10 GPa, which explains its instability at higher pressures.

Having considered the PV-term in the enthalpy ($H = E + PV$), to get additional insight, we turned to the internal energy E and its changes when the H₂ and H₂O molecules are placed from the hydrate into pure H₂ and H₂O phases, while keeping molecular volumes fixed to their values in the hydrate (Fig. 4.8). This energy characterizes the net balance between the vdW attraction and steric repulsion between the molecules: this net effect is

4.2 Novel hydrogen hydrate structures under pressure

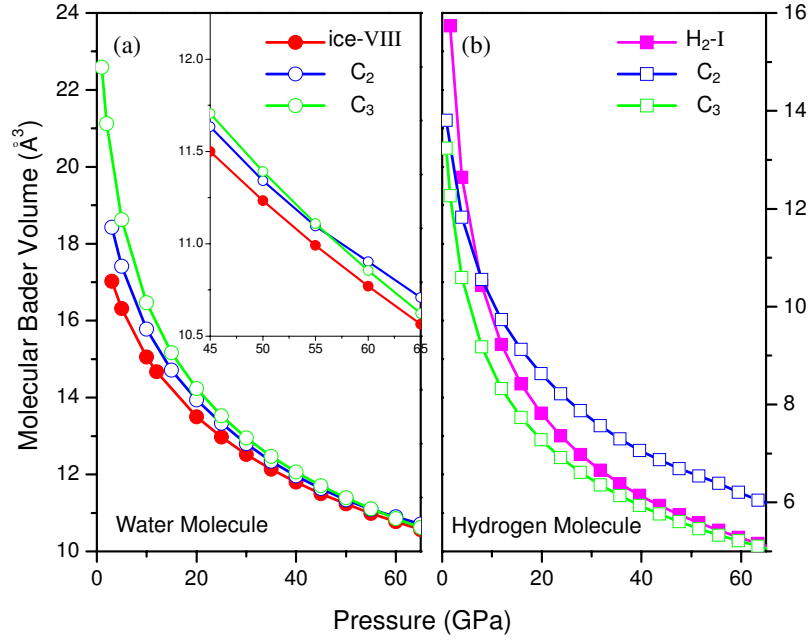


Fig. 4.8 Bader volumes of the water and hydrogen molecules in ice-VIII, H₂-I [141], C₂ and C₃ phases as a function of pressure.

very small in the C₃ phase (slightly destabilizing below ~ 30 GPa and slightly stabilizing above ~ 30 GPa). The remarkably wide stability field of the C₃ phase is therefore mostly due to its high density and only to a small extent to more favorable intermolecular interactions. A much more interesting picture is observed for the C₂ phase (Fig. 4.9a): we find its slight energetic stabilization below ~ 15 GPa, and an increasingly large destabilization at higher pressures. This explains why C₂ is unstable at high pressures, and furthermore, it is clear that the increasing energetic instability of the C₂ phase is responsible for the displacive phase transition, metastably occurring on overcompression and transforming the cubic H₂O host sublattice into tetragonal, to enable better packing of the molecules.

Our theoretical calculations also found that a C₃-type phase is stable in the H₂O–He system at 8-75 GPa (without including zero-point energy), and this phase is denser than the mixture of H₂O and He. On the other hand, no such phase was found in the H₂O–Ne system, and indeed the C₃ phase is not packing-efficient in this system (see the Fig. 4.10). He and Ne are equally chemically inert, their almost only differences are size and (here insignificant) mass. Stability of He-C₃ and instability of Ne-C₃ hydrates reinforce our conclusion made for the H₂O–H₂ system, that stability of this novel phase comes not from specific bonding interactions between the molecules, and not even due to their shapes, but mostly due to their very efficient packing.

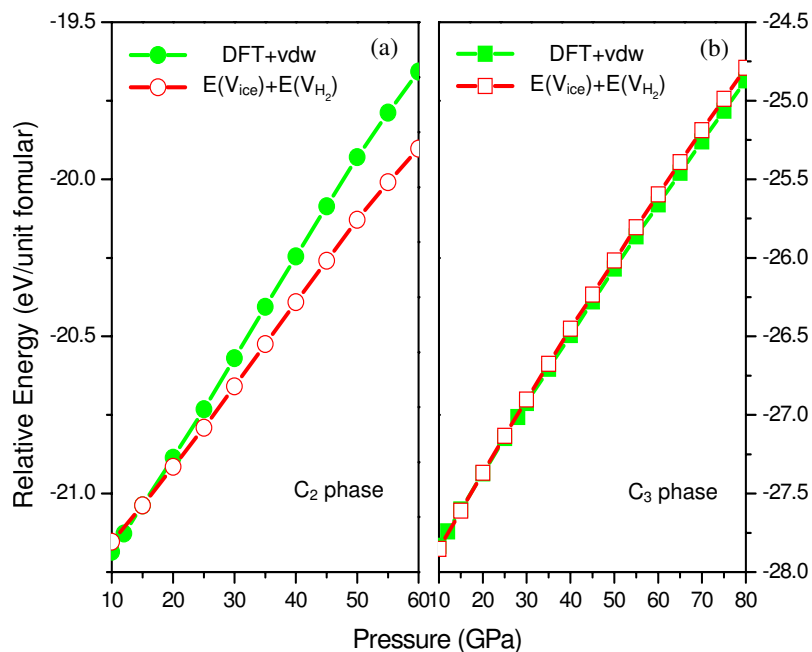


Fig. 4.9 Internal energy of the C₂ and C₃ phases relative to the isochoric mixture of H₂O and H₂. Green lines represent the energy of the hydrate phases; red lines – the energy of the isochoric mixture of ice-VIII and H₂-I phases.

In summary, using the evolutionary algorithm USPEX, we explored the H₂O–H₂ system at pressures of up to 100 GPa. Stoichiometries and stability fields of H₂O–H₂ hydrate phases have been studied. A series of pressure-induced transformations found by theory closely coincides with experimental data, but also new insight was obtained. A novel *Ih*–C₀ structure is predicted to have a very close enthalpy to the recently discovered C₀ structure. At pressures above 38 GPa, novel hydrogen hydrate C₃, based on cubic ice Ic, is predicted to be stable. With stoichiometry H₂O:2H₂, this is the hydrogen-richest hydrate known to date. With gravimetric density of easily removable hydrogen (18 wt.%), this is a promising hydrogen storage material that can find practical applications if its synthesis pressure can be decreased.

4.3 Novel hydronitrogens materials under pressure

Hydrogen is the most abundant, and nitrogen - seventh most abundant element in the universe. Giant planets Uranus and Neptune are predominantly made of H, O, C and N. While the behavior of the H-O [145, 181, 182] and C-O [49] systems under pressure has been investigated in some detail, the N-H system remains largely unexplored. Ammonia

4.3 Novel hydronitrogens materials under pressure

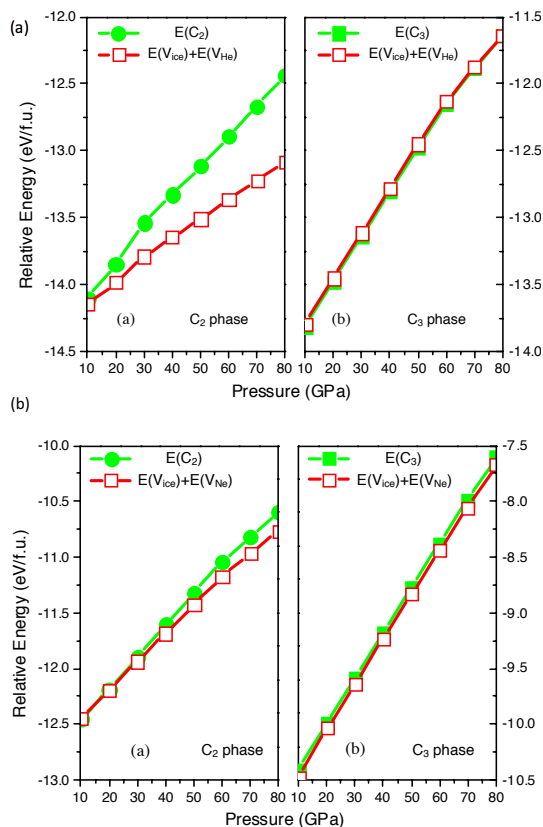


Fig. 4.10 Internal energy of the C_2 and C_3 phases of (a) H_2O -He and (b) H_2O -Ne, respectively.

(NH_3), as an important compound in many branches of science and technology, is the only stable hydronitrogen at ambient conditions, and exists in a wide range of temperatures and pressures. Recent studies [54, 123, 139] revealed that ammonia undergoes a series of phases transitions, including ionic disproportionation and return to non-ionic phase at megabar pressures. Ammonia is considered as a major component of the interiors of giant planets such as Uranus and Neptune under extreme pressure (up to 600 GPa) and temperature (2,000~7,000 K) [25, 58, 70, 148, 152]. Nitrogen hydrides, including ammonia (NH_3), hydrazine (N_2H_4), hydrazoic acid (HN_3), etc., are compounds of great fundamental and applied importance. Their high-pressure behavior is important because of their abundance in giant planets and because of the hopes of discovering high-energy-density materials.

What has not been properly explored is the full phase stability in the N-H system [30, 93–95, 131, 195], including the possibility of decomposition of ammonia; it may well be that, instead of ammonia, very different molecules with different stoichiometries are actually present in planetary interiors.

All nitrogen hydrides, except ammonia, are metastable at ambient pressure. Due to the substantial energy difference between single and triple nitrogen-nitrogen bonds, nitrogen-rich hydronitrogens are potentially superior high-energy-density materials. However, large-scale synthesis of these materials is still problematic. Having a complete phase diagram for the N-H system is necessary for developing synthetic strategies, but such a phase diagram has not been determined. As a result, there is a fundamental interest in investigating the high-pressure behavior and corresponding structural and stability properties of N-H system in both planetary and condensed-matter physics.

Extensive theoretical [69, 201, 205] and experimental [199] studies revealed exotic compounds appearing under compression, and exhibiting unique structures and properties different from usual compounds - see previous investigations of NaCl [199], MgO [205], BH [69] and H-O [145] systems. One might wonder if new hydronitrogen compounds should emerge under pressure. Considering the dramatically changed nature of nitrogen [100, 168, 188] and the autoionization [139] found in NH_3 , this appears plausible.

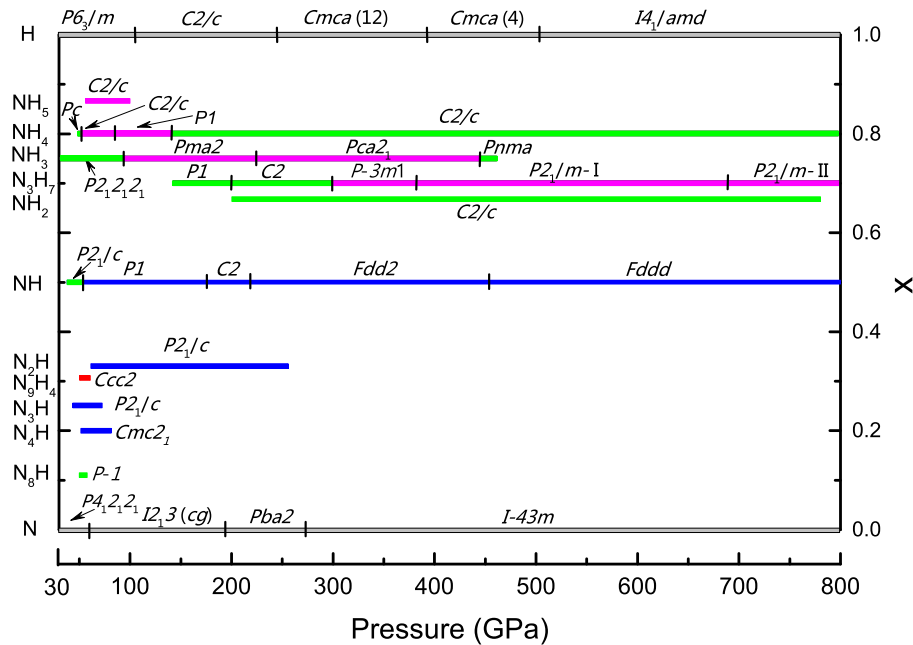


Fig. 4.11 Phase diagram for N-H system from 30-800 GPa. For the hydronitrogen structures, the blue color indicate infinite nitrogen chain structures. Green and pink indicates molecule and molecular ionic structures, respectively. The red color indicates the 2D-plane N_9H_4 phase.

4.3.1 Calculation details

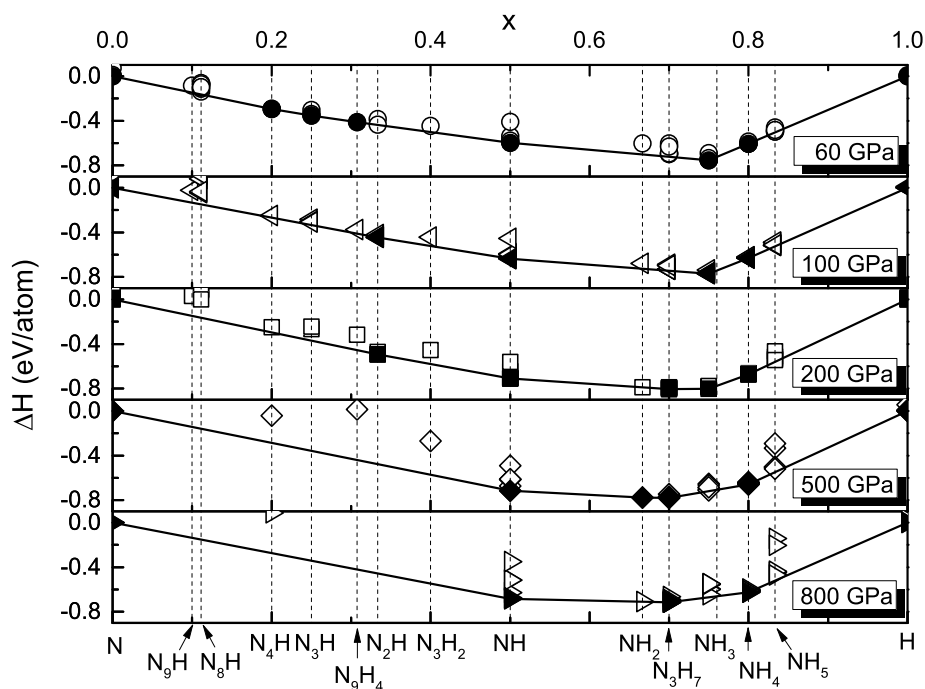


Fig. 4.12 Convex hull for nitrogen hydride system at 60, 100, 200, 500, 800 GPa. The solid and hollow symbols indicate stable and metastable phases, respectively.

Using the evolutionary algorithm USPEX [125–127, 201, 203], we carried out structure and stoichiometry predictions to find all stable compounds (and their stability field) in the N-H system (See Methods). Our calculations confirm that ammonia is the only stable hydronitrogen from ambient pressure to 36 GPa. Above 36 GPa, remarkably, a whole series of previously unknown compounds become stable. These compounds exhibit unusual compositions, peculiar structures and unique properties.

Crystal structure prediction was performed using the variable-composition evolutionary algorithm USPEX [125–127, 201, 203]. A number of studies illustrate the power of the USPEX method [69, 199, 205]. Calculations for the N-H system were performed at various pressures in the wide range of 0-800 GPa.

Given the dramatically changed behavior of nitrogen under pressure and a wide pressure range of our investigation, we performed a number of different types of predictions with USPEX. We ran variable-composition predictions for N-H, N-NH and NH-H systems with up to 32 atoms per unit cell. Given the molecular nature of all stable and nearly stable

compounds in hydrogen-rich hydronitrogens, we also did structure prediction for the packing of well-defined NH_3 and H_2 molecules (rather than N and H atoms), by applying the specially designed constrained global optimization algorithm, considering structures with up to 24 molecules (i.e. up to 96 atoms) per primitive unit cell. These calculations were run together in a global coevolutionary search with exchanging good (stable and some metastable) structures between different runs. This coevolutionary method is very efficient and has been implemented on top of the USPEX code.

When performing prediction for metastable nitrogen structures containing zigzag N-chains, we applied the antiseeds technique [98], which was adopted to search for all low-enthalpy structures based on zigzag N-chains.

After the thermodynamically stable hydronitrogen compounds were found, we can classify them into three types. (i) Infinite-chain polymeric hydronitrogens, including N_4H , N_3H , N_2H and NH , with polymeric chains featuring all-nitrogen backbones. (ii) Two-dimensional (2D) metallic N_9H_4 phase consisting of 2D nitrogen planes and NH_4^+ cations; note that 2D-nitrogen planes have not been reported in any other nitrogenous compounds before. (iii) Molecular compounds including N_8H , NH_2 , N_3H_7 , NH_4 , NH_5 , and of course NH_3 . Here, molecular (or molecular ions) compounds are bonded by hydrogen bonds. The phase diagram of the stable compounds is shown in Fig. 4.11 and detailed convex hulls at 60, 100, 200, 500, and 800 GPa are presented in Fig. 4.12.

4.3.2 Polymeric hydronitrogens

We found that nitrogen-rich hydronitrogens (N_xH , $x \geq 1$) are more prone to adopt polymeric structures with N-backbones, except N_9H_4 and N_8H . The N_8H phase is very close to the convex hull at 40~60 GPa, $\sim 0.003\text{eV/atom}$ above the convex hull line at 55 GPa. Below 69 GPa, the ground state of N_8H adopts the $\text{P}\bar{1}\text{-N}_8\text{H}$ molecular structure with four pentazole (N_5H) and six N_2 molecules in the unit cell (as shown in Fig 4.13a). Above 69 GPa, N_8H adopts a long zigzag chain structure with symmetric hydrogen bonds between the two nitrogen backbones, (as shown in Fig 4.13b). Our calculations indicate that N_9H also adopts long zigzag chain structure at 40~80 GPa, where only 1/3 of the zigzag chains have hydrogen attached on the nitrogen backbone chain (as shown in Fig 4.13c).

The N_4H , N_3H and N_2H compounds are predicted to be stable at 51-80 GPa, 42-75 GPa and 60-260 GPa, respectively. The ground state of N_4H has a $\text{Cmc}2_1$ structure, containing four zigzag nitrogen chains (N-chains) in the unit cell, with pairs of nearest N-chains linked by hydrogen bonds, see Fig. 4.14a. Here, we use

4.3 Novel hydronitrogens materials under pressure

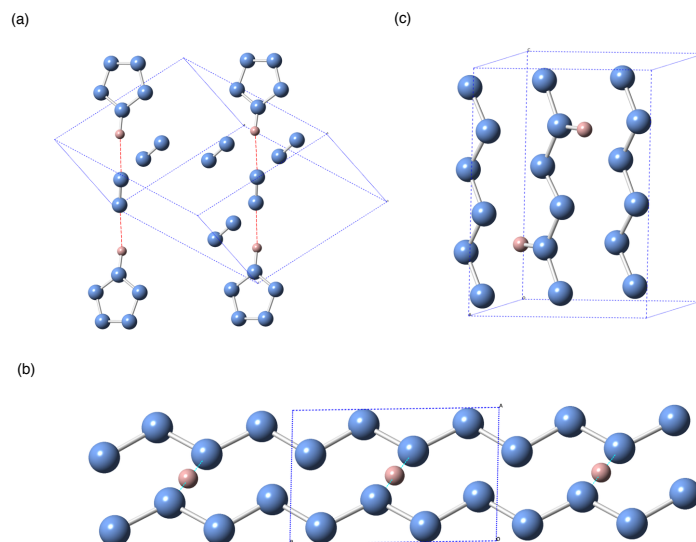
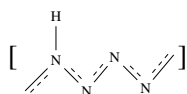
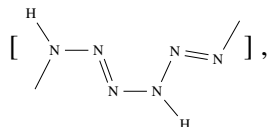


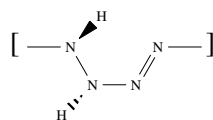
Fig. 4.13 Structures for N_8H and N_9H , (a) $P\bar{1}$ - N_8H molecular structure with four pentazole (N_5H) and six nitrogen molecules. (b) $P\bar{1}$ - N_8H structure with zigzags-shaped nitrogen chain structure. (c) $Cc2m$ - N_9H type with zigzags-shaped nitrogen chains. The red dot lines indicate symmetric hydrogen bonds.



to represent the monomeric unit in the polymeric chain of N_4H . The delocalized nitrogen-nitrogen bonds run along the zigzag chain, and have the same length of 1.28 Å at 60 GPa. Instead of a zigzag chain, the most stable N_3H structure has space group $P2_1/c$ and is composed of distorted arm-chair monomers



see Fig. 4.14b. These chains are connected with each other through H-bonds to form a layered structure. The $P2_1/c$ phase of N_2H becomes thermodynamically stable at ~ 60 GPa, and its structure consists of two



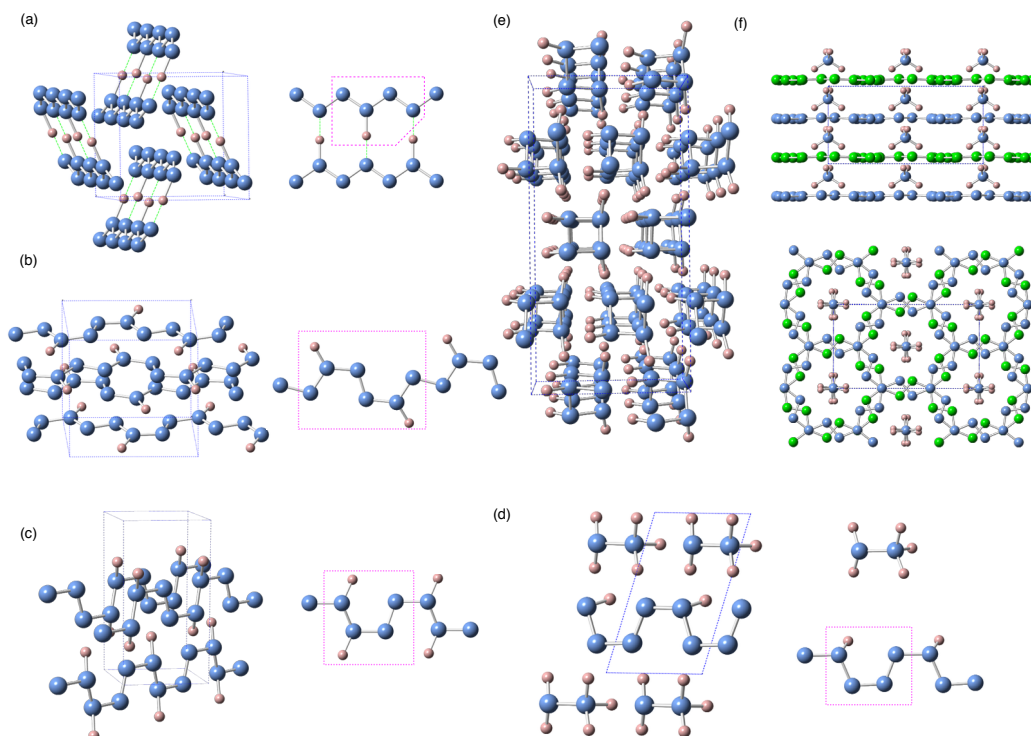
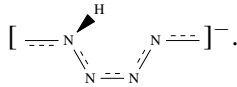


Fig. 4.14 The proposed structures for N_4H , N_3H , and N_2H and NH , N_9H_4 . The small pink spheres indicate hydrogen atoms and the blue large spheres are nitrogen atoms. The structures in the pink box are the corresponding monomeric units. (a) $Cmc2_1$ - N_4H structure. The structure is composed of one dimensional zigzag-shaped N-chains. Every two chains are engaged though asymmetric hydrogen bone, and crosswise packed. (b) Layered $P2_1/c$ - N_3H structure containing distorted arm-chair-shaped chain. (c) $P2_1/c$ - N_2H structure composed of parallel one dimensional arm-chair-shaped N_2H chains. (d) $P1$ - NH structure. Its structure consists of $N_2H_5^+$ ion and negatively charged arm-chair-shaped chain layers. It will transform to $C2$ phase at 180 GPa, due to the symmetrization of the hydrogen bonds between $N_2H_5^+$ ions and between chains. (e) The $Fdd2$ - NH structure consists of square-spiral-like chains. (f) Top view and side view of $Ccc2$ - N_9H_4 . The small pink spheres indicate hydrogen atoms and the blue and green large spheres are nitrogen atoms at different layers.

4.3 Novel hydronitrogens materials under pressure

monomers in the unit cell, see Fig. 4.14c. At 200 GPa, the lengths of single N-N bonds in this polymer are 1.27 and 1.28 Å, and the double N=N bond is slightly shorter as 1.24 Å. The small difference hints at a possible bond resonance along the chain. The doubly-bonded nitrogen atoms form weak asymmetric hydrogen bonds with nearby chains. Before the symmetrization of hydrogen bonds occurring at ~ 280 GPa, $P2_1/c$ -N₂H undergoes a spontaneous decomposition at ~ 260 GPa. All these polymeric structures are metallic as a result of bond resonance and electronic delocalization along the nitrogen backbone.

With the equal ratio of nitrogen and hydrogen, the NH compound is predicted to be stable in a huge pressure range, from 36 GPa and at least up to 800 GPa. The $P2_1/c$ structure is more stable than the one predicted in the work of Hu & Zhang [68]. This phase consists of two tetrazene N₄H₄ molecules in the unit cell, which are short hydrogen-capped nitrogen zigzag chain molecules. At 55 GPa, $P2_1/c$ -NH undergoes a phase transition to an ionic structure of $P1$ symmetry. As shown in Fig. 4.14d, the ionic structure is composed of N₂H₅⁺ cations arranged in hydrogen bonded layers, alternating with layers of infinite chains



The unit cell structure contains 6 NH formula units: N₂H₅⁺ group and N₄H⁻ from the polymeric chain. At ~ 180 GPa, all hydrogen bonds become symmetric and space group is raised to $C2$. Both the $P1$ and $C2$ structures are only nominally ionic, because they are metallic and metals have very efficient screening of ionic interactions by the electron gas. Above ~ 220 GPa, the ionic NH phases become less stable than an $Fdd2$ structure made of tetragonal spiral chains, as shown in Fig. 4.14e. Similar square chains have been reported in group VI elements under pressure, e.g. sulfur-II phase [31] and the $I4_1/amd$ phase of oxygen at pressure around 2 TPa [167]. The $Fdd2$ -NH is predicted to be a wide-gap semiconductor (4.8 eV at 400 GPa). In contrast to the strongly localized electrons found in the $I4_1/amd$ -oxygen structure with isolated chains, $Fdd2$ -NH has asymmetric hydrogen bonds between the square chains. $Fdd2$ transforms to an $Fddd$ structure upon hydrogen bond symmetrization at 460 GPa. For both these orthorhombic phases symmetry breaking leads to two non-equivalent N-N bond lengths in the chain - e.g. 1.25 and 1.34 Å in $Fddd$ -NH at 460 GPa. The different lengths of the N-N bonds come from the distortion of the square spirals, caused by their packing and hydrogen bond pattern. The $Fddd$ -NH remains stable up to at least 800 GPa.

Our theoretical calculations indicate that the N-H system exhibits rich chemistry under pressure. The infinite long-chain polymeric structures are widely found in nitrogen-rich hydronitrogen compounds, and are thermodynamically stable above 42 GPa. They could potentially serve as good high-energy-density and fuel materials due to the substantial

energy difference between the single/double and triple nitrogen-nitrogen bonds. The nitrogen backbone follows different patterns as a different hydrogen ratio in compounds. With the “antiseeds” technique mentioned above, we found that metastable nitrogen phases containing zigzag N-chains have competitive enthalpies (~ 0.03 eV/atom higher at 60 GPa) to the molecular states and the singly bonded cg-N [43] structure at 40-70 GPa, and they are more energetically favorable than arm-chair-shaped and other N-chains. A low hydrogen content stabilizes these chains and does not change much of the packing pattern of the chains and the electronic properties of the resonant N-N bonds. The ground states of metastable N_9H and high pressure N_8H phases contain infinite zigzag N-backbones. With higher hydrogen content, the zigzag N-backbone become unstable in N_3H , N_2H and NH phases.

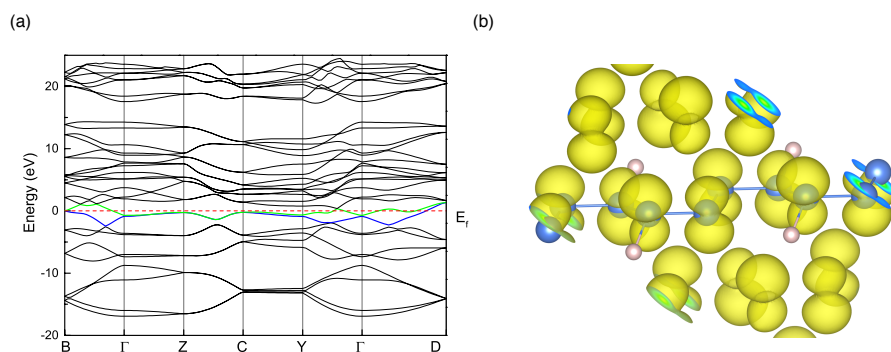


Fig. 4.15 (a) The band structure of $P2_1/c$ N_2H phase at 120 GPa. (b) Electron density corresponding to the vicinity of the Fermi level for the $P2_1/c$ N_2H chain structure. The nitrogen atoms have sp^2 hybridization, and are responsible for the π^* orbitals along the arm-chair nitrogen chain, which makes N_2H act as a metallic polymer.

Isoelectronic to oxygen, (NH) units generally serve as analogs of group VI elements in these polymeric chain structures. Besides the square-spiral chain in high pressure phases found in NH , the monoclinic N_2H phase can be considered as an analogue material of sulfur nitride $(SN)_n$ [6] or $(ON)_n$ [74, 75] polymers. The proposed nitrogen oxides $(ONNO)_n$ chain oligomer also has comparatively strong N=N bonds. The monoclinic N_2H phase is a metallic polymer as the Fermi level is crossed by anti-bonding π^* bands (See Fig 4.15), which is similar to the first known metallic polymer $(SN)_n$ [117] as a superconductor with $T_c = 0.26$ K [53]. All our 1D long-chain hydronitrogen compounds containing delocalized nitrogen bonds are metallic. Our calculations reveal that N_4H (at 55 GPa) and N_2H (at 60 GPa) are superconductors with $T_c = 2.6$ and 7.8 K (with the value of $\mu^* = 0.13$), respectively.

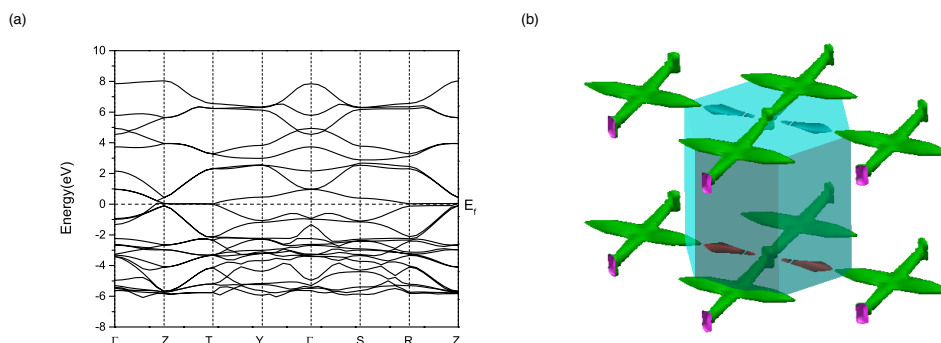


Fig. 4.16 (a) Band structures of N_9H_4 and (b) Fermi surface of N_9H_4 at 60 GPa.

4.3.3 Two dimensional N_9H_4 phases

Distinct the polymeric chain structures, we also discovered an exotic stable nitrogen-rich compound N_9H_4 . Its structure has $Ccc2$ symmetry, and is composed of negatively-charged 2D nitrogen planes and NH_4^+ cations. $Ccc2$ - N_9H_4 was predicted to be thermodynamically stable in a narrow pressure range 50-60 GPa. As shown in Fig. 4.14f, the 2D nitrogen plane is a loose structure due to the hexagonal star-shaped holes decorated by 18 additional nitrogen atoms. Parallel stacking of the nitrogen planes creates infinite channels in the perpendicular direction, and NH_4^+ cations are located along these channels. As a result of the delocalized electrons in the plane, the compound N_9H_4 is metallic with a flat band crossing the Fermi level. In contrast to N_3H and N_2H , N_9H_4 phase is not a superconductor.

4.3.4 Molecular hydronitrogens

N_8H is found to be stable around 50 GPa, and adopts a very unusual molecular structure with four pentazole (N_5H) and six nitrogen (N_2) molecules in the unit cell, as shown in Fig 4.13(a).

Hydrogen-rich hydronitrogens, instead of polymeric structures, have hydrogen-bonded molecular structures. The NH_4 phases, containing a higher hydrogen ratio than NH_3 , are found to be thermodynamically stable above ~ 50 GPa, and stable at least up to 800 GPa. At pressures above 50 GPa, NH_4 first adopts a host-guest structure of Pc symmetry with the structural formula $(NH_3)_2 \cdot H_2$, as shown in Fig 4.17a,b. Other host-guest structures, adopting $P2_1$, $C2/c$ and $I4/m$ symmetries, have very close enthalpies to this structure below 80 GPa,

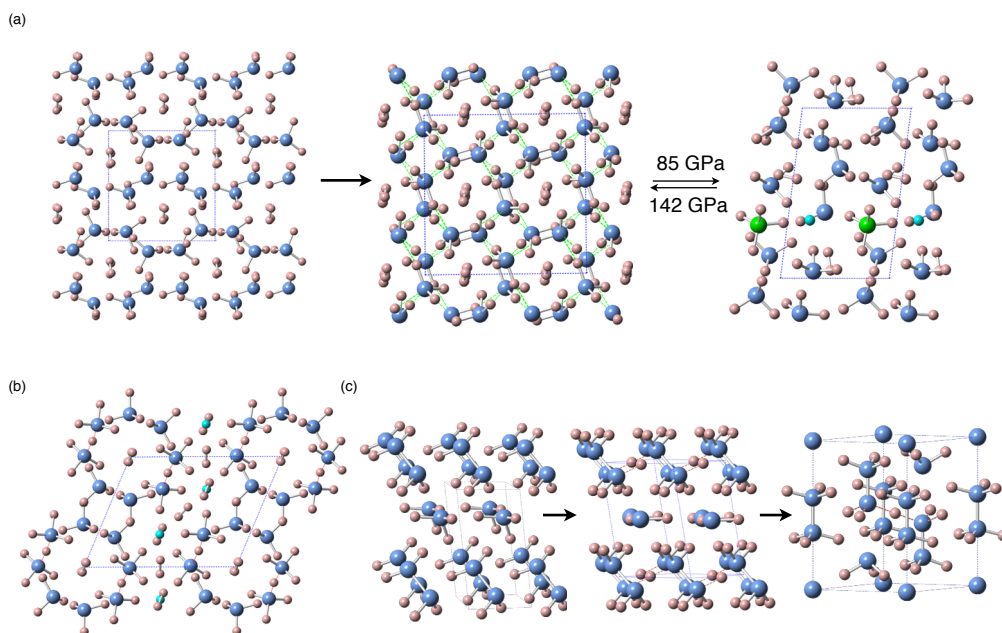


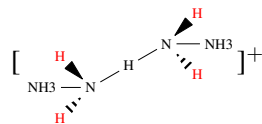
Fig. 4.17 The proposed structures for NH_4 , NH_5 and N_3H_7 . The small pink spheres indicate hydrogen atoms and the blue large spheres are nitrogen atoms. The nitrogen atom in NH_4^+ cation and the H^- anion are noted with green and aqua spheres, respectively. (a) Phase transition sequence from host-guest $Pc \rightarrow$ host-guest $C2/c \leftrightarrow$ Partially ionic $P1$ NH_4 phases. In host-guest structure of $C2/c$ - NH_4 , the hydrogen molecules are captured in the channels formed by NH_3 molecules. In the partially ionic $P1$ - NH_4 structure, the NH_4^+ cation is close to the H^- anion. (b) The ionic $C2/c$ NH_5 phase, with symmetric hydrogen bonds in $[\text{H}_3\text{N} \cdots \text{H} \cdots \text{NH}_3]^+$ units and H^- anions. (c) Phase transition sequence molecular $P1 \rightarrow$ ionic $C2 \rightarrow$ ionic $P-3m1$ N_3H_7 .

4.3 Novel hydronitrogens materials under pressure

(See Fig 4.18). At 52 GPa, $C2/c$ - NH_4 becomes the most stable among host-guest structures. In all host-guest structures, H_2 molecules are captured in hydrogen-bonded frameworks formed by NH_3 molecules. In the pressure range 85-142 GPa, the ionic $P1$ - NH_4 phase is more stable than host-guest molecular structures. In the unit cell of this low-symmetry ionic phase, every eighth ammonia molecule reacts with an H_2 molecule to form the NH_4^+ cation and H^- anion. The distance of H^- anion and the nearest hydrogen of the NH_4^+ cation is 1.13 Å at 100 GPa. Above 142 GPa, the ionic phase undergoes a reentrant transition to the same $C2/c$ host-guest structure again, thus returning to structures consisting of neutral NH_3 and H_2 molecules. Hydrogen-bond symmetrization was not observed in any stable NH_4 phases up to 800 GPa.

With the 1:1 ratio of H_2 and NH_3 , several NH_5 phases are also found to be thermodynamically stable or nearly stable around 55-100 GPa. The ionic $C2/c$ phase (See Fig 4.17b) has the lowest enthalpy at pressures below 162 GPa. In the unit cell of $C2/c$ - NH_5 , there are two $[\text{H}_3\text{N}\cdots\text{H}\cdots\text{NH}_3]^+$ units and two H^- anions. At pressure above ~ 162 GPa, $C2/c$ - NH_5 phase transforms into metastable ionic $P2$ and $Ama2$ structures, then adopts a $P2_1/c$ structure containing alternating layers of NH_3 and H_2 molecules above ~ 363 GPa, (See Fig 4.19).

At about 140 GPa, a previously unreported remarkable compound with the composition N_3H_7 is also found to be thermodynamically stable. For N_3H_7 , we have predicted several thermodynamically stable phases with the structural sequence $P1 \rightarrow C2 \rightarrow P-3m1 \rightarrow P2_1/m\text{-I} \rightarrow P2_1/m\text{-II}$ upon increasing pressure (See Fig 4.17c for the first three structures). At 140-200 GPa, $P1$ - N_3H_7 adopts a stable molecular structure, consisting of one ammonia (NH_3) and one hydrazine (N_2H_4) molecule in the unit cell. At 200 GPa, $P1$ undergoes a spontaneous molecular-to-ionic transition, resulting in a layered $C2$ structure. In this process, ammonia and hydrazine molecules react to form the NH_2^- (amide) anions and N_2H_5^+ (hydrazinium) cations, respectively. The N_2H_5^+ ions are in a parallel arrangement and connected by symmetric H-bonds. At 300-380 GPa, complicated ionic N_3H_7 structure of $P-3m1$ symmetry becomes stable. As shown in Fig 4.17c, the third structure has the trigonal unit cell, containing two neutral ammonia molecules, one N^{3-} anion, one $[\text{N}_2\text{H}_6]^{2+}$ cation and one



unit (net formula N_4H_9^+ , the red H symbols indicate that such hydrogen atoms are symmetrically hydrogen-bonded and shared with neighbor N_4H_9^+ units). This is the only structure with bare nitrogen anions observed among the newly proposed nitrogen hydrides. The nitride anion N^{3-} is surrounded by 12 hydrogen atoms from NH_3 molecules and N_4H_9^+

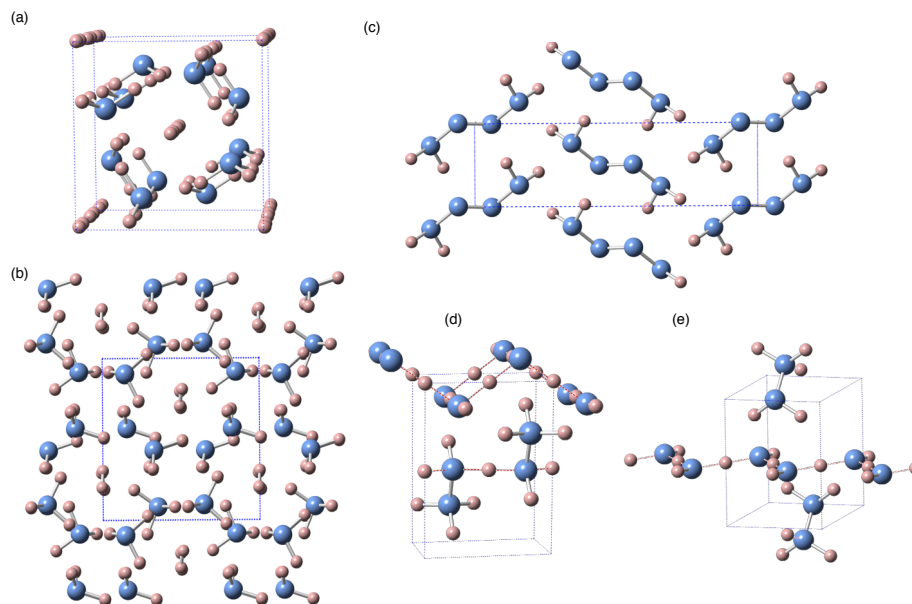


Fig. 4.18 (a) Host-guest $I4/m$ NH_4 structure at 60 GPa, the hydrogen molecules fill channels in the frameworks formed by NH_3 molecules. (b) Host-guest $P2_1$ type NH_4 structure at 60 GPa. There is only small difference in the orientation directions of the NH_3 molecules between $P2_1$ and Pc type NH_4 . (c) Short-chain molecular $P2_1/c$ -NH structure at 36 GPa. (d) The $P2_1/m$ - N_3H_7 structure (shown at 400 GPa) is stable in the range 380-680 GPa and consists of buckled N_2H_5^+ and NH_2^- layers. (e) Another $P2_1/m$ N_3H_7 structure (shown at 500 GPa, we call it $P2_1/m$ -II), calculated to be stable above 680 GPa, is also an ionic phase consisting of NH_5^+ and NH_2^- ions. In contrasting to the $P2_1/m$ structure, the NH_2^- layers arrange as zigzag chains plain between the NH_5^+ layers. All the symmetric hydrogen bonds are shown by the red dashed lines.

4.3 Novel hydronitrogens materials under pressure

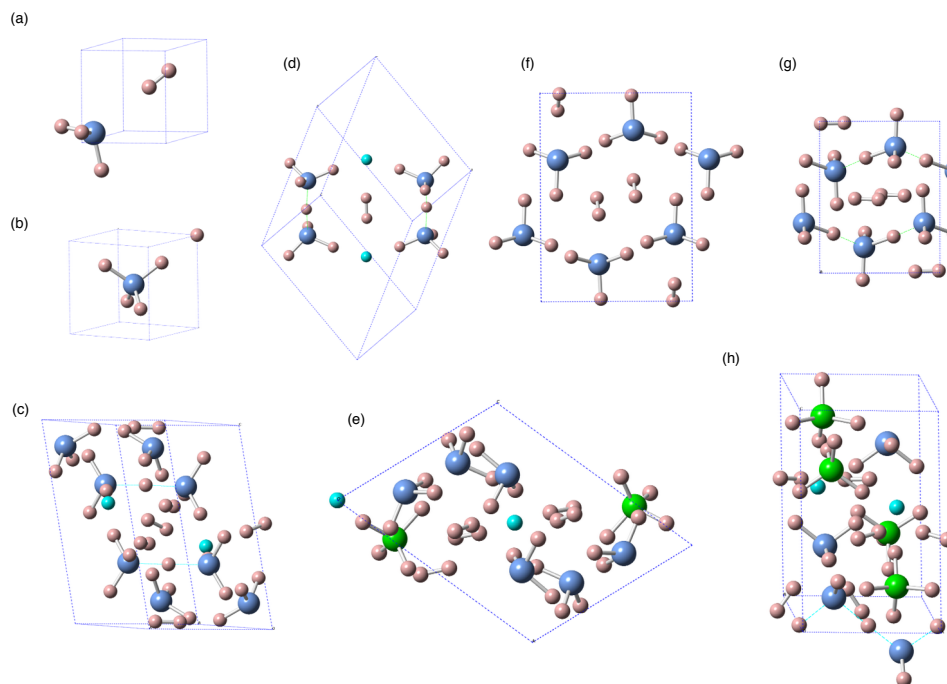


Fig. 4.19 Various structures for NH_5 . (a) Molecular $R3m$ structure at 5 GPa. (b) Ionic $P-43m$ structure at 5 GPa. (c) Ionic $C2/c$ structure at 150 GPa. (d) The view of $[\text{H}_3\text{N}\cdots\text{H}\cdots\text{NH}_3]^+$ subunit in ionic $C2/c$ structure at 100 GPa. (e) Ionic $P2$ structure at 200 GPa. (f) Molecular $P2_1/c$ structure at 40 GPa, where hydrogen molecules locates at the empty channels formed by NH_3 . (g) Another molecular $P2_1/c$ structure at 500 GPa. (h) Ionic $Ama2$ structure at 300 GPa. The small pink spheres indicate hydrogen atoms and the blue large spheres are nitrogen atoms. The nitrogen atom in the NH_4 cation and the H^- anion are noted with green and aqua spheres, respectively.

cation, with distances of 1.32 and 1.38 Å at 380 GPa. Then, at pressure above 380 GPa, the trigonal N_3H_7 phase will give way to another two $P2_1/m$ type ionic structures, consisting of NH_2^- anions and $N_2H_5^+$ cations again. They have different packing patterns from the ionic $C2$ structure (named $P2_1/m$ -I and $P2_1/m$ -II N_3H_7 by stability sequence upon increasing pressure, respectively.)

With pressure increasing, our calculation confirmed that NH_3 , above 36 GPa, undergoes phase transformations from hydrogen-bonded molecular $P2_12_12_1$ structure to layered ionic $Pma2$ and $Pca2_1$ phases, and then returns to $Pnma$ structures consisting of neutral NH_3 molecules at very high pressure [123, 139]. However, NH_3 , the only thermodynamically stable hydronitrogen compound at ambient conditions, is surprisingly predicted to decompose into N_3H_7 and NH_4 at ~ 460 GPa at zero temperature. For NH_2 , the dense molecular hydrazine phase was also predicted to be stable and have a $C2/c$ symmetry at ~ 200 -780 GPa, which is consistent with Zhang's work [196]. The $C2/c$ structure of NH_2 consists of hydrazine molecules, forming both symmetric and asymmetric hydrogen bonds with each other.

Multiple stable stoichiometries also exist in hydrogen-rich hydronitrogens at pressure. These hydronitrogens form molecular crystals at low pressure, and then tend to undergo auto-ionization under moderate compression, except NH_2 (See Table. 1). The structures of these compounds show various characteristics and are quite different from each other. N_3H_7 , NH_4 (and NH_5) can be considered as binary $NH_3 + N_2H_4$ and $NH_3 + xH_2$ compounds, respectively. Therefore, in general, high-pressure hydrogen-rich hydronitrogens tend to contain molecules and molecular ions.

It is predicted that hydrogen-rich hydronitrogens remain stable to extremely high pressures, NH_3 and NH_2 become unstable and decompose (into NH_4 and N_3H_7 , or into NH and N_3H_7) only at 480 and 780 GPa, respectively; and NH_4 and N_3H_7 are thermodynamically stable at least up to 800 GPa. In contrast, methane (CH_4) was predicted to dissociate into ethane (C_2H_6), butane (C_4H_{10}), and finally, diamond plus hydrogen at 287 GPa [49].

NH_4 and NH_5 undergo a molecular \Rightarrow ionic \Rightarrow molecular phase sequence under pressure, which is very similar to NH_3 [139]. The auto-ionization process also occurs in N_3H_7 , which remains in the ionic phase at least up to 800 GPa. In contrast, C-H compounds have non-polar non-ionic structures, and the high energy cost of proton transfer in H_2O [139, 189] prevents auto-ionization until extremely high pressure (~ 1.4 TPa) [189]. Our calculation revealed that the energy cost of proton transfer from H_2 to NH_3 molecule and from NH_3 to N_2H_4 molecule is ~ 0.7 eV and ~ 1.0 eV, respectively, while it costs ~ 0.9 eV [90] to form NH_2^- and NH_4^+ ions in NH_3 . Therefore, $NH_3 + xH_2$ compounds would undergo auto-ionization at a lower pressure (NH_4 at ~ 85 GPa and NH_5 at ~ 42 GPa) than pure NH_3 (at ~ 90 GPa).

4.3 Novel hydronitrogens materials under pressure

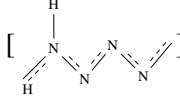
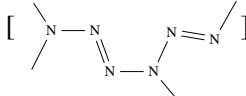
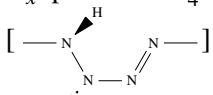
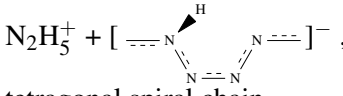
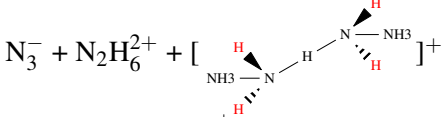
Due to high cost of proton transfer, auto-ionization phenomenon was not observed in any stable $\text{H}_2\text{O}-\text{H}_2$ compounds [145]. Calculations show that auto-ionization happens at ~ 200 GPa in N_3H_7 , higher in NH_3 (90 GPa) [139], due to the higher proton transfer energy cost, and survives up to at least 800 GPa. The pV term in the free energy plays an important role in deterring the phase transition sequence at high pressure. Under pressure, stable N_3H_7 and NH_3-xH_2 host-guest phases are more packing efficient than the volume of $\text{NH}_3 + \text{N}_2\text{H}_4$ and $\text{NH}_3 + \text{H}_2$, respectively. The auto-ionization transition in N_3H_7 leads to denser structures and enhances stability of N_3H_7 under compression.

4.3.5 Discussion

We have extensively explored the nature of hydronitrogen compounds up to ultrahigh pressures. It turns out that unusual compounds, such as $\text{N}_8\text{H N}_4\text{H}$, N_3H , N_9H_4 , N_2H , NH , NH_2 , N_3H_7 , NH_4 and NH_5 are stable under pressure. These compounds possess intriguing crystal structures and remarkably novel, exotic properties. Three main features can be concluded, 1) the (NH) unit behaves similarly to its isoelectronic analogs, oxygen (also the sulfur) atoms, 2) molecular hydronitrogens are mainly composed of H_2 , NH_3 , N_2H_4 molecules and corresponding ions, 3) auto-ionization is common in N-H molecular phases due to the low energy cost of the proton transfer among the H_2 , NH_3 , N_2H_4 molecules.

Our investigation opens ways for designing synthesis strategies of novel high-energy-density polymeric hydronitrogens. It is clear that starting with metastable precursors (such as N_2H_4 , N_3H) should lower polymerization pressure (compared to the lowest pressure of thermodynamically stable polymerization, 42 GPa). With different mixtures of N_2H_4 , N_3H and N_2 to produce N_3H or NH compounds, We found that using N_2 in the precursor mixture does not give good results. Instead, pure N_2H_4 and N_3H , or their mixtures can polymerize already at near-ambient conditions. For planetary interiors (where $\text{H}/\text{N} > 1$), we expect the presence of N-containing molecular ions at all pressures above ~ 55 GPa in NH_5 . This means a much thicker layer with ionic conductivity than previously thought, which will affect models of planetary magnetic fields (which are generated by convection of electrically conducting layers). High-pressure chemistry of hydronitrogens uncovered here has comparable or greater diversity than hydrocarbons. This invites the question whether nitrogen-based (rather than carbon-based) life is possible in the interiors of gas giant planets. This is not impossible - though at high temperature of planetary interiors - lifetime of metastable molecules (essential for life) will be short.

Table 4.1 Structure details of stable nitrogen hydrides compounds

Compounds	Pressure (GPa)	Structure Type	Subunits
N ₈ H	50 ~ 54	molecular*	NH ₅ + N ₂
N ₄ H	51 ~ 80	long-chain	
N ₃ H	42 ~ 75	long-chain	
N ₉ H ₄	50 ~ 60	two dimensional	N _x ⁻ plane + NH ₄ ⁺
N ₂ H	60 ~ 260	long-chain	
NH	36 ~ >800	(a) short chain (<i>P</i> ₂ ₁ / <i>c</i>)	N ₄ H ₄
		(b) dimer+long-chain(<i>P</i> ₁ , <i>C</i> ₂)	N ₂ H ₅ ⁺ + [] ⁻ ,
		(c) long-chain (<i>Fdd</i> ₂ , <i>Fddd</i>)	tetragonal spiral chain
NH ₂	200 ~ 780	molecular	N ₂ H ₄ (hydrazine)
N ₃ H ₇	140 ~ >800	(a) molecular/ionic	NH ₃ + N ₂ H ₄ / NH ₂ ⁻ + N ₂ H ₅ ⁺
		(b) ionic (<i>P</i> -3 <i>m</i> 1)	N ₃ ⁻ + N ₂ H ₆ ²⁺ + [] ⁺
NH ₃	0 ~ 460	molecular/ionic	NH ₃ / NH ₂ ⁻ + NH ₄ ⁺
NH ₄	50 ~ >800	molecular/ionic	NH ₃ + H ₂ / NH ₃ + NH ₄ ⁺ + H ⁻
NH ₅	55 ~ 100	ionic**	NH ₃ + [H ₃ N···H···NH ₃] ⁺ + H ⁻

* long-chain > 70 GPa, ** molecular < 42 GPa

 Table 4.2 Chemical reactions to synthesis high-energy-density hydronitrogen at $\Delta H = 0$

	Reaction	Pressure [GPa]	ΔV [³]
N ₃ H (HA*)	→ N ₃ H (long-chain)	6.0	7.58
N ₂ H ₄ + N ₃ H (HA)	→ 5NH (dimer+long-chain)	12.1, 12.8**	10.9, 9.81**
N ₂ H ₄ + N ₂ (<i>P</i> ₄ ₁ ₂ ₁ ₂ ₁)	→ 4NH (dimer+long-chain)	32.5	6.26
N ₂ H ₄ + 5N ₂ (<i>P</i> ₄ ₁ ₂ ₁ ₂ ₁)	→ 4N ₃ H (long-chain)	37.3	18.5

* HA shorts for Hydrazoic Acid

** With *C*₂ and *P*₂₁ N₂H₄ phases, respectively

Chapter 5

Phase Transition Pathway and Mechanism investigation

5.1 Phase Transition Investigation with VC-NEB

Nudged elastic band (NEB) method, a popular technique for studying reaction paths due to its efficiency, has not been extensively used in solid state physics because of the need to deal with the variation of the unit cell during solid-solid transformations. Here we present an extended technique—a variable-cell NEB (VC-NEB) technique combined with *ab initio* method, implemented in the USPEX code. Our technique is applied to reconstructive solid-solid phase transitions of GaN: from wurtzite to rocksalt (B4→B1) and from zincblende to rocksalt (B3→B1), this part is mainly basic on [143]. As more challenging applications, we study the mechanism of the recently predicted insulator-metal phase transition of BH, a unknown “phase X” investigation of MgF₂ and guiding materials synthesis. The results reveal that the VC-NEB technique is an efficient and general method and should have wide applications for studying the paths and mechanisms of reconstructive phase transitions. Results of the VC-NEB method can be considered as a starting point for a more sophisticated treatment using the transition path sampling method, the main prerequisite of which is to have an initial transformation trajectory.

5.1.1 Phase transition mechanism of B4→B1 and B3→B1 in GaN

In recent years, many theoretical models have been presented to explore phase transitions from wurtzite to rocksalt (B4→B1) [16, 20, 29, 91, 92, 150, 159, 164, 165, 194] and from zincblende to rocksalt (B3→B1) [11, 22–24, 60, 92, 113–116, 136, 158, 198] in II-VI, III-V and IV binary semiconductors. For the pressure-induced B4→B1 phase transition,

two representative *hexagonal* and *tetragonal* transition paths have been proposed. For the pressure-induced B3→B1 phase transition, based on the least-enthalpy calculation [22–24] the Landau-like model [113–116], and the extended uniaxial Bain path method [198], the *Imm2* symmetry as an intermediate activated state has been found. We revisit the B4→B1 and B3→B1 phase transitions in GaN by using the VC-NEB technique.

All calculations were performed in the framework of density functional theory by using the Quantum ESPRESSO code [52] and the PW91 exchange-correlation functional (GGA family) [134, 192]. The electron-ion interactions are described by ultrasoft pseudopotentials [178], with the $1s^2$ core configuration for the N atoms and the [Ar] core configuration for the Ga atoms. The kinetic energy cutoff for the plane wave expansion is 75 Ry and the k -point set is an $8 \times 8 \times 6$ grid of the reciprocal unit cell with a Γ -centered Monkhorst-Pack grid [172]. The common tangent construction [71] was used to predict the B4→B1 and B3→B1 transition pressures P_t in GaN. The results indicate $P_t = 45.7$ and 45.0 GPa, for B4→B1 and B3→B1, respectively, which are in good agreement with the previous theoretical and experimental values, as listed in Table 5.1.

Table 5.1 Structure parameters of B4, B3 and B1 structures for GaN at zero pressure. Other calculated and experimental values are also given for a comparison.

Phase	a (Å)	c/a	u	P_t (GPa)	B_0 (GPa)	B'_0
B4	3.123	1.629	0.377	45.7	170.6	4.34
	3.180 ^a	1.632 ^a	0.376 ^{a,c}	42.9 ^a	237 ^a	4.2 ^a
	3.145 ^c	1.633 ^c	0.377 ^a	43.7 ^b	245 ^a	3.2 ^a
	3.160-3.190 ^a	1.622-1.632 ^a		44.5 ^c 33.5 ^d	188 ^a	
B3	4.542			45.0	173.2	4.36
	4.497 ^a			42.1 ^a	196 ^a	4.2 ^a
	4.49-4.52 ^a			35.4-65 ^a	190 ^a	
B1	4.263	1.414	0.5		218.9	4.15
	4.225 ^a				240 ^a	4.5 ^a
	4.180 ^c				248 ^a 323 ^a	5.5 ^a 3.8 ^a

^aRef. [154] and references therein

^bDFT-LDA (ABINIT code) in Ref. [161]

^cDFT-LDA (VASP code) in Ref. [20]

^dDFT-LDA (PWSCF code) in Ref. [150]

For the VC-NEB method, in the first step, we should calculate the exact configurations of the two endpoint phases, by minimizing the enthalpy at constant pressure. In order to ensure the robustness of the VC-NEB method and to find the precise saddle point, the improved techniques presented in Refs. [47, 62, 63, 118], (including variable-elastic-constants, improved-tangent-estimate and climbing image NEB) are also utilized in our VC-NEB code. For all the VC-NEB calculations in this work, we take 27 intermediate images. For the halting criteria for performing the VC-NEB method, we choose 0.03 eV/\AA for the root-mean-square (RMS) force convergence (but 0.01 eV/\AA at saddle point) for the images. The spring constant is within a range of $0.2\text{--}1.5 \text{ eV/\AA}^2$, and the range is slightly narrower than that suggested in Ref. [47, 118].

B4→B1 phase transition GaN as an important semiconductor shows remarkable properties for technological applications. [121, 155] As is well known, GaN undergoes a B4→B1 phase transition under pressure. This phase transition process is in general summarized by two paths (*hexagonal* [91, 92, 150, 159, 194] and *tetragonal* [29, 91, 92, 150, 159, 164, 165, 194]). As shown in Fig. 5.1, both paths can be considered as two-stage processes with the coordination number changing from 4 to 6. A pair of particular free parameters (u, γ) are used to describe the structures. Based on the calculation methods as mentioned above, under the transition pressure $P_t = 45.7 \text{ GPa}$, the parameters u for the B4 and B1 phases are 0.377 and 0.5, respectively, in good agreement with the values reported in literature, as listed in Table 5.1.

For performing the VC-NEB calculation of the B4→B1 phase transition, we should focus on the detailed information on the saddle point, including the image position and the enthalpy barrier. First, by using the linear interpolation for all the dimensions of \mathbf{X} between the B4 and B1 phases, we generate the primary 27 intermediate images. After performing the VC-NEB procedure, we find the candidate transition path through the optimization. The results of the *tetragonal* path, as plotted in Figs. 3.7 and 5.2, show the dependence of the enthalpy H and the internal structural parameters (u, γ) on the image number. Without rotation-avoiding technique, as shown in Fig. 3.7, the enthalpy H has no change within the first 6 images (or the last 5 images), implying that the structure belongs still to the B4 (or B1) type. With the rotation-avoiding technique implemented in the VC-NEB calculation, a transformation enthalpy barrier of 0.34 eV/formula is found at image 15 in Fig. 5.2, which is close to 0.384 eV/formula in Ref. [20] and 0.37 eV/formula in Ref. [92]. As shown in Fig. 5.2b, γ changes from 60° at the initial image to 90° at image 23 and u increases from 0.377 to 0.427 during the lattice deformation. From image 23 to image 29, u increases from 0.427 to 0.5 and H decreases from 0.14 eV/formula to 0, while γ remains at 90° , implying that there indeed exists a *tetragonal* intermediate phase with a coordination number of 5. At the final state

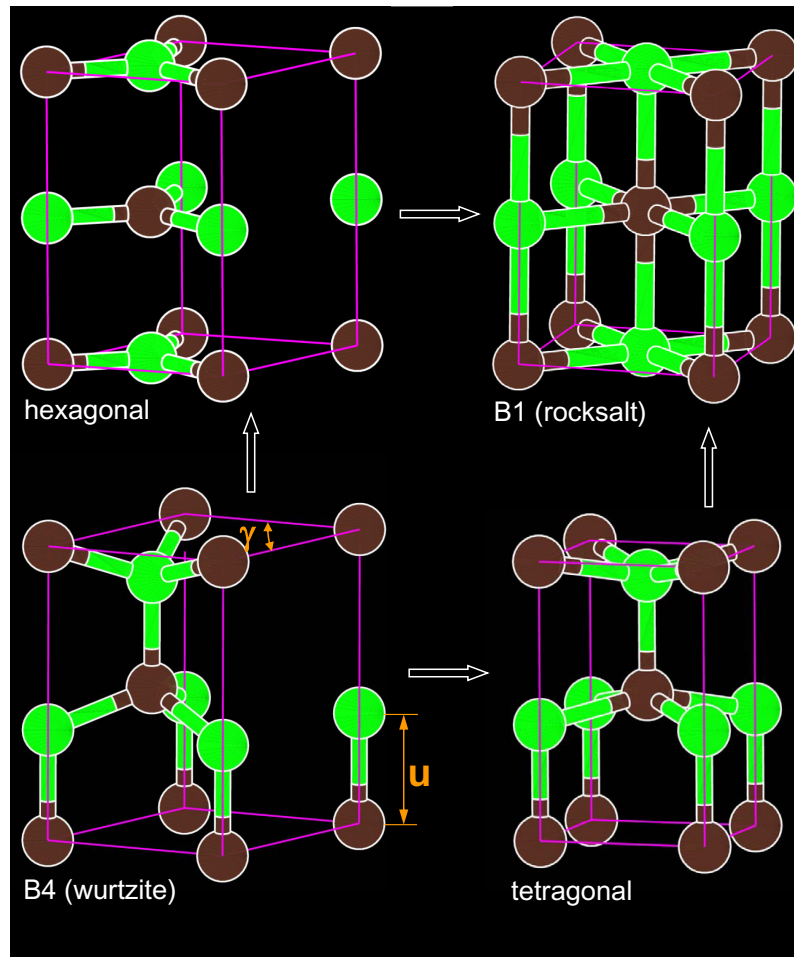


Fig. 5.1 Two representative paths for B4→B1 phase transition, through the *hexagonal* and *tetragonal* intermediate structures, respectively. The structural parameters (u, γ) denote the primary characteristics of these structures.

(image 29), H , u and γ are 0, 0.5 and 90° , respectively, indicating that the B4 (wurtzite) phase has transformed into the B1 (rocksalt) phase.

We now explore the *hexagonal* intermediate phase path and compare with the tetragonal path. The initial set of other intermediate images are generated by using the linear interpolation between the B4 and B1 structures and assigned to be the *hexagonal* structure. Starting from the assigned initial path, the VC-NEB calculation reveals the existence of another possible transition path, as shown in Fig. 5.3. From the initial structure to image 12, H increases from 0 to 0.31 eV/formula and u changes from 0.377 to 0.5, while γ keeps at 60° . Correspondingly the crystal structure changes from the B4 structure into the *h*-MgO

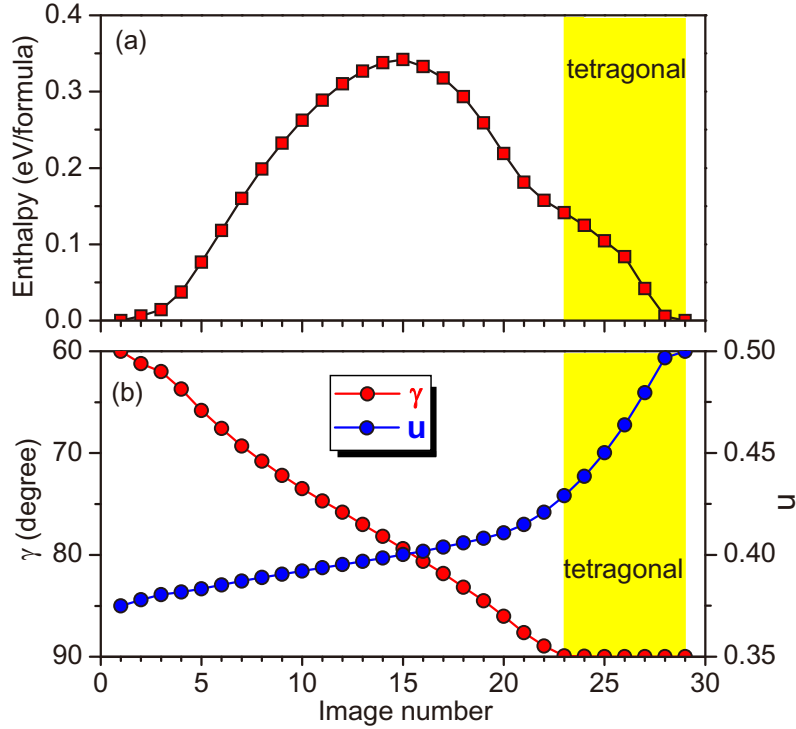


Fig. 5.2 Enthalpy barrier and evolution of internal structural parameters for the B4→B1 phase transition of GaN at the transition pressure along the “tetragonal” path. The saddle point is at image 15 with a barrier of 0.34 eV/formula.

structure with the coordination number of 5. From image 12 to image 29, u remains at 0.50 while γ increases from 60° to 90° , and the crystal structure transforms to the B1 structure. Following this transition path, the B4→B1 transition goes through an *hexagonal* intermediate phase and must overcome an enthalpy barrier of 0.39 eV/formula at image 20. The transformation enthalpy barrier along the *hexagonal* path is 0.05 eV/formula higher than that along *tetragonal* path, indicating that the tetragonal path should be preferred for the B4→B1 phase transition in GaN.

B3→B1 phase transition The VC-NEB method can also give a clear picture for the B3→B1 phase transition in GaN from the zincblend (B3) structure to the rocksalt (B1) structure. We assume for the moment that the primary path for the B3→B1 phase transition is based on a cooperative migration of atom positions from $(1/4, 1/4, 1/4)$ to $(1/2, 1/2, 1/2)$ along the cubic diagonal direction in the B3 phase [22–24]. All the 27 intermediate images are generated by the simple linear interpolation. After carrying out the VC-NEB procedure, a transition path (including the atomic positions in the intermediate images and the dependence of H on image number) is obtained through the VC-NEB calculations. Fig 5.4a shows H

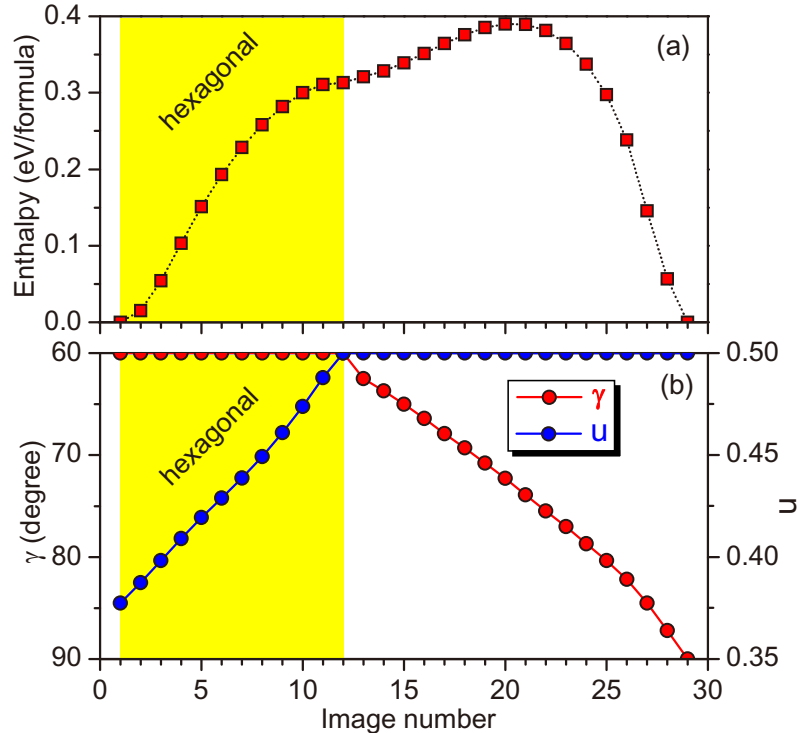


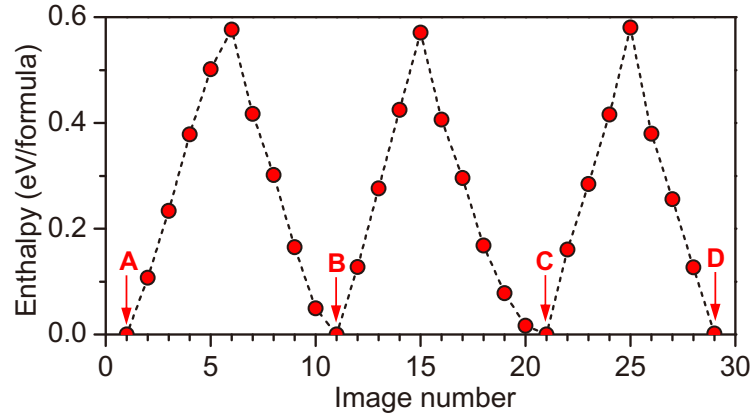
Fig. 5.3 Enthalpy barrier and internal structural parameters for the B4→B1 phase transition of GaN under transition pressure along the *hexagonal* path with a barrier of 0.39 eV/formula.

as a function of image number for the obtained transition path. It is clear that there are three enthalpy barriers (with almost the same barrier of 0.57 eV/formula and with their peaks located at images 6, 15 and 25). Correspondingly, there are two minimum enthalpy positions located at images 11 and 21, i.e., points B and C in Fig. 5.1a. After the geometry optimization, the exact structures at images 11 and 21 are shown in panels B and C in Fig. 5.1b, which correspond to the B1 and B3 structures (with the respective orthorhombic [22–24, 113–116, 136, 198] and monoclinic cells, respectively. [60, 113–116] We also confirm that the phase transition path from the initial image (B3 structure) to image 11 (B1 structure) goes through the common subgroup *Imm2*, consistent with the results reported in Refs.[22–24, 113–116, 136, 198].

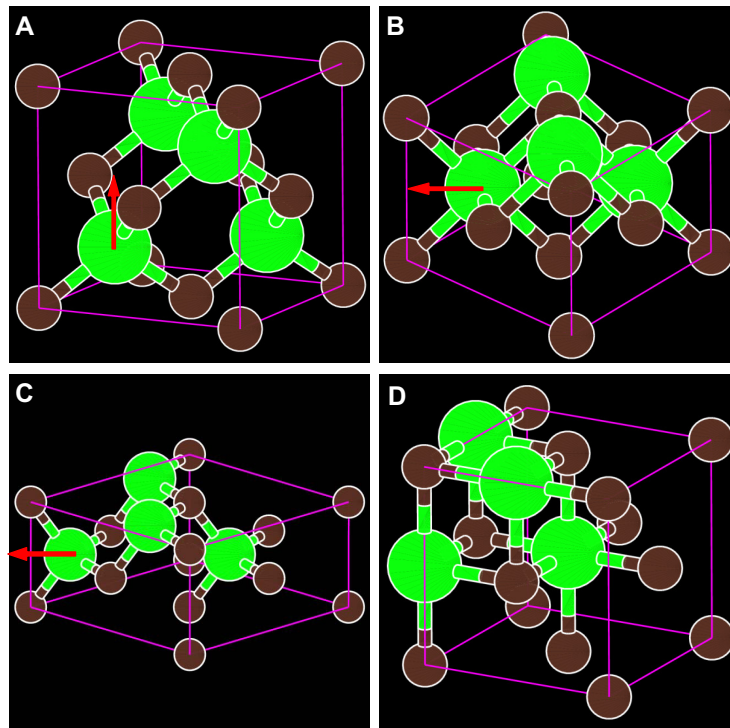
The VC-NEB calculations indicate that the B3→B1 transition path should be from $(1/4, 1/4, 1/4)$ to $(1/4, 1/4, 1/2)$ as shown from Panel A to Panel B in Fig. 5.4b, instead of the above supposed path from $(1/4, 1/4, 1/4)$ to $(1/2, 1/2, 1/2)$. Similarly, the transformations from image 11 (B1 structure) to image 21 (B3 structure) and from image 21 to image 29 (B1 structure) also contain the transition state with the *Imm2* space group. We also explore

5.1 Phase Transition Investigation with VC-NEB

the B3→B1 phase transition in AlN, and obtain similar results with the enthalpy barrier of 0.34 eV/formula and *Imm2* transition state [198].



(a)



(b)

Fig. 5.4 Enthalpy barrier of B3→B1 phase transition in GaN at the equilibrium pressure 45.0 GPa. At images 11 and 21, B1 and B3 structures in a monoclinic cell are found during the MEP searching, respectively. The Ga atoms move along the arrow directions during the phase transition.

5.1.2 Intermediate phases investigation in MgF_2

Magnesium fluoride (MgF_2) is of considerable interest as this mineral is one of the products of dissociation of post-perovskite (PPv) NaMgF_3 and behaves as a good low-pressure analog for SiO_2 . First-principles calculations [128, 174] and experiments [120] revealed that MgSiO_3 undergoes a reconstructive structure phase transition at ~ 125 GPa, from perovskite (Pv) to CaIrO_3 -type PPv phase, near the core-mantle boundary of the Earth. It is also predicted that MgSiO_3 would dissociate under an extreme condition above 1000 GPa and 10,000 K [175], into CsCl-type MgO and cotunnite-type SiO_2 . Unfortunately, this breakdown could not be observed experimentally, because the predicted dissociation pressure is too high to be achieved in the lab today. As an alternative, NaMgF_3 is proposed as a low-pressure analog [176] for experimental investigation of properties of the CaIrO_3 -type structure, since NaMgF_3 is also predicted to undergo the same Pv to PPv transformation at 18~22 GPa and meet a breakdown at 40~48 GPa, which is much lower than the phase transition and dissociation pressure of MgSiO_3 . The products, NaF and MgF_2 , from the dissociation of PPv-type NaMgF_3 are also good analog materials for MgO and SiO_2 , respectively.

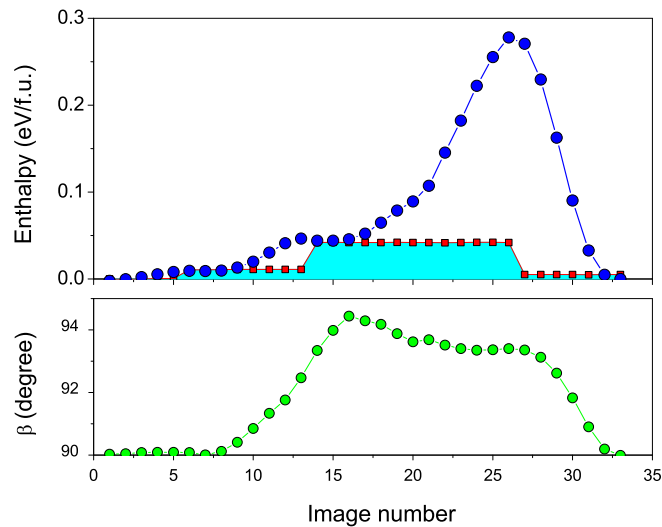


Fig. 5.5 Transformation barrier for pyrite \rightarrow cotunnite structural transition of MgF_2 at $P = 45.0$ GPa. The intermediate orthorhombic and baddeleyite-type MgF_2 structures are found along the pathway at image 7 and image 16. The saddle point is at the 26 image with a barrier 0.28eV/f.u.. The blue stage indicates relative enthalpy of the fully relaxed images.

5.1 Phase Transition Investigation with VC-NEB

MgF₂ undergoes the same sequence of pressure-induced transformation as SiO₂: rutile → α -PbO₂ → PdF₂ → α -PbCl₂ [59]. Recently, experiments from Grocholski's work [57] show that MgF₂ may not transform from pyrite-type to cotunnite-type directly, but preceded a post-pyrite "phase X" in a very narrow pressure range. A very small density increase of this "phase X" appears to have a coordination number (CN) between high (9) in cotunnite phase and low CN (6) in pyrite phase. This phase X or mixture of phases may be a quenchable high temperature phase as it is synthesized above ~1500 K in these experiments. The expected breakdown of NaMgF₃ was not observed at well above P - T condition in the experiment, which is stable till at least 70 GPa and 2500K [176]. Therefore, the determination of the structure for "phase X" would greatly help in investigating the properties of the PPv structure, including its dissociation.

The VC-NEB method was used for MgF₂ pyrite → cotunnite transition at 45 GPa to 60 GPa, trying to reveal the phase transition mechanism and reveal the fact of encountering a unclear metastable phase. 15 intermediate images are generated with linear interpolation method between the intial (pyrite-type) and final (cotunnite-type) structures at first. The improved-tangent-estimate, climbing-image, rotation-avoiding technique [143] and variable number of images technique are utilized in the VC-NEB calculations. After the transition pathway fully converged, structural relaxations of the final 31 images were approached

Table 5.2 Structural data and atomic coordinates in the orthorhombic ($Pca2_1$) and baddeleyite-type ($P2_1/c$) MgF₂ at 45 GPa.

	LDA	GGA
orthorhombic MgF ₂ ($Pca2_1$)		
(a, b, c) , Å	(4.662, 4.373, 4.421)	(4.704, 4.483, 4.525)
Mg ($4a$)	(0.040, 0.772, 0.979)	(0.536, 0.769, 0.986)
F ₁ ($4a$)	(0.108, 0.602, 0.386)	(0.613, 0.600, 0.382)
F ₂ ($4a$)	(0.767, 0.925, 0.704)	(0.277, 0.924, 0.701)
Volume, Å ³	90.13	95.42
baddeleyite-type ($P2_1/c$)		
(a, b, c) , Å	(4.323, 4.733, 4.388)	(4.794, 4.421, 4.480)
β	94.38°	94.62°
Mg ($4e$)	(0.778, 0.044, 0.216)	(0.043, 0.777, 0.215)
F ₁ ($4e$)	(0.609, 0.103, 0.767)	(0.105, 0.606, 0.769)
F ₂ ($4e$)	(0.925, 0.763, 0.496)	(0.763, 0.928, 0.496)
Volume, Å ³	89.78	94.64

independently to search the local metastable structures around the phase transition pathway in the VC-NEB code. The FIRE algorithm [10] is utilized in both the VC-NEB and structural relaxation calculations, and a very small time step is used in the structural relaxation to avoid the images running away from the local minima. All first-principles calculations were carried out with the projector augmented wave (PAW) method as implemented in the VASP code.[83] A plane-wave cutoff of 550 eV and an automatic variable k -point gridmesh were used. Exchange and correlation effects were treated using the PBE GGA exchange-correlation functional [133].

In Fig 5.5, the VC-NEB results show that the pyrite-type \rightarrow cotunnite-type reconstructive phase transition can be considered as a three stage transformation. From image 1 to image 7, MgF_2 first transforms from a cubic cell into an orthorhombic structure, which is considered to be a displacive transition. A metastable orthorhombic MgF_2 is found at image 7, with the enthalpy $\sim 0.01\text{eV/f.u}$ higher than the pyrite-type. The cation CN changes from 6 in pyrite phase to 7 in this new orthorhombic phase. Then, starting from the orthorhombic structure, the images transform into another metastable baddeleyite-type structure at image 15 which has a $CN = 7$ (or maybe 8) as well. Within a symmetry tolerance of 0.05 \AA , the images from 15 to 30 have a $P2_1/c$ space group, and a 0.28 eV energy barrier at image 26 along the transformation pathway. Structural relaxation shows that intermediate structures are near the orthorhombic phase from image 6 to image 12, and the next 13 images would easily fall into the baddeleyite-type structure.

Careful analysis of the two metastable structures reveals that the orthorhombic MgF_2 is a good candidate structure for the experimentally observed “phase X”. The unit cell volume decreases through the post-pyrite transition by $\sim 1.3\%$ at 45.0 GPa , which is very close to the experimental results in Ref. [57], and decreases by $\sim 2.0\%$ at 50.0 GPa . The shortest covalent Mg-F bond length also decreases through the transition by $\sim 1\%$. This structure would easily go to pyrite-type through structural relaxation below $\sim 44 \text{ GPa}$. The baddeleyite-type structure has a higher coordination number and a volume decrease larger than orthorhombic MgF_2 , as shown in Fig. 5.6b.

5.1.3 the VC-NEB method in guiding materials synthesis

Above, using the example of GaN, we have shown that the VC-NEB method is a good way for studying mechanisms of pressure-induced phase transitions. In this section, we investigate a 2D insulator - 3D metal structural transformation of BH at high pressure.

Synthesis of BH phases Solid B-H compounds are important because of potential application as high-energy-density materials and potential high-temperature superconductors. Recently,

5.1 Phase Transition Investigation with VC-NEB

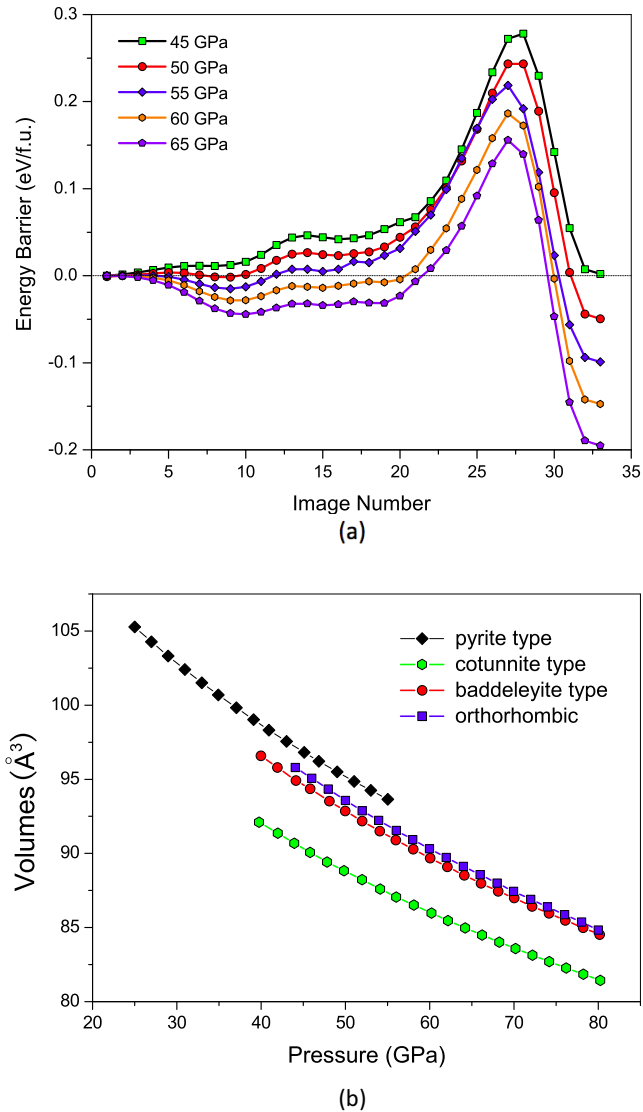


Fig. 5.6 (a) Transformation barrier for pyrite \rightarrow cotunnite structural transition of MgF₂ at various pressures. The intermediate orthorhombic type MgF₂ structure at image 8 is always energy preferred than the pyrite phase above 50 GPa, which is considered as a good candidate for “phase X”. (b) Volume compression of MgF₂ with pressure. The volume of the orthorhombic structure is $\sim 1.5\%$ smaller than pyrite type. The baddeleyite type MgF₂ is $\sim 2\%$ denser than pyrite type.

it was predicted [69] that the simplest stable boron hydride at ambient conditions, diborane (B₂H₆), at high pressures above 153 GPa above breaks down into *Ibam*-BH and H₂. The *Ibam* phase of BH is insulating and has a clear layered structure. At 168 GPa it was predicted

to transform into a $P6/mmm$ structure, which is metallic and has a 3D-connected topology. The VC-NEB method has helped us to study the mechanism of this transition.

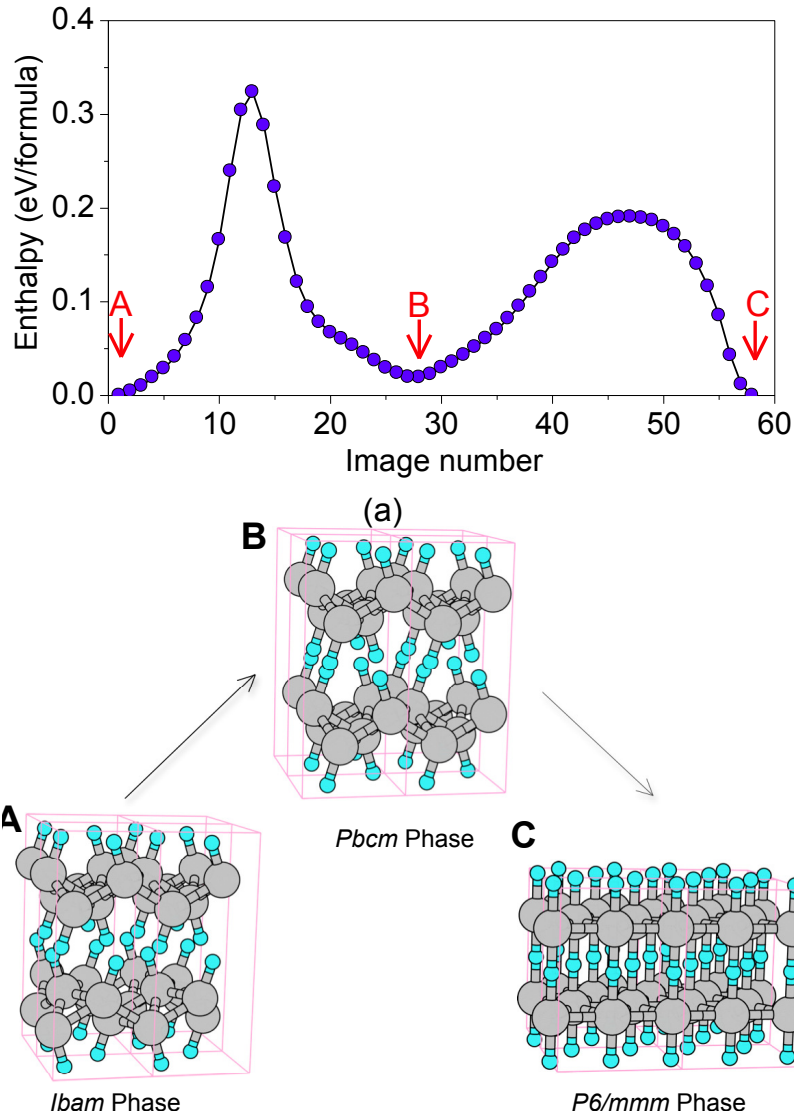


Fig. 5.7 The $Ibam \rightarrow P6/mmm$ transition of BH system at 168 GPa. A *Pbcm* intermediate phase is revealed. The saddle points on $Ibam \rightarrow Pbcm$ and $Pbcm \rightarrow P6/mmm$ segments have barriers of 0.32 and 0.19 eV/formula, respectively.

For every image, we use a cell containing 8 formula units. For greater confidence, we explored several initial pathways between the initial (*Ibam*) and final (*P6/mmm*) shape cell structures with linear interpolation method and manual configurations. We set configurations of $\mathbf{X}_1 = (\epsilon_{Ibma}; \mathbf{r}_{P6/mmm})$ and $\mathbf{X}_2 = (\epsilon_{P6/mmm}; \mathbf{r}_{Ibma})$ as the intermediate phases in the B-H

5.1 Phase Transition Investigation with VC-NEB

system VC-NEB pathway initialization. ϵ_{Ibma} , $\epsilon_{P6/mmm}$, $\mathbf{r}_{P6/mmm}$ and \mathbf{r}_{Ibma} are the finite strain tensors and atom fraction coordinates in the of *Ibma* and *P6/mmm* B-H phases at 168 GPa respectively. The electronic structure calculations were carried out within the PBE96 functional [133] using the projector augmented wave (PAW) method as implemented in the VASP code. We use the plane-wave kinetic energy cutoff of 540 eV and Γ -centered Monkhorst-Pack meshes with reciprocal space resolution of $2\pi \times 0.03 \text{ \AA}^{-1}$. After performing the VC-NEB calculations, all initial pathways converged to the same one, which features the *Pbcm* structure as a transition state. Fig. 5.7 shows the enthalpy profile for this transition from the VC-NEB results. In the first stage (*Ibam* \rightarrow *Pbcm*) of the transition, antiparallel BH-layers are reconstructed into a “parallel” arrangement (see Fig. 5.7b), with a 0.32 eV/formula enthalpy barrier. Then the interlayer distance is decreased (until B-H-B bonds connecting these layers are formed) and layers gradually become flat in the *P6/mmm* structure. This stage has a much lower enthalpy barrier 0.19 eV/formula. This mechanism implies that low-temperature decompression of the *P6/mmm* phase may lead to the *Pbcm* structure, rather than the *Ibam* structure.

Synthesis of polymeric N_3H These long-chain polymeric hydronitrogen compounds would be a great alternative to commonly used high-energy-density materials. Compared to pure polymeric nitrogen (cg-N phase), layered *P2₁/c* N_3H is stable starting from ~ 42 GPa, i.e. at pressures lower than the stability pressure of cg-N (> 56 GPa). Hydrazoic acid [44] (N_3H) may be an even better precursor for synthesizing long-chain polymers. With hydrazoic acid, the layered *P2₁/c* N_3H can be formed at as low as 6.0 GPa (See Tab. 2). The VC-NEB [143] calculation indicates that the phase transformation from hydrazoic acid to *P2₁/c* N_3H has an energy barrier of ~ 0.25 eV/atom at 10 GPa, (See Fig. 5.8), and occurs in several stages. In the first stage, some H-bonds between HN_3 molecules break making the molecules free to rotate (as shown in Fig. 5.8 from image 1 to 5). After adjusting directions of HN_3 molecules (images 5 to 18), metastable short N-chain molecules (image 21 and image 27) appear during the transition, new nitrogen-nitrogen bonds appear, eventually leading to infinite polymeric chains (image 30). The energy barrier of first stage with rotation of the HN_3 molecules is around 0.15 eV (from images 1 to 19), and approximately equals the barrier of the second stage (nitrogen-nitrogen bond formation). The transition should happen easily in liquid hydrazoic acid. Mixture of hydrazine and hydrazoic acid are an alternative precursor, with polymerization estimated to happen at ~ 13 GPa (See Tab. 2).

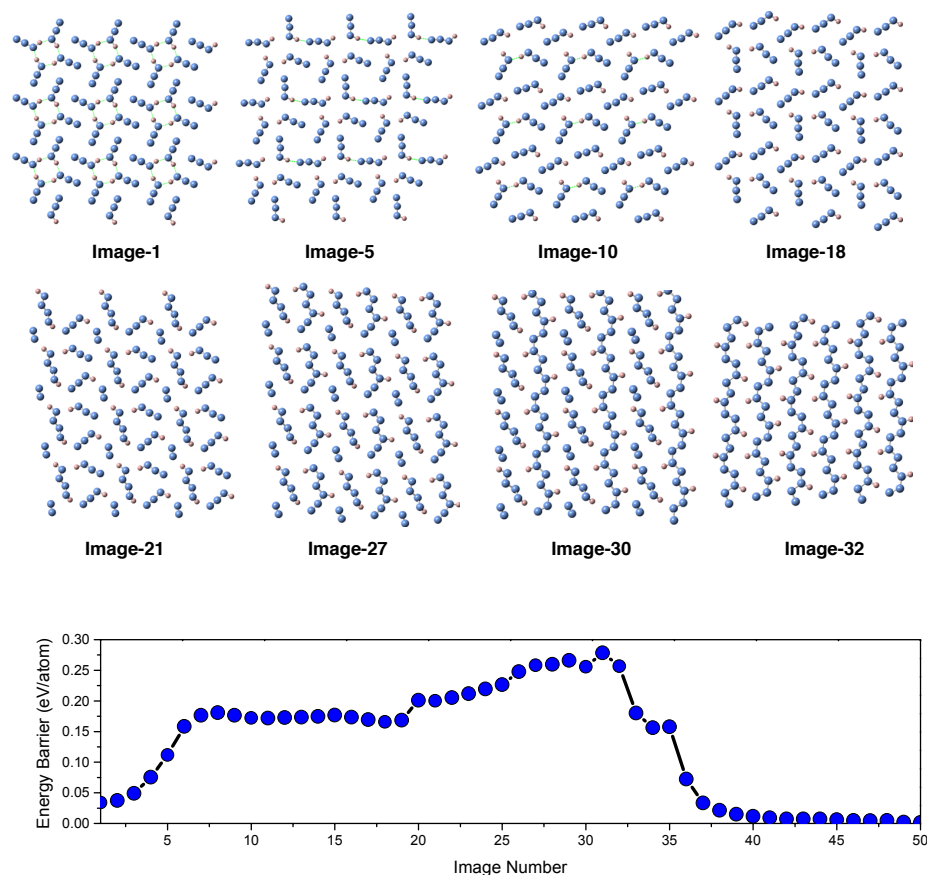


Fig. 5.8 Mechanism and energy barrier of hydrazoic acid to $P2_1/c$ N_3H phase transition revealed by the VC-NEB method. A unit cell with 32 atoms was used during the pathway calculation. Only one layer of N_3H structures during the phase transition are shown at specific images.

5.2 Phase transition investigation for argon in USPEX

USPEX provides a general way for phase transition mechanism investigation at different levels, starting with evolutionary metadynamics for primary phase transition mechanism study, VC-NEB method provides a static picture of transformation pathway and enables searching for different feasible pathways, while higher-level TPS approach gives a detailed dynamical picture with nucleation at a large scale. Here we present the phase transition mechanism investigation of fcc \rightarrow hcp in argon system under the framework of USPEX. In

rare gas solids, the weak van der Waals interatomic interactions plays an important role in the phase transition process. Understanding the physics of these simple materials is helpful for uncovering physics of the more complex materials. Many theoretical [80, 81, 147] and experimental [77, 82] studies indicated different possible mechanisms of the fcc→hcp transition in argon nanoclusters, which is related to the size of the system. Here we are studying the mechanism the fcc-to-hcp transition at ambient pressure within USPEX.

5.2.1 Phase diagram tree from evolutionary metadynamics simulation

An initial structure based on a unit cell containing just two argon atoms is used in performing generalized evolutionary metadynamics (GEM) simulations, which enable the increase of the size of the unit cell based on the selected eigenvector of the vibration modes for softmutation. The maximum number of atoms in an expanded unit cell was set to 24. To build up a clear tree of phase transitions, we ran three different GEM calculations with different heights and widths of Gaussians added to the energy surface to accelerate phase transitions. Structure relaxations were done using DFT within vdW functional optB88-vdW [78] to have accurate energies.

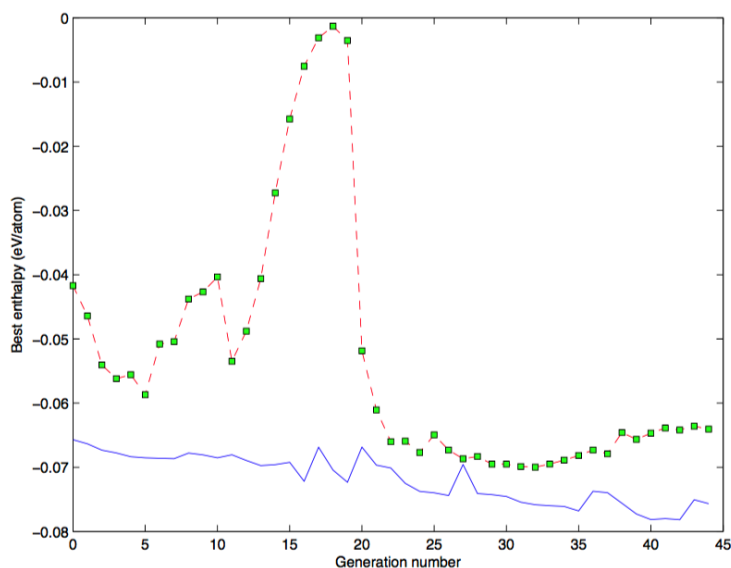


Fig. 5.9 Enthalpy evolution in GEM simulation at ambient pressure starting from the hcp structure (red dash line: enthalpies for best structures; blue line: enthalpies for best structures after full relaxation). The structures undergo amorphous phases after at 18 generations.

Capable of searching for the neighbor phases on the energy surface, evolutionary metadynamics has built a phase diagram tree of argon, shown in Fig. 5.10. Besides the

fcc and hcp phases, monoclinic, orthorhombic, trigonal, hexagonal structures are all covered in the phase diagram tree. In Fig. 5.10, only a part of the phase diagram tree is illustrated to reveal the main possible transformations in argon, others are not shown. For the fcc→hcp transformation, all three transformation models [82] (one monoclinic and two orthorhombic schemes) are found in our GEM calculations, either as direct transitions or through intermediate phases. These phase transition models give good initial pathways for detailed transformation mechanism investigation with VC-NEB and TPS approaches.

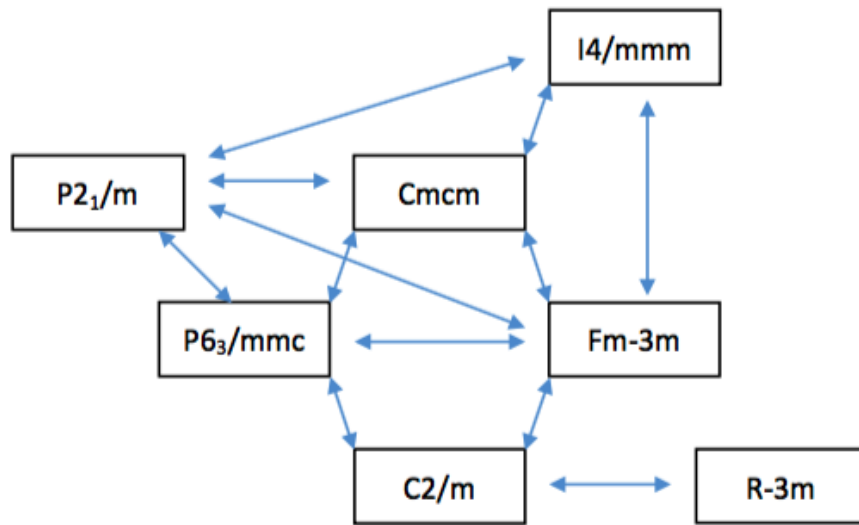


Fig. 5.10 Phase diagram tree built from the GEM calculations. Many low-symmetry phases are ignored for clarity.

5.2.2 Transformation pathway investigation with VC-NEB method

With the given transformation models found in GEM calculations, the VC-NEB calculations were performed for the monoclinic and another two orthorhombic schemes, separately. The VC-NEB calculations were done with Lennard-Jones pair potential with parameters $\epsilon/k_B = 119.8$ K and $\sigma = 0.3405$ nm [149], using the minimum physically sufficient for these transitions cells, containing four argon atoms.

For the monoclinic transformation model, no stable pathway was found by USPEX. For the orthorhombic-1 scheme, a pathway with an energy barrier ~ 4 meV/atom was uncovered by VC-NEB calculations, as shown in Fig 5.11. Along this pathway, the fcc→hcp transformation is a three-stage transition process. From image 1 to image 10, the cubic unit cell undergoes a distortion to tetragonal then to monoclinic shape, accompanied with

5.2 Phase transition investigation for argon in USPEX

displacement of the argon atoms (shown in Fig 5.12). From image 10 to image 14, larger distortion of the unit cell and displacement of the atoms are found during this stage. Image 10 and 14 are two metastable phases with $C2/m$ symmetry. Then, at the last stage of the transition, with the argon atoms moving to form close-packed pattern, the structure turns to the hcp phase. In contrast, a pathway with transformation barrier ~ 5 meV/atom is revealed by VC-NEB starting with the orthorhombic-2 scheme, which is considered [82] as the hcp nanoclusters growth mechanism from fcc fragments. For our static VC-NEB results, the pathway undergoing the $C2/m$ metastable phases is energetically preferred than the orthorhombic-2 scheme.

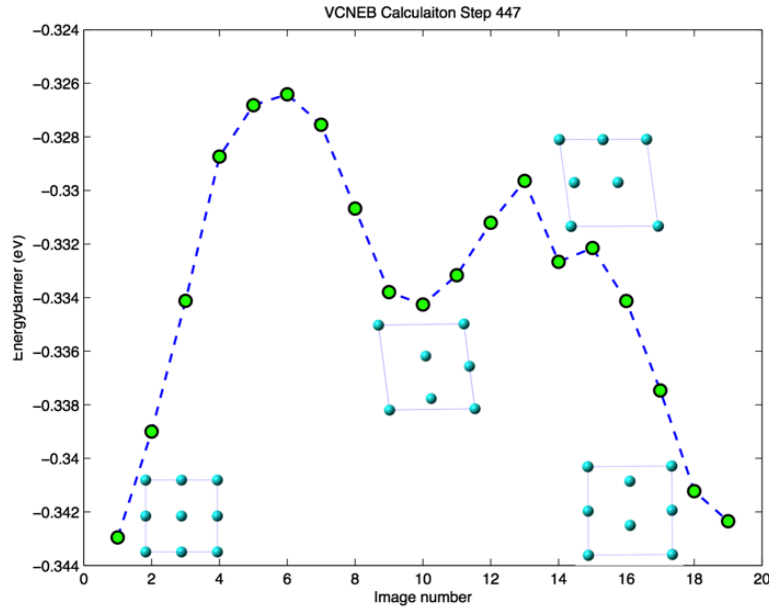


Fig. 5.11 Energy barrier for fcc \rightarrow hcp structure transition for argon found in a VC-NEB calculation.. The initial pathway is same as the orthorhombic-1 model in Ref. [82]. At images 10 and 14, two intermediate $C2/m$ phases are found as metastable states during the transformation.

5.2.3 Nucleation study with TPS approach

To consider the effect of temperature and nucleation on the fcc \rightarrow hcp phase transition mechanism, the TPS approach is applied to study the transformation for systems with 1000 and 18000 argon atoms at 40 K. Moreover, TPS has the ability of finding superior and non-intuitive transformation mechanisms, given an initial mechanism (even a suboptimal one).

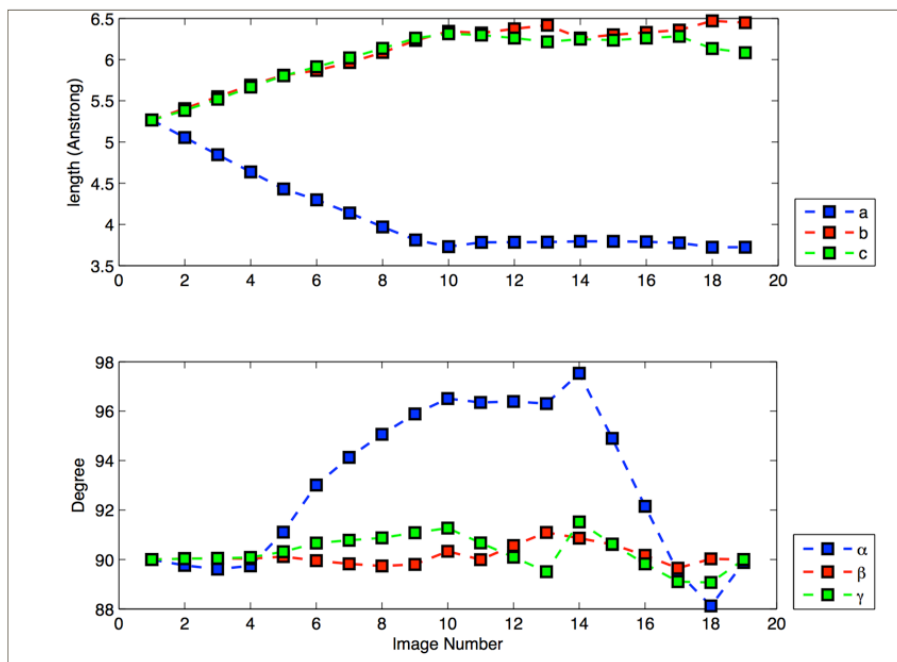


Fig. 5.12 Evolution of structural parameters of the fcc \rightarrow hcp phase transition revealed by VC-NEB. The initial and final structure are described in orthogonal settings, with $\alpha = \beta = \gamma = 90^\circ$.

For generating the first trajectory for TPS simulation, dense images are interpolated near the saddle point (image 6 as shown in Fig. 5.11) at the energetically preferred pathway from VC-NEB result. Supercells of 1000 and 18000 atoms are created from these interpolated images, respectively; then, the MD simulations with $+t$ and $-t$ are performed to get a complete phase transition trajectory from fcc to hcp phase. For the first trajectory initialization, it almost has a 100% success rate in generating it starting from the saddle point image or the interpolated images less than 3000 atoms. It becomes difficult when the size of system gets larger. For the system with 18000 atoms, we get only around 1% success rate to have a good trajectory reaching both the fcc and hcp phases among all the MD calculations.

In the TPS simulation for 1000 argon atoms, the fingerprint OP similarity criterion is set as [0.995 0.996] in reference to fcc and hcp respectively, to distinguish the phases. The snapshots of a typical trajectory of the phase transition are shown in Fig. 5.13. Focussing on the phase transformation process in our analysis, a time slice of the MD trajectory is selected as 0 ps, where the atoms are arranged in a face-centered cubic pattern and the phase transition is beginning to happen. At ~ 0.15 ps, a boundary of a new intermediate phase and

the initial fcc phase is found. Then, the boundary propagates to the whole system at ~ 0.40 ps. The intermediate phase has an orthorhombic structure, and ABAB packing. The new intermediate phase lasts for 0.2 ps, then typical hexagonal holes of hcp pattern develop in the middle of the cell, as shown in Fig. 5.13(d). Then the whole argon crystal forms the hcp structure at ~ 1.25 ps. Snapshots of the nucleation of the orthorhombic and hcp phases in the system with 18,000 argon atoms are shown in Fig 5.15. The yellow dashed circles indicate the nucleation of the orthorhombic structure in (a) and hexagonal phase in (b).

In the system of 1000 argon atoms, sometimes the MD trajectory is easily trapped in the intermediate phase, which has a fingerprint cosine similarity with the hcp phase close to 0.995, as shown in Fig. 5.14. Thus, to successfully distinguish the hcp and the intermediate phase, a fingerprint OP criteria reference to hcp structure up to 0.996 is critical.

From the general investigation procedure of phase transition mechanism in USPEX, a whole picture of the phase transition mechanism of fcc \rightarrow hcp is revealed. The evolutionary metadynamics approach helps build up a whole picture of low-enthalpy phases and possible phase transition mechanisms for argon. The VC-NEB method indicates a pathway with a $C2/c$ metastable phase during the structural transformation. Finally, the TPS approach found a different mechanism going through an orthorhombic intermediate phase where two nucleation events happened during the transformation. The energy barrier is around 4 meV/atom in VC-NEB calculation, and around 2.2 meV/atom with 1000 argon atoms, and decreases to ~ 0.6 meV/atom in with 18,000 argon atoms from TPS simulations.

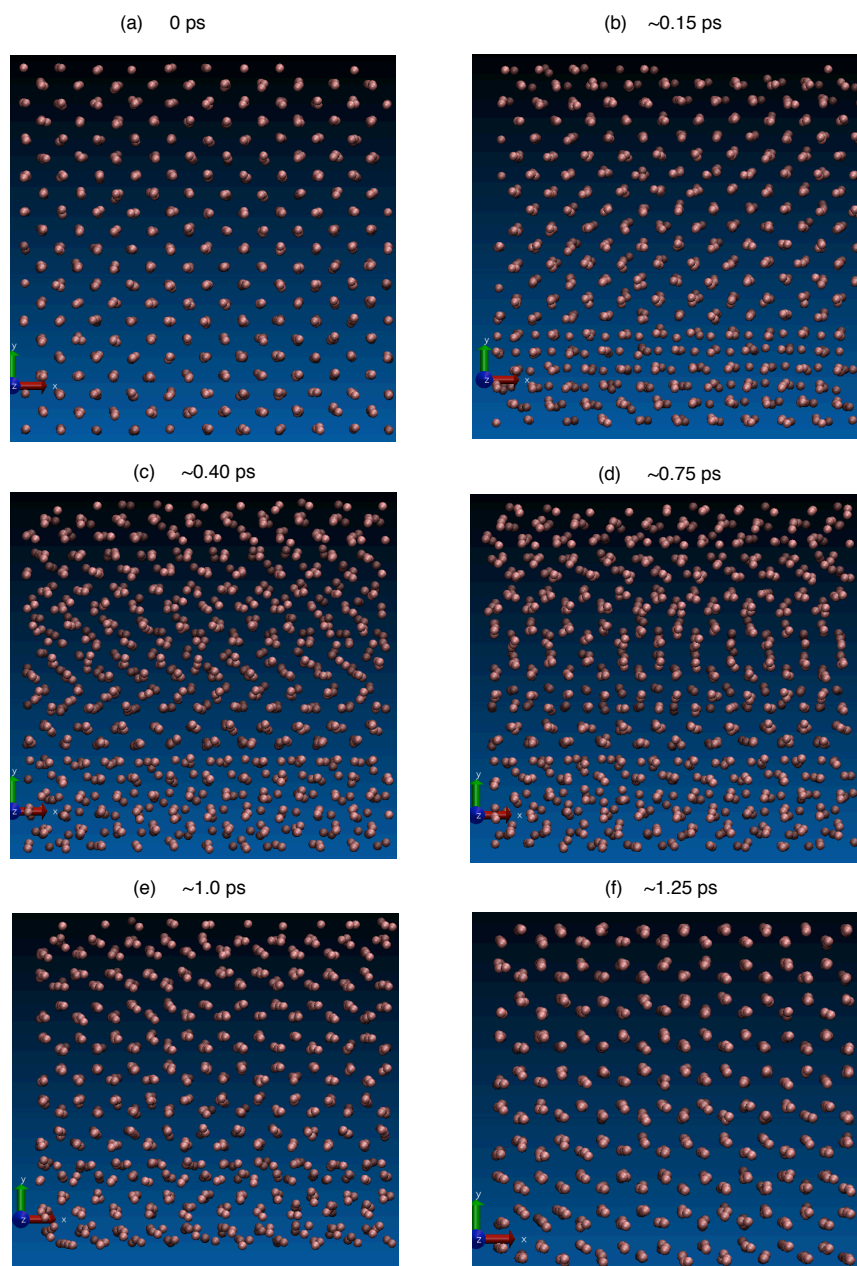


Fig. 5.13 Snapshots taken from a representative trajectory of the real mechanism for the fcc \rightarrow hcp phase transition.

5.2 Phase transition investigation for argon in USPEX

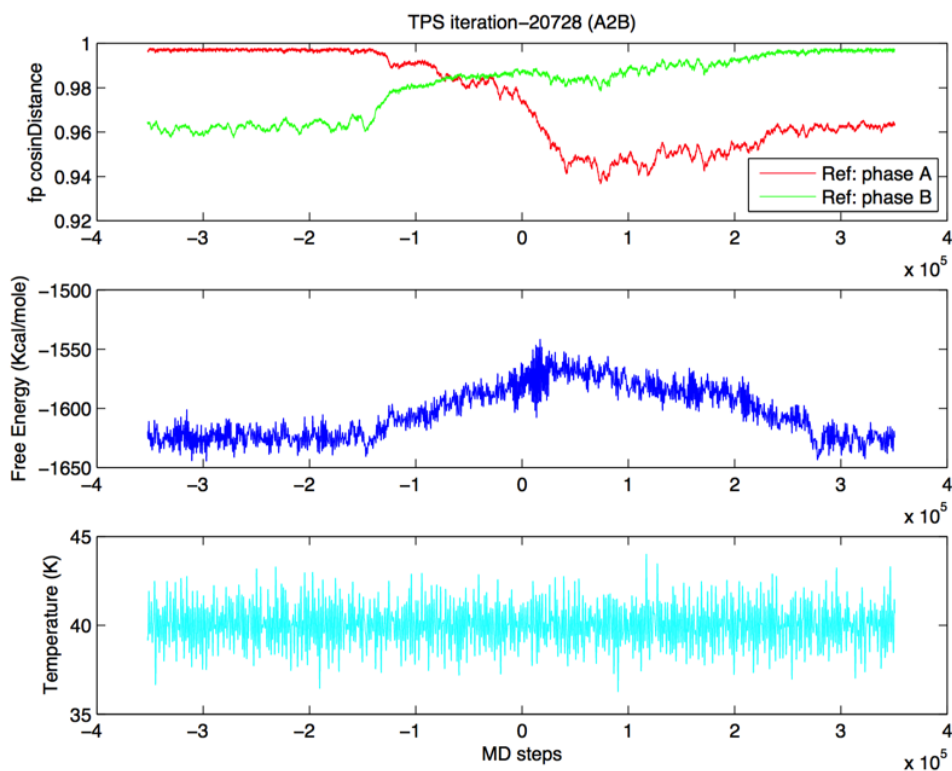
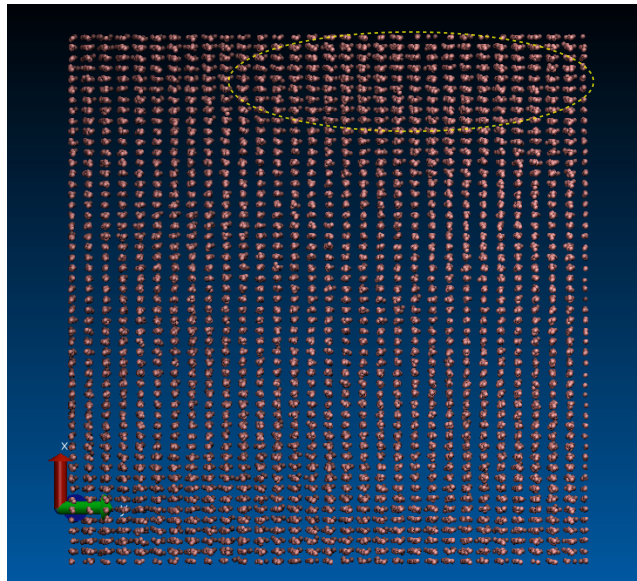


Fig. 5.14 Evolution of the fingerprint cosine similarity, free energy and temperature in a successful MD TPS trajectory. A and B indicate fcc and hcp phases, respectively. The red and green lines are the cosine similarities of the structures to the fcc and hcp phases, respectively. The top subfigure indicates a successful MD simulation of the fcc→hcp transformation. There are 70, 000 MD steps in total, time step is 0.1 fs.

(a)



(b)

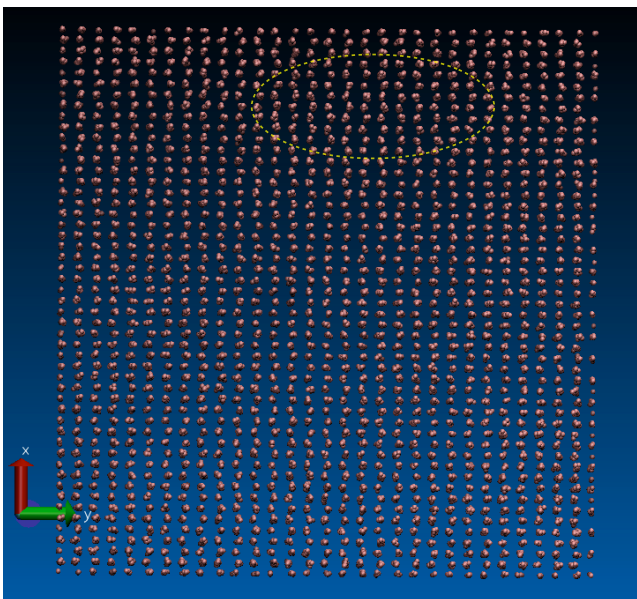


Fig. 5.15 Snapshots taken from a representative trajectory of the nucleation of the orthorhombic and hcp phases. The yellow dashed circles indicate the site of nucleation.

References

- [1] Adamo, C. and Barone, V. (1999). Toward reliable density functional methods without adjustable parameters: The PBE0 model. *J. Chem. Phys.*, 110(13):6158–6170.
- [2] Anisimov, V. I., Zaanen, J., and Andersen, O. K. (1991). Band theory and mott insulators: Hubbard U instead of Stoner I. *Phys. Rev. B*, 44(3):943.
- [3] Babaev, E., Sudbø, A., and Ashcroft, N. (2005). Observability of a projected new state of matter: a metallic superfluid. *Phys. Rev. Lett.*, 95(10):105301.
- [4] Bader, R. F. W. (1990). *Atoms in Molecules - A Quantum Theory*. Oxford University Press.
- [5] Ball, P. (1996). Scandal of crystal design... *Nature*, 381(6584):648–650.
- [6] Banister, A. J. and Gorrell, I. B. (1998). Poly(sulfur nitride): The first polymeric metal. *Adv. Mater.*, 10(17):1415–1429.
- [7] Bartlett, R. J. and Stanton, J. F. (2007). Applications of post-Hartree-Fock methods: A tutorial. *Rev. Comput. Chem.*, 5:65–169.
- [8] Becke, A. D. (1993). Density-functional thermochemistry. III. the role of exact exchange. *J. Chem. Phys.*, 98(7):5648–5652.
- [9] Berezhkovskii, A. and Szabo, A. (2005). One-dimensional reaction coordinates for diffusive activated rate processes in many dimensions. *J. Chem. Phys.*, 122(1):014503.
- [10] Bitzek, E., Koskinen, P., Gähler, F., Moseler, M., and Gumbsch, P. (2006). Structural relaxation made simple. *Phys. Rev. Lett.*, 97:170201.
- [11] Blanco, M. A., Recio, J., Costales, A., and Pandey, R. (2000). Transition path for the B3 \rightleftharpoons B1 phase transformation in semiconductors. *Phys. Rev. B*, 62(16):R10599.
- [12] Blatov, V. A. and Proserpio, D. M. (2010). Periodic-graph approaches in crystal structure prediction. *Modern methods of crystal structure prediction*.
- [13] Blöchl, P. E. (1994). Projector augmented-wave method. *Phys. Rev. B*, 50:17953–17979.
- [14] Bolhuis, P. et al. (1998). Sampling ensembles of deterministic transition pathways. *Faraday Discuss.*, 110:421–436.
- [15] Bolhuis, P. G., Chandler, D., Dellago, C., and Geissler, P. L. (2002). Transition path sampling: Throwing ropes over rough mountain passes, in the dark. *Annu. Rev. Phys. Chem.*, 53(1):291–318.

- [16] Boulfefel, S., Zahn, D., Grin, Y., and Leoni, S. (2007). Walking the path from B4-to B1-type structures in GaN. *Phys. Rev. Lett.*, 99(12):125505.
- [17] Boulfefel, S. E. (2009). Atomic scale investigation of pressure induced phase transitions in the solid state. (*Doctoral dissertation, Technische Universität Dresden*).
- [18] Boulfefel, S. E., Zahn, D., Hochrein, O., Grin, Y., and Leoni, S. (2006). Low-dimensional sublattice melting by pressure: Superionic conduction in the phase interfaces of the fluorite-to-cotunnite transition of CaF_2 . *Phys. Rev. B*, 74(9):094106.
- [19] Buerger, J. M. (1951). *Phase Transformation in Solids*. Wiley.
- [20] Cai, J. and Chen, N. (2007). Microscopic mechanism of the wurtzite-to-rocksalt phase transition of the group-III nitrides from first principles. *Phys. Rev. B*, 75(13):134109.
- [21] Caspersen, K. J. and Carter, E. A. (2005). Finding transition states for crystalline solid–solid phase transformations. *Proc. Natl. Acad. Sci. USA*, 102(19):6738–6743.
- [22] Catti, M. (2001). Orthorhombic intermediate state in the zinc blende to rocksalt transformation path of SiC at high pressure. *Phys. Rev. Lett.*, 87(3):035504.
- [23] Catti, M. (2002). First-principles study of the orthorhombic mechanism for the B3/B1 high-pressure phase transition of ZnS. *Phys. Rev. B*, 65(22):224115.
- [24] Catti, M. (2003). Ab initio predicted metastable TII-like phase in the B1 to B2 high-pressure transition of CaO. *Phys. Rev. B*, 68(10):100101.
- [25] Cavazzoni, C., Chiarotti, G. L., Scandolo, S., Tosatti, E., Bernasconi, M., and Parrinello, M. (1999). Superionic and metallic states of water and ammonia at giant planet conditions. *Science*, 283(5398):44–46.
- [26] Chandler, D. (1978). Statistical mechanics of isomerization dynamics in liquids and the transition state approximation. *J. Chem. Phys.*, 68(6):2959–2970.
- [27] Chandler, D. (1987). Introduction to modern statistical mechanics. *Introduction to Modern Statistical Mechanics, by David Chandler, pp. 288. Foreword by David Chandler. Oxford University Press, Sep 1987. ISBN-10: 0195042778. ISBN-13: 9780195042771, 1.*
- [28] Chau, P.-L. and Hardwick, A. (1998). A new order parameter for tetrahedral configurations. *Molecular Physics*, 93(3):511–518.
- [29] Corll, J. A. (1967). Effect of pressure on the elastic parameters and structure of CdS. *Phys. Rev.*, 157(3):623.
- [30] Crowhurst, J. C., Zaug, J. M., Radousky, H. B., Steele, B. A., Landerville, A. C., and Oleynik, I. I. (2014). Ammonium azide under high pressure: A combined theoretical and experimental study. *J. Phys. Chem. A*, 118(38):8695–8700.
- [31] Degtyareva, O., Gregoryanz, E., Somayazulu, M., Dera, P., Mao, H.-k., and Hemley, R. J. (2005). Novel chain structures in group vi elements. *Nat. Mater.*, 4(2):152–155.
- [32] Dellago, C., Bolhuis, P., and Geissler, P. L. (2002). Transition path sampling. *Adv. Chem. Phys.*, 123:1–78.

References

- [33] Dellago, C., Bolhuis, P. G., and Chandler, D. (1998a). Efficient transition path sampling: Application to Lennard-Jones cluster rearrangements. *J. Chem. Phys.*, 108(22):9236–9245.
- [34] Dellago, C., Bolhuis, P. G., and Chandler, D. (1999). On the calculation of reaction rate constants in the transition path ensemble. *J. Chem. Phys.*, 110(14):6617–6625.
- [35] Dellago, C., Bolhuis, P. G., Csajka, F. S., and Chandler, D. (1998b). Transition path sampling and the calculation of rate constants. *J. Chem. Phys.*, 108(5):1964–1977.
- [36] Desiraju, G. R. (2002). Cryptic crystallography. *Nat. Mater.*, 1(2):77–79.
- [37] Dion, M., Rydberg, H., Schröder, E., Langreth, D. C., and Lundqvist, B. I. (2004). Van der waals density functional for general geometries. *Phys. Rev. Lett.*, 92(24):246401.
- [38] Dove, M. T. (1997). Theory of displacive phase transitions in minerals. *Am. Mineral.*, 82(3):213–244.
- [39] Duan, D., Liu, Y., Tian, F., Li, D., Huang, X., Zhao, Z., Yu, H., Liu, B., Tian, W., and Cui, T. (2014). Pressure-induced metallization of dense $(\text{H}_2\text{S})_2\text{H}_2$ with high- T_c superconductivity. *Sci. Rep.*, 4.
- [40] Efimchenko, V., Kuzovnikov, M., Fedotov, V., Sakharov, M., Simonov, S., and Tkacz, M. (2011). New phase in the water–hydrogen system. *J. Alloy. Comp.*, 509, Supplement 2(0):S860 – S863.
- [41] Ensing, B., De Vivo, M., Liu, Z., Moore, P., and Klein, M. L. (2006). Metadynamics as a tool for exploring free energy landscapes of chemical reactions. *Acc. Chem. Res.*, 39(2):73–81.
- [42] Ensing, B., Laio, A., Parrinello, M., and Klein, M. L. (2005). A recipe for the computation of the free energy barrier and the lowest free energy path of concerted reactions. *J. Phys. Chem. B*, 109(14):6676–6687.
- [43] Eremets, M. I., Gavriluk, A. G., Trojan, I. A., Dzivenko, D. A., and Boehler, R. (2004). Single-bonded cubic form of nitrogen. *Nat. Mater.*, 3(8):558–563.
- [44] Evers, J., Göbel, M., Krumm, B., Martin, F., Medvedyev, S., Oehlinger, G., Steemann, F. X., Troyan, I., Klapötke, T. M., and Eremets, M. I. (2011). Molecular structure of hydrazoic acid with hydrogen-bonded tetramers in nearly planar layers. *J. Am. Chem. Soc.*, 133(31):12100–12105.
- [45] Eyring, H. (1935). The activated complex in chemical reactions. *J. Chem. Phys.*, 3(2):107–115.
- [46] Frenkel, D. and Smit, B. (2001). *Understanding molecular simulation: from algorithms to applications*, volume 1. Academic press.
- [47] G. Mills, H. J. and Jacobsen, K. W. (1998). *Classical and quantum dynamics in condensed phase simulations*, volume Chap. 16. World Scientific.
- [48] Gale, J. D. (1997). Gulp: A computer program for the symmetry-adapted simulation of solids. *J. Chem. Soc., Faraday Trans.*, 93(4):629–637.

- [49] Gao, G., Oganov, A. R., Ma, Y., Wang, H., Li, P., Li, Y., Itaka, T., and Zou, G. (2010). Dissociation of methane under high pressure. *J. Chem. Phys.*, 133:144508.
- [50] Gavezzotti, A. (1994). Are crystal structures predictable? *Acc. Chem. Res.*, 27(10):309–314.
- [51] Gervasio, F. L., Laio, A., and Parrinello, M. (2005). Flexible docking in solution using metadynamics. *J. Am. Chem. Soc.*, 127(8):2600–2607.
- [52] Giannozzi, P., Baroni, S., Bonini, N., Calandra, M., Car, R., Cavazzoni, C., Ceresoli, D., Chiarotti, G. L., Cococcioni, M., Dabo, I., et al. (2009). Quantum espresso: a modular and open-source software project for quantum simulations of materials. *J. Phys.: Condens. Matter*, 21(39):395502.
- [53] Greene, R. L., Street, G. B., and Suter, L. J. (1975). Superconductivity in polysulfur nitride (SN)_x. *Phys. Rev. Lett.*, 34:577–579.
- [54] Griffiths, G. I., Needs, R., and Pickard, C. J. (2012). High-pressure ionic and molecular phases of ammonia within density functional theory. *Phys. Rev. B*, 86(14):144102.
- [55] Grimme, S. (2006). Semiempirical gga-type density functional constructed with a long-range dispersion correction. *J. Comput. Chem.*, 27(15):1787–1799.
- [56] Grochala, W., Hoffmann, R., Feng, J., and Ashcroft, N. W. (2007). The chemical imagination at work in very tight places. *Angew. Chem. Int. Ed.*, 46(20):3620–3642.
- [57] Grocholski, B., Shim, S. H., and Prakapenka, V. B. (2010). Stability of the MgSiO₃ analog NaMgF₃ and its implication for mantle structure in super-earths. *Geophys. Res. Lett.*, 37(14):L14204.
- [58] Guillot, T. (1999). Interiors of giant planets inside and outside the solar system. *Science*, 286(5437):72–77.
- [59] Haines, J., Léger, J. M., Gorelli, F., Klug, D. D., Tse, J. S., and Li, Z. Q. (2001). X-ray diffraction and theoretical studies of the high-pressure structures and phase transitions in magnesium fluoride. *Phys. Rev. B*, 64:134110.
- [60] Hatch, D. M., Stokes, H. T., Dong, J., Gunter, J., Wang, H., and Lewis, J. P. (2005). Bilayer sliding mechanism for the zinc-blende to rocksalt transition in SiC. *Phys. Rev. B*, 71(18):184109.
- [61] Henkelman, G., Arnaldsson, A., and Jonsson, H. (2006). A fast and robust algorithm for bader decomposition of charge density. *Comput. Mater. Sci.*, 36(3):354 – 360.
- [62] Henkelman, G. and Jonsson, H. (2000). Improved tangent estimate in the nudged elastic band method for finding minimum energy paths and saddle points. *J. Chem. Phys.*, 113(22):9978–9985.
- [63] Henkelman, G., Uberuaga, B. P., and Jónsson, H. (2000). A climbing image nudged elastic band method for finding saddle points and minimum energy paths. *J. Chem. Phys.*, 113(22):9901–9904.

References

- [64] Heyd, J., Scuseria, G. E., and Ernzerhof, M. (2003). Hybrid functionals based on a screened coulomb potential. *J. Chem. Phys.*, 118(18):8207–8215.
- [65] Hirai, H., Kagawa, S., Tanaka, T., Matsuoka, T., Yagi, T., Ohishi, Y., Nakano, S., Yamamoto, Y., and Irifune, T. (2012). Structural changes of filled ice Ic hydrogen hydrate under low temperatures and high pressures from 5 to 50 GPa. *J. Chem. Phys.*, 137(7):074505.
- [66] Hirai, H., Ohno, S., Kawamura, T., Yamamoto, Y., and Yagi, T. (2007). Changes in vibration modes of hydrogen and water molecules and in lattice parameters with pressure for filled-ice hydrogen hydrates. *J. Phys. Chem. C*, 111(1):312–315.
- [67] Hohenberg, P. and Kohn, W. (1964). Inhomogeneous electron gas. *Phys. Rev.*, 136(3B):B864.
- [68] Hu, A. and Zhang, F. (2011). A hydronitrogen solid: high pressure ab initio evolutionary structure searches. *J. Phys.: Condens. Matter*, 23(2):022203.
- [69] Hu, C.-H., Oganov, A. R., Zhu, Q., Qian, G.-R., Frapper, G., Lyakhov, A. O., and Zhou, H.-Y. (2013). Pressure-induced stabilization and insulator-superconductor transition of bh. *Phys. Rev. Lett.*, 110:165504.
- [70] Hubbard, W. B. (1981). Interiors of the giant planets. *Science*, 214(4517):145–149.
- [71] Jaffe, J. E., Snyder, J. A., Lin, Z., and Hess, A. C. (2000). LDA and GGA calculations for high-pressure phase transitions in ZnO and MgO. *Phys. Rev. B*, 62(3):1660.
- [72] Jensen, F. (2013). *Introduction to computational chemistry*. John Wiley & Sons.
- [73] Johannesson, G. H., Bligaard, T., Ruban, A. V., Skriver, H. L., Jacobsen, K. W., and Nørskov, J. K. (2002). Combined electronic structure and evolutionary search approach to materials design. *Phys. Rev. Lett.*, 88(25):255506.
- [74] Jones, W. and Csizmadia, I. (1994). Polymeric $(\text{NO})_3(\text{N}_2\text{O})_n$, $(\text{NO})_3(\text{N}_2\text{O})_n^+$, and $(\text{NO})_3(\text{N}_2\text{O})_n^-$: an interpretation of experimental observations. *Z. Phys. D: At., Mol. Clusters*, 32(1):145–152.
- [75] Jones, W. H. (1991). Metastable polymers of the nitrogen oxides. 1. open chain nitric oxide analogs of polythiazyl: a mndo/am1 study. *J. Phys. Chem.*, 95(6):2588–2595.
- [76] Khaliullin, R. Z., Eshet, H., Kühne, T. D., Behler, J., and Parrinello, M. (2011). Nucleation mechanism for the direct graphite-to-diamond phase transition. *Nat. Mater.*, 10(9):693–697.
- [77] Kiryukhin, V., Bernard, E., Khmelenko, V. V., Boltnev, R., Krainyukova, N., and Lee, D. (2007). Noble-gas nanoclusters with fivefold symmetry stabilized in superfluid helium. *Phys. Rev. Lett.*, 98(19):195506.
- [78] Klimeš, J., Bowler, D. R., and Michaelides, A. (2011). Van der waals density functionals applied to solids. *Phys. Rev. B*, 83:195131.
- [79] Kohn, W. and Sham, L. J. (1965). Self-consistent equations including exchange and correlation effects. *Phys. Rev.*, 140(4A):A1133.

- [80] Krainyukova, N. (2007). The energetics of large lennard-jones clusters: transition to the hexagonal close-packed structure. *The European Physical Journal D-Atomic, Molecular, Optical and Plasma Physics*, 43(1):45–48.
- [81] Krainyukova, N. V. (2006). ‘The crystal structure problem’ in noble gas nanoclusters. *Thin Solid Films*, 515(4):1658–1663.
- [82] Krainyukova, N. V., Boltnev, R. E., Bernard, E., Khmelenko, V. V., Lee, D. M., and Kiryukhin, V. (2012). Observation of the fcc-to-hcp transition in ensembles of argon nanoclusters. *Phys. Rev. Lett.*, 109(24):245505.
- [83] Kresse, G. and Furthmüller, J. (1996). Efficient iterative schemes for *ab initio* total-energy calculations using a plane-wave basis set. *Phys. Rev. B*, 54:11169–11186.
- [84] Kudin, K. N. and Car, R. (2005). Free energy profile along a discretized reaction path via the hyperplane constraint force and torque. *J. Chem. Phys.*, 122(11):114108.
- [85] Laio, A. and Parrinello, M. (2002). Escaping free-energy minima. *Proc. Natl. Acad. Sci. USA*, 99(20):12562–12566.
- [86] Landau, L. D. and Lifshitz, E. M. (2013). *Course of theoretical physics*. Elsevier.
- [87] Lazzeri, M. and Mauri, F. (2003). First-principles calculation of vibrational raman spectra in large systems: Signature of small rings in crystalline SiO₂. *Phys. Rev. Lett.*, 90:036401.
- [88] Lenz, A. and Ojamäe, L. (2011). Structures of the I-, II- and H-methane clathrates and the Ice-methane clathrate phase transition from quantum-chemical modeling with force-field thermal corrections. *J. Phys. Chem. A*, 115(23):6169–6176.
- [89] Li, K., Wang, X., Zhang, F., and Xue, D. (2008). Electronegativity identification of novel superhard materials. *Phys. Rev. Lett.*, 100(23):235504.
- [90] Liebman, J. F. (1997). Existence and estimated enthalpies of formation of ammonium hydroxide, hydronium amide, and some related species. *Struct. Chem.*, 8(4):313–315.
- [91] Limpijumngong, S. and Jungthawan, S. (2004). First-principles study of the wurtzite-to-rocksalt homogeneous transformation in ZnO: A case of a low-transformation barrier. *Phys. Rev. B*, 70(5):054104.
- [92] Limpijumngong, S. and Lambrecht, W. R. (2001). Homogeneous strain deformation path for the wurtzite to rocksalt high-pressure phase transition in GaN. *Phys. Rev. Lett.*, 86(1):91.
- [93] Liu, Q.-J., Zeng, W., Liu, F.-S., and Liu, Z.-T. (2013). First-principles study of hydronitrogen compounds: Molecular crystalline NH₄N₃ and N₂H₅N₃. *Comput. Theor. Chem.*, 1014:37–42.
- [94] Liu, Q.-J., Zhang, N.-C., Sun, Y.-Y., Zhang, M.-J., Liu, F.-S., and Liu, Z.-T. (2014a). Density-functional theory study of the pressure-induced phase transition in hydronitrogen compound N₄H₄. *Phys. Rev. A*, 378(18):1333–1335.

References

- [95] Liu, Q.-J., Zhang, N.-C., Wu, J., Sun, Y.-Y., Zhang, M.-J., Liu, F.-S., Wang, H.-Y., and Liu, Z.-T. (2014b). Theoretical insight into the structural, elastic and electronic properties of N_4H_4 compounds. *Comput. Mater. Sci.*, 81:582–586.
- [96] Lokshin, K. A., Zhao, Y., He, D., Mao, W. L., Mao, H.-K., Hemley, R. J., Lobanov, M. V., and Greenblatt, M. (2004). Structure and dynamics of hydrogen molecules in the novel clathrate hydrate by high pressure neutron diffraction. *Phys. Rev. Lett.*, 93:125503.
- [97] Loveday, J. S. and Nelmes, R. J. (2008). High-pressure gas hydrates. *Phys. Chem. Chem. Phys.*, 10:937–950.
- [98] Lyakhov, A. O., Oganov, A. R., Stokes, H. T., and Zhu, Q. (2013). New developments in evolutionary structure prediction algorithm uspeX. *Comput. Phys. Commun.*, 184(4):1172–1182.
- [99] Lyakhov, A. O., Oganov, A. R., and Valle, M. (2010). How to predict very large and complex crystal structures. *Comput. Phys. Commun.*, 181(9):1623–1632.
- [100] Ma, Y., Oganov, A. R., Li, Z., Xie, Y., and Kotakoski, J. (2009). Novel high pressure structures of polymeric nitrogen. *Phys. Rev. Lett.*, 102:065501.
- [101] Machida, S.-I., Hirai, H., Kawamura, T., Yamamoto, Y., and Yagi, T. (2008). Structural changes of filled ice Ic structure for hydrogen hydrate under high pressure. *J. Chem. Phys.*, 129(22):224505.
- [102] Machida, S.-I., Hirai, H., Kawamura, T., Yamamoto, Y., and Yagi, T. (2010). Structural changes and intermolecular interactions of filled ice Ic structure for hydrogen hydrate under high pressure. *J. Phys.: Conf. Ser.*, 215(1):012060.
- [103] Machida, S.-I., Hirai, H., Kawamura, T., Yamamoto, Y., and Yagi, T. (2011). Isotopic effect and amorphization of deuterated hydrogen hydrate under high pressure. *Phys. Rev. B*, 83:144101.
- [104] Maddox, J. (1988). Crystals from first principles. *Nature*, 335(6187).
- [105] Mao, W. L. and Mao, H.-K. (2004). Hydrogen storage in molecular compounds. *Proc. Natl. Acad. Sci. USA*, 101(3):708–710.
- [106] Mao, W. L., Mao, H.-K., Goncharov, A. F., Struzhkin, V. V., Guo, Q., Hu, J., Shu, J., Hemley, R. J., Somayazulu, M., and Zhao, Y. (2002). Hydrogen clusters in clathrate hydrate. *Science*, 297(5590):2247–2249.
- [107] Maragakis, P., Andreev, S. A., Brumer, Y., Reichman, D. R., and Kaxiras, E. (2002). Adaptive nudged elastic band approach for transition state calculation. *J. Chem. Phys.*, 117(10):4651–4658.
- [108] Martin, R. M. (2004). *Electronic structure: basic theory and practical methods*. Cambridge university press.
- [109] Martoňák, R., Laio, A., Bernasconi, M., Ceriani, C., Raiteri, P., Zipoli, F., and Parrinello, M. (2005). Simulation of structural phase transitions by metadynamics. *Z. Kristallogr.*, 220(5/6/2005):489–498.

- [110] Martoňák, R., Laio, A., and Parrinello, M. (2003). Predicting crystal structures: the parrinello-rahman method revisited. *Phys. Rev. Lett.*, 90(7):075503.
- [111] Masel, R. I. (1996). *Principles of adsorption and reaction on solid surfaces*, volume 3. John Wiley & Sons.
- [112] Metropolis, N., Rosenbluth, A. W., Rosenbluth, M. N., Teller, A. H., and Teller, E. (1953). Equation of state calculations by fast computing machines. *J. Chem. Phys.*, 21(6):1087–1092.
- [113] Miao, M. and Lambrecht, W. R. (2003). Unified path for high-pressure transitions of SiC polytypes to the rocksalt structure. *Phys. Rev. B*, 68(9):092103.
- [114] Miao, M. and Lambrecht, W. R. (2005). Universal transition state for high-pressure zinc blende to rocksalt phase transitions. *Phys. Rev. Lett.*, 94(22):225501.
- [115] Miao, M., Prikhodko, M., and Lambrecht, W. R. (2002a). Changes of the geometry and band structure of SiC along the orthorhombic high-pressure transition path between the zinc-blende and rocksalt structures. *Phys. Rev. B*, 66(6):064107.
- [116] Miao, M., Prikhodko, M., and Lambrecht, W. R. (2002b). Comment on “orthorhombic intermediate state in the zinc blende to rocksalt transformation path of SiC at high pressure”. *Phys. Rev. Lett.*, 88(18):189601.
- [117] Mikulski, C., Russo, P., Saran, M., MacDiarmid, A., Garito, A., and Heeger, A. (1975). Synthesis and structure of metallic polymeric sulfur nitride, SN_x , and its precursor, disulfur dinitride, S_2N_2 . *J. Am. Chem. Soc.*, 97(22):6358–6363.
- [118] Mills, G., Jónsson, H., and Schenter, G. K. (1995). Reversible work transition state theory: application to dissociative adsorption of hydrogen. *Surf. Sci.*, 324(2):305–337.
- [119] Mujica, A., Rubio, A., Muñoz, A., and Needs, R. (2003). High-pressure phases of group-IV, III–V, and II–VI compounds. *Rev. Mod. Phys.*, 75(3):863.
- [120] Murakami, M., Hirose, K., Kawamura, K., Sata, N., and Ohishi, Y. (2004). Post-perovskite phase transition in $MgSiO_3$. *Science*, 304(5672):855–858.
- [121] Nakamura, S. (1998). The roles of structural imperfections in ingan-based blue light-emitting diodes and laser diodes. *Science*, 281(5379):956–961.
- [122] Nielsen, O. and Martin, R. M. (1985). Stresses in semiconductors: Ab initio calculations on Si, Ge, and GaAs. *Phys. Rev. B*, 32(6):3792.
- [123] Ninet, S., Datchi, F., Dumas, P., Mezouar, M., Garbarino, G., Mafety, A., Pickard, C., Needs, R., and Saitta, A. (2014). Experimental and theoretical evidence for an ionic crystal of ammonia at high pressure. *Phys. Rev. B*, 89(17):174103.
- [124] Oganov, A. R. (2011). *Modern methods of crystal structure prediction*. John Wiley & Sons.
- [125] Oganov, A. R. and Glass, C. W. (2006). Crystal structure prediction using ab initio evolutionary techniques: Principles and applications. *J. Chem. Phys.*, 124(24):–.

References

- [126] Oganov, A. R., Lyakhov, A. O., and Valle, M. (2011). How evolutionary crystal structure prediction works—and why. *Acc. Chem. Res.*, 44(3):227–237.
- [127] Oganov, A. R., Ma, Y., Lyakhov, A. O., Valle, M., and Gatti, C. (2010). Evolutionary crystal structure prediction as a method for the discovery of minerals and materials. *Rev. Mineral. Geochem.*, 71(1):271–298.
- [128] Oganov, A. R. and Ono, S. (2004). Theoretical and experimental evidence for a post-perovskite phase of MgSiO_3 in earth's d'' layer. *Nature*, 430(6998):445–448.
- [129] Oganov, A. R. and Valle, M. (2009). How to quantify energy landscapes of solids. *J. Chem. Phys.*, 130(10):104504.
- [130] Öhrström, L. and Larsson, K. (2005). *Molecule-Based Materials: The Structural Network Approach*. Elsevier.
- [131] Palasyuk, T., Troyan, I., Eremets, M., Drozd, V., Medvedev, S., Zaleski-Ejgierd, P., Magos-Palasyuk, E., Wang, H., Bonev, S. A., Dudenko, D., et al. (2014). Ammonia as a case study for the spontaneous ionization of a simple hydrogen-bonded compound. *Nat. Commun.*, 5.
- [132] Parrinello, M. and Rahman, A. (1980). Crystal structure and pair potentials: A molecular-dynamics study. *Phys. Rev. Lett.*, 45(14):1196.
- [133] Perdew, J. P., Burke, K., and Ernzerhof, M. (1996). Generalized gradient approximation made simple. *Phys. Rev. Lett.*, 77(18):3865.
- [134] Perdew, J. P., Chevary, J., Vosko, S., Jackson, K. A., Pederson, M. R., Singh, D., and Fiolhais, C. (1992). Atoms, molecules, solids, and surfaces: Applications of the generalized gradient approximation for exchange and correlation. *Phys. Rev. B*, 46(11):6671.
- [135] Perdew, J. P., Ruzsinszky, A., Csonka, G. I., Vydrov, O. A., Scuseria, G. E., Constantin, L. A., Zhou, X., and Burke, K. (2008). Restoring the density-gradient expansion for exchange in solids and surfaces. *Phys. Rev. Lett.*, 100(13):136406.
- [136] Perez-Mato, J., Aroyo, M., Capillas, C., Blaha, P., and Schwarz, K. (2003). Comment on“orthorhombic intermediate state in the zinc blende to rocksalt transformation path of sic at high pressure”. *Phys. Rev. Lett.*, 90(4):49603.
- [137] Pfrommer, B. G., Côté, M., Louie, S. G., and Cohen, M. L. (1997). Relaxation of crystals with the quasi-newton method. *J. Comput. Chem.*, 131(1):233–240.
- [138] Piana, S. and Laio, A. (2007). A bias-exchange approach to protein folding. *J. Phys. Chem. B*, 111(17):4553–4559.
- [139] Pickard, C. J. and Needs, R. (2008). Highly compressed ammonia forms an ionic crystal. *Nat. Mater.*, 7(10):775–779.
- [140] Pickard, C. J. and Needs, R. (2011). Ab initio random structure searching. *J. Phys.: Condens. Matter*, 23(5):053201.
- [141] Pickard, C. J. and Needs, R. J. (2007). Structure of phase III of solid hydrogen. *Nat. Phys.*, 3(11):473–476.

- [142] Pratt, L. R. (1986). A statistical method for identifying transition states in high dimensional problems. *J. Chem. Phys.*, 85(9):5045–5048.
- [143] Qian, G.-R., Dong, X., Zhou, X.-F., Tian, Y., Oganov, A. R., and Wang, H.-T. (2013). Variable cell nudged elastic band method for studying solid–solid structural phase transitions. *Comput. Phys. Commun.*, 184(9):2111–2118.
- [144] Qian, G.-R., Hu, C.-H., Oganov, A. R., Zeng, Q., and Zhou, H.-Y. (2014a). Diverse chemistry of stable hydronitrogens, and implications for planetary and materials sciences. *arXiv preprint arXiv:1411.4513*.
- [145] Qian, G.-R., Lyakhov, A. O., Zhu, Q., Oganov, A. R., and Dong, X. (2014b). Novel hydrogen hydrate structures under pressure. *Sci. Rep.*, 4.
- [146] Quapp, W. and Heidrich, D. (1984). Analysis of the concept of minimum energy path on the potential energy surface of chemically reacting systems. *Theor. Chim. Acta*, 66(3-4):245–260.
- [147] Raoult, B., Farges, J., De Feraudy, M., and Torchet, G. (1989). Comparison between icosahedral, decahedral and crystalline lennard-jones models containing 500 to 6000 atoms. *Philos. Mag. B*, 60(6):881–906.
- [148] Ross, M. (1981). The ice layer in uranus and neptune—diamonds in the sky? *Nature*, 292:435–436.
- [149] Rowley, L., Nicholson, D., and Parsonage, N. (1975). Monte carlo grand canonical ensemble calculation in a gas-liquid transition region for 12-6 argon. *J. Comput. Phys.*, 17(4):401–414.
- [150] Saitta, A. M. and Decremps, F. (2004). Unifying description of the wurtzite-to-rocksalt phase transition in wide-gap semiconductors: The effect of d electrons on the elastic constants. *Phys. Rev. B*, 70(3):035214.
- [151] Santra, B., Klimeš, J., Alfè, D., Tkatchenko, A., Slater, B., Michaelides, A., Car, R., and Scheffler, M. (2011). Hydrogen bonds and van der waals forces in ice at ambient and high pressures. *Phys. Rev. Lett.*, 107:185701.
- [152] Sasselov, D. D. (2008). Astronomy: Extrasolar planets. *Nature*, 451(7174):29–31.
- [153] Schön, J., Putz, H., and Jansen, M. (1996). Studying the energy hypersurface of continuous systems—the threshold algorithm. *J. Phys.: Condens. Matter*, 8(2):143.
- [154] Serrano, J., Rubio, A., Hernández, E., Muñoz, A., and Mujica, A. (2000). Theoretical study of the relative stability of structural phases in group-III nitrides at high pressures. *Phys. Rev. B*, 62(24):16612.
- [155] Shan, W., Little, B., Fischer, A., Song, J., Goldenberg, B., Perry, W., Bremser, M., and Davis, R. (1996). Binding energy for the intrinsic excitons in wurtzite gan. *Phys. Rev. B*, 54(23):16369.
- [156] Sheppard, D., Terrell, R., and Henkelman, G. (2008). Optimization methods for finding minimum energy paths. *J. Chem. Phys.*, 128(13):134106.

References

- [157] Sheppard, D., Xiao, P., Chemelewski, W., Johnson, D. D., and Henkelman, G. (2012). A generalized solid-state nudged elastic band method. *J. Chem. Phys.*, 136(7):074103.
- [158] Shimojo, F., Ebbsjö, I., Kalia, R. K., Nakano, A., Rino, J. P., and Vashishta, P. (2000). Molecular dynamics simulation of structural transformation in silicon carbide under pressure. *Phys. Rev. Lett.*, 84(15):3338.
- [159] Shimojo, F., Kodiyalam, S., Ebbsjö, I., Kalia, R. K., Nakano, A., and Vashishta, P. (2004). Atomistic mechanisms for wurtzite-to-rocksalt structural transformation in cadmium selenide under pressure. *Phys. Rev. B*, 70(18):184111.
- [160] Sibani, P., Schön, J. C., Salamon, P., and Andersson, J.-O. (1993). Emergent hierarchical structures in complex-system dynamics. *Europhys. Lett.*, 22(7):479.
- [161] Silva, C., Leite Alves, H., Scolfaro, L., and Leite, J. (2005). Pressure-induced phase transitions and polytypic structures in III-nitrides. *Phys. Status Solidi C*, 2(7):2468–2471.
- [162] Somayazulu, M., Finger, L., Hemley, R., and Mao, H. (1996). High-pressure compounds in methane-hydrogen mixtures. *Science*, 271(5254):1400–1402.
- [163] Song, J., Corrales, L. R., Kresse, G., and Jónsson, H. (2001). Migration of o vacancies in α -quartz: The effect of excitons and electron holes. *Phys. Rev. B*, 64(13):134102.
- [164] Sowa, H. (2001). On the transition from the wurtzite to the nacl type. *Acta Crystallogr., Sect. A: Found. Crystallogr.*, 57(2):176–182.
- [165] Sowa, H. (2005). A transition path for the pressure-induced wurtzite-to NaCl-type transformation described in Pna2₁. *Acta Crystallogr., Sect. A: Found. Crystallogr.*, 61(3):325–330.
- [166] Strobel, T. A., Somayazulu, M., and Hemley, R. J. (2011). Phase behavior of H₂ + H₂O at high pressures and low temperatures. *J. Phys. Chem. C*, 115(11):4898–4903.
- [167] Sun, J., Martinez-Canales, M., Klug, D. D., Pickard, C. J., and Needs, R. J. (2012). Persistence and eventual demise of oxygen molecules at terapascal pressures. *Phys. Rev. Lett.*, 108:045503.
- [168] Sun, J., Martinez-Canales, M., Klug, D. D., Pickard, C. J., and Needs, R. J. (2013). Stable all-nitrogen metallic salt at terapascal pressures. *Phys. Rev. Lett.*, 111:175502.
- [169] Togo, A., Oba, F., and Tanaka, I. (2008). First-principles calculations of the ferroelastic transition between rutile-type and CaCl₂-type SiO₂ at high pressures. *Phys. Rev. B*, 78:134106.
- [170] Tolédano, J.-C. and Tolédano, P. (1987). *The Landau theory of phase transitions*. World Scientific.
- [171] Tolédano, P. and Dmitriev, V. (1996). *Reconstructive phase transitions*. World Scientific.
- [172] Troullier, N. and Martins, J. L. (1991). Efficient pseudopotentials for plane-wave calculations. *Phys. Rev. B*, 43(3):1993.

- [173] Trygubenko, S. A. and Wales, D. J. (2004). A doubly nudged elastic band method for finding transition states. *J. Chem. Phys.*, 120(5):2082–2094.
- [174] Tsuchiya, T., Tsuchiya, J., Umemoto, K., and Wentzcovitch, R. M. (2004). Phase transition in MgSiO_3 perovskite in the earth's lower mantle. *Earth. Planet. Sci. Lett.*, 224(3):241–248.
- [175] Umemoto, K., Wentzcovitch, R. M., and Allen, P. B. (2006a). Dissociation of MgSiO_3 in the cores of gas giants and terrestrial exoplanets. *Science*, 311(5763):983.
- [176] Umemoto, K., Wentzcovitch, R. M., Weidner, D. J., and Parise, J. B. (2006b). $\text{Mg}_3\text{Si}_2\text{O}_7$: A low-pressure analog of MgSiO_3 . *Geophys. Res. Lett.*, 33(15):L15304.
- [177] Van Beest, B., Kramer, G., and Van Santen, R. (1990). Force fields for silicas and aluminophosphates based on ab initio calculations. *Phys. Rev. Lett.*, 64(16):1955.
- [178] Vanderbilt, D. (1990). Soft self-consistent pseudopotentials in a generalized eigenvalue formalism. *Phys. Rev. B*, 41(11):7892.
- [179] Vargiu, A. V., Ruggerone, P., Magistrato, A., and Carloni, P. (2008). Dissociation of minor groove binders from dna: insights from metadynamics simulations. *Nucleic Acids Res.*, 36(18):5910–5921.
- [180] Vineyard, G. H. (1957). Frequency factors and isotope effects in solid state rate processes. *J. Phys. Chem. Solids*, 3(1):121–127.
- [181] Vos, W. L., Finger, L. W., Hemley, R. J., and Kwang Mao, H. (1996). Pressure dependence of hydrogen bonding in a novel $\text{H}_2\text{O} - \text{H}_2$ clathrate. *Chem. Phys. Lett.*, 257(5–6):524 – 530.
- [182] Vos, W. L., Finger, L. W., Hemley, R. J., and Mao, H.-K. (1993). Novel $\text{H}_2 - \text{H}_2\text{O}$ clathrates at high pressures. *Phys. Rev. Lett.*, 71:3150–3153.
- [183] Voter, A. F. (1997). A method for accelerating the molecular dynamics simulation of infrequent events. *J. Chem. Phys.*, 106(11):4665–4677.
- [184] Wales, D. J. (2003). *Energy Landscapes*. Cambridge University Press.
- [185] Wales, D. J. and Bogdan, T. V. (2006). Potential energy and free energy landscapes. *J. Phys. Chem. B*, 110(42):20765–20776.
- [186] Wales, D. J. and Doye, J. P. (1997). Global optimization by basin-hopping and the lowest energy structures of Lennard-Jones clusters containing up to 110 atoms. *J. Phys. Chem. A*, 101(28):5111–5116.
- [187] Wales, D. J. and Scheraga, H. A. (1999). Global optimization of clusters, crystals, and biomolecules. *Science*, 285(5432):1368–1372.
- [188] Wang, X., Wang, Y., Miao, M., Zhong, X., Lv, J., Cui, T., Li, J., Chen, L., Pickard, C. J., and Ma, Y. (2012). Cagelike diamondoid nitrogen at high pressures. *Phys. Rev. Lett.*, 109:175502.

References

- [189] Wang, Y., Liu, H., Lv, J., Zhu, L., Wang, H., and Ma, Y. (2011). High pressure partially ionic phase of water ice. *Nat Commun.*, 2:563.
- [190] Wentzcovitch, R. M. (1991). Invariant molecular-dynamics approach to structural phase transitions. *Phys. Rev. B*, 44(5):2358.
- [191] Wert, C. and Zener, C. (1949). Interstitial atomic diffusion coefficients. *Phys. Rev.*, 76(8):1169.
- [192] White, J. and Bird, D. (1994). Implementation of gradient-corrected exchange-correlation potentials in car-parrinello total-energy calculations. *Phys. Rev. B*, 50(7):4954.
- [193] Wigner, E. (1938). The transition state method. *Trans. Faraday Soc.*, 34:29–41.
- [194] Wilson, M. and Madden, P. A. (2002). Transformations between tetrahedrally and octahedrally coordinated crystals: the wurtzite \rightarrow rocksalt and blende \rightarrow rocksalt mechanisms. *J. Phys.: Condens. Matter*, 14(18):4629.
- [195] Yin, K., Wang, Y., Liu, H., Peng, F., and Zhang, L. (2015). N_2H : a novel polymeric hydronitrogen as a high energy density material. *J. Matter. Chem. A*, 3(8):4188–4194.
- [196] Zhang, H.-D., Zheng, S.-K., Jin, X.-L., Jiang, S.-Q., He, Z., Liu, B.-B., and Cui, T. (2014). Crystal structure prediction and hydrogen-bond symmetrization of solid hydrazine under high pressure: a first-principles study. *Acta Cryst. C*, 70(2):112–117.
- [197] Zhang, J., Kuo, J.-L., and Iitaka, T. (2012). First principles molecular dynamics study of filled ice hydrogen hydrate. *J. Chem. Phys.*, 137(8):084505.
- [198] Zhang, R., Sheng, S., and Veprek, S. (2007). Mechanism of the b 3 to b 1 transformation in cubic aln under uniaxial stress. *Phys. Rev. B*, 76(7):075208.
- [199] Zhang, W., Oganov, A. R., Goncharov, A. F., Zhu, Q., Boulfelfel, S. E., Lyakhov, A. O., Stavrou, E., Somayazulu, M., Prakapenka, V. B., and Konôpková, Z. (2013). Unexpected stable stoichiometries of sodium chlorides. *Science*, 342(6165):1502–1505.
- [200] Zhu, Q. (2013). Crystal structure prediction and its application in earth and materials sciences. (*Doctoral dissertation, Stony Brook University*).
- [201] Zhu, Q., Jung, D. Y., Oganov, A. R., Glass, C. W., Gatti, C., and Lyakhov, A. O. (2012a). Stability of xenon oxides at high pressures. *Nat. Chem.*, 5(1):61–65.
- [202] Zhu, Q., Li, L., Oganov, A. R., and Allen, P. B. (2013a). Evolutionary method for predicting surface reconstructions with variable stoichiometry. *Phys. Rev. B*, 87(19):195317.
- [203] Zhu, Q., Oganov, A. R., Glass, C. W., and Stokes, H. T. (2012b). Constrained evolutionary algorithm for structure prediction of molecular crystals: methodology and applications. *Acta Crystallogr., Sect. B: Struct. Sci*, 68(3):215–226.
- [204] Zhu, Q., Oganov, A. R., and Lyakhov, A. O. (2012c). Evolutionary metadynamics: a novel method to predict crystal structures. *CrystEngComm*, 14(10):3596–3601.
- [205] Zhu, Q., Oganov, A. R., and Lyakhov, A. O. (2013b). Novel stable compounds in the Mg-O system under high pressure. *Phys. Chem. Chem. Phys.*, 15:7696–7700.